SYSTEMATIC STUDY OF EARTHQUAKE TRIGGERING USING MICROEARTHQUAKES DETECTED BY THE MATCHED FILTER TECHNIQUE

A Dissertation
Presented to
The Academic Faculty

by

Xiaofeng Meng

In Partial Fulfillment
of the Requirements for the Degree
DOCTOR OF PHILOSOPHY in the
School of Earth and Atmospheric Sciences

Georgia Institute of Technology
August 2015

SYSTEMATIC STUDY OF EARTHQUAKE TRIGGERING USING MICROEARTHQUAKES DETECTED BY THE MATCHED FILTER TECHNIQUE

Approved by:

Dr. Zhigang Peng, Advisor
School of Earth and Atmospheric Sciences
Georgia Institute of Technology

Dr. Christian Huber
School of Earth and Atmospheric Sciences
Georgia Institute of Technology

Dr. Andrew Newman
School of Earth and Atmospheric Sciences
Georgia Institute of Technology

Dr. Yao Xie
H. Milton Stewart School of Industrial and Systems Engineering
Georgia Institute of Technology

Dr. Josef Dufek
School of Earth and Atmospheric Sciences
Georgia Institute of Technology

Date Approved: May 11, 2015

To My Family

ACKNOWLEDGEMENTS

I would like to first thank my advisor Dr. Zhigang Peng for his patience, support, and guidance of my doctoral work. His expertise, innovative vision, and advices inspired me during all the years that I worked with him. I would also thank my committee members Dr. Andrew Newman, Dr. Josef Dufek, Dr. Christian Huber, and Dr. Yao Xie for their valuable discussion and critical comments.

This work also benefits from the discussion and helps from many researchers. I would like to give my thanks to Dr. Jeanne Hardebeck, Dr. David Shelly, Dr. Ross Stein, Dr. Chunquan Wu, Dr. Bo Hong, Xiao Yu, Dr. Kim Olsen, Dr. Debi Kilb, Dr. Peng Zhao, Dr. Jake Walter, and Dr. Hongfeng Yang. I also want to thank many of my colleagues and friends in Georgia Institute of Technology, including Dr. Lujia Feng, Dr. Jaime Convers, Dr. Carol Paty, Dr. Kurt Frankel, Yan Luo, Chuanfei Dong, Chenxiao Du, Dr. Chastity Aiken, Dr. Kevin Chao, Dr. Joe Estep, Dr. Zach Lifton, Zefeng Li, Dongdong Yao, Brendan Sullivan, Wenlong Yu, Wenchao Jiang, Shangguo Zhu, Feng Wang and all the other current and past members in the Geophysics group.

Finally, I want to thank my parents and my dear wife Qian Wang for their support and faith in me.

TABLE OF CONTENTS

LIST OF TABLES

LIST OF FIGURES

SUMMARY

Earthquakes can be promoted or inhibited by surprisingly small stress perturbations. Most importantly, earthquake triggers other seismic or aseismic events in a wide range of time (seconds to years) and space (meters to thousands of kilometers) windows. The most commonly proposed stress transfer mechanisms include permanent stress redistribution caused by fault slip (i.e., static stress), radiated seismic waves (i.e., dynamic stress) and post-seismic stress redistribution. Moreover, earthquakes can be triggered by other natural and anthropogenic processes, such as magma intrusion, atmospheric pressure changes, solid earth tide and wastewater disposal. Studies of earthquake triggering have the potential for helping us understand the physics of the earthquake nucleation, and ultimately, improve seismic hazard assessment and mitigation by forecasting where the next "domino" may fall. My dissertation primarily focuses on the physical mechanisms of earthquake triggering in different tectonic regions, including major plate boundary (central and southern California) and intraplate regions (central and eastern United States).

I first introduce a GPU-based matched filter technique, which detects microearthquakes that are missing from standard earthquake catalogs. The matched filter technique utilizes waveforms of previously identified earthquakes as templates and scan through the continuous to search for similar signals. It is extremely useful to detect low signal-to-noise signals, such as early aftershocks, foreshocks, earthquake swarms and low frequency earthquakes within tremor episodes. However, one major disadvantage of this technique is that it can be very computationally intensive and not feasible for very large

dataset. The GPU-based code takes advantage of multiple levels of parallelism in the algorithm and is able to achieve ~40 times speedup over a single CPU.

In Chapter 3, I investigate the seismicity rate changes along the Parkfield section of the San Andreas Fault following the 2003 M_w 6.5 San Simeon earthquake. A M_w 6.0 earthquake occurred ~60 km from and 9 months after the 2003 San Simeon earthquake near Parkfield, which indicates a possible triggering case. Here I apply the waveform-based matched filter technique to systematically detect earthquakes near Parkfield around the origin time of the San Simeon earthquake. I identify ~8 times more earthquakes than in the Northern California Seismic Network (NCSN) catalog. The newly identified events along the creeping section of the San Andreas Fault show a statistically significant decrease following the San Simeon mainshock, which correlates well with the negative static shear stress changes (i.e., stress shadow) cast by the mainshock. In comparison, the seismicity rate around the hypocenter of the Parkfield earthquake increased moderately where the static shear stress changes are positive. The seismicity rate changes correlate well with the static shear stress changes induced by the San Simeon mainshock, suggesting a low friction in the seismogenic zone along the Parkfield section of the San Andreas Fault.

In the next Chapter, I examine the seismicity rate changes in southern California following the 2010 M_w 7.2 El Mayor-Cucapah earthquake. I focus on the Salton Sea Geothermal Field and the San Jacinto Fault Zone because of high-sensitivity continuous borehole recordings and ample background seismicity. A significant increase in seismic activity is found in both study regions immediately following the mainshock. However, near the Salton Sea where the static Coulomb stress decreased, the seismicity rate

dropped below the pre-mainshock level after ~1 month. In comparison, along the San Jacinto Fault with an increase in the static Coulomb stress, the seismicity rate remained higher than the background rate with several moderate-size earthquakes occurring in the subsequent months. While cannot completely rule out other mechanisms, these observations are best explained by dynamic stress changes immediately after the mainshock and static stress changes in longer term. My observation, together with other recent studies, suggests that both static and dynamic stress changes are important in triggering near-field earthquakes, but their affected regions and timescales are different.

In Chapter 5, I compare the sizes of aftershock zone of 10 M>4 earthquakes near the Anza gap of the San Jacinto Fault. Recent geodetic studies revealed a much shallower locking depth of 10-12 km than the seismogenic depth of 15-17 km outlined by microearthquakes in this region. This disagreement leads to the speculation that creep episodes exist in the lower part of seismogenic zone. Whether deep creep occurs along the fault holds key indication on how tectonic stress is released in this region and seismic hazard imposed to southern California. I first obtain more complete earthquake catalogs for the 10 earthquake sequences using the matched filter technique. Then, I find anomalously large aftershock zones for mainshocks occurred below the geodetically inferred locking depth (i.e., ~12 km), which strongly suggests a weak root of the San Jacinto Fault. However, I do not observe clear migration of aftershocks that might be driven by the deep creep. The presence of a weak root of the San Jacinto Fault likely provides a constraint on the maximum magnitude of future events within the Anza gap.

In Chapter 6 of my dissertation, I focus on whether major meteorological forces are capable of affecting seismic activities. On August 23, 2011, a magnitude 5.7 reverse

faulting earthquake struck Louisa County in Virginia and was followed by numerous aftershocks. About three days later, a category II hurricane, Irene, passed by the epicentral region, providing a unique opportunity to evaluate whether a hurricane could affect seismicity. Using identified aftershocks in this region as templates, I detect several times more events than existing earthquake catalogs. A clear increase of off-fault aftershocks was found during Irene's pass-by. After ruling out other possible triggering mechanisms, I conclude that atmospheric pressure decrease associated with the hurricane eye center may unclamp the reverse fault with a stress perturbation on the order of 1-2 kPa and have triggered additional aftershocks.

CHAPTER 1

INTRODUCTION

1.1 Overview of Earthquake Triggering

Earthquakes occur when the elastic stress overcomes failure stress along a fault. The elastic stress is accumulated due to the long-term relative motion across the fault driven by plate tectonics. The stress condition along the fault can be described by a Coulomb failure criterion [*Scholz*, 1990]:

$$CFS = \tau - \mu(\sigma_N - P) \tag{1.1}$$

where CFS is the Coulomb failure stress, τ is the shear stress, σ_N is the normal stress, P is the pore pressure and μ is the coefficient of friction. In much shorter time scales, the shear and normal stresses, pore pressure and coefficient of friction can be altered by natural and anthropogenic processes. Triggering is the result of such stress perturbation induced by those processes. One can calculate the change in Coulomb stress following:

$$\Delta CFS = \Delta\tau - \mu(\Delta\sigma_N - \Delta P) \tag{1.2}$$

The most frequently studied triggering mechanisms are static and dynamic triggering following large earthquakes [*Stein*, 1999; *Hill and Prejean*, 2007]. Static triggering refers to earthquakes being triggered by stress changes caused by fault displacement, which are permanent (thus 'static') but decay fast with distance r (i.e., r^{-3}). Dynamic triggering refers to earthquakes being triggered by stress changes caused by passing seismic waves, which are transient (thus 'dynamic') but decay slower with distance (i.e., $r^{-1.5}$). The minimum stress changes able to trigger earthquakes are on the

order of a few kPa [*Hill and Prejean*, 2007]. In remote distances (several rupture lengths away), only dynamic stress changes are large enough to trigger earthquakes. However, in near field, scientists are still debating on whether static or dynamic stresses are more important in triggering [e.g., *Felzer and Brodsky*, 2005; *Richards-Dinger et al.*, 2010]. Moreover, it is well established that postseismic relaxation mechanisms, including afterslip [*Peng and Zhao*, 2009], viscous relaxation [e.g., *Freed and Lin*, 2001] and poroelastic rebound [e.g., *Peltzer et al.*, 1998], can trigger earthquakes and successfully explained the long delay between mainshocks and triggered earthquakes in many cases. Finally, other natural processes, such as magma intrusion [e.g., *Toda et al.*, 2002] and solid earth tide [e.g., *Cochran et al.*, 2004], and anthropogenic process, such as wastewater disposal [e.g., *Ellsworth*, 2013], trigger earthquakes as well, but are much less frequently observed.

1.2 Motivations

Earthquake triggering holds major implication on the stress state of the lithosphere and its spatial-temporal variations, the underlying physics of earthquake nucleation [e.g., *Dieterich*, 1994], earthquake hazard assessment and mitigation [*Reasenberg and Jones*, 1989; *Gerstenberger et al.*, 2005]. Quantifying the stress state of the lithosphere is a long-standing problem and one of the grand challenges in seismological studies [*Lay et al.*, 2009], as it is essential to understanding the plate tectonics and earthquake cycle. Because earthquakes are easy to be triggered when they are close to the failure stage [*Brodsky and van der Elst*, 2014], studies on earthquake triggering in a large area can shed light on its spatial distribution of stress. Long-term monitoring of triggering phenomenon along certain faults may reveal temporal variations

of the stress state [e.g., *van der Elst et al.*, 2013]. Moreover, since the stress changes and timings of triggering are known in most cases, triggered earthquakes are ideal for studying the nucleation process of earthquakes. For example, the combination of Coulomb failure and rate/state friction successfully explained many observed triggering cases, especially aftershocks [*Dieterich*, 1994]. Finally, triggered earthquakes may impose significant seismic hazard as well. It was suggested that dynamically triggered earthquakes can be as large as M7 [*Pollitz et al.*, 2012b]. In addition, the M6.5 Big Bear earthquake occurred a few hours after the 1992 M7.3 Landers earthquake in southern California and was believed to be triggered [*King et al.*, 1994]. Similarly, the 2013 M6.6 Lushan earthquake may be linked with the 2008 M7.9 Wenchuan earthquake through static stress transfer [*Parsons and Segou*, 2014]. Hence, a better understanding of triggering mechanisms can greatly improve the ability to forecast and mitigate seismic hazard following large earthquakes.

During my Ph.D. work, I conducted a systematic investigation on a wide spectrum of earthquake triggering mechanisms, including static and dynamic triggering, creep and atmospheric pressure changes, in both interplate and intraplate regions (Figure 1.1). These studies provide new evidences on the co-existence of multiple triggering mechanisms and their relative importance.

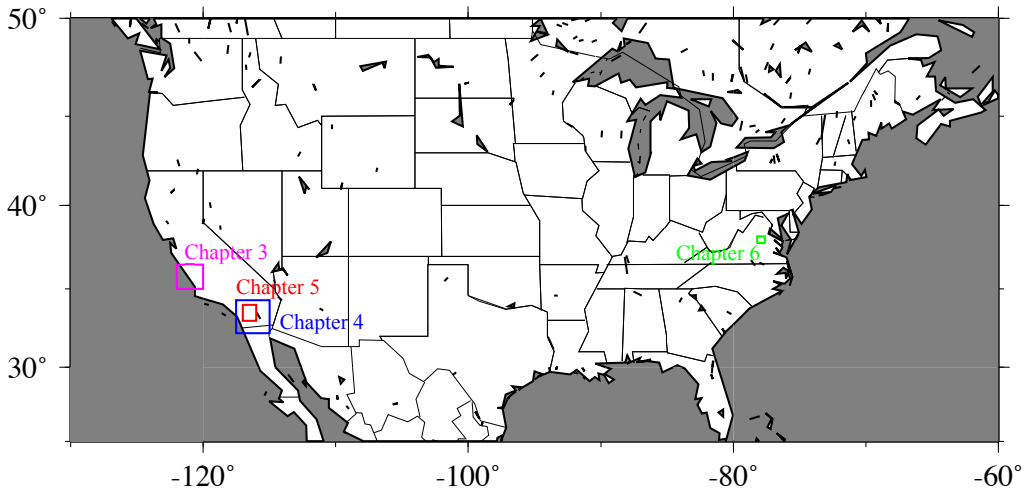

Figure 1.1 Map of United States of America. Rectangles denote to study regions of my PhD work.

1.3 Thesis Organization

My thesis primarily consists of three published papers [*Meng et al.*, 2012; *Meng et al.*, 2013; *Meng and Peng*, 2014] and two manuscripts in preparation [*Meng and Peng*, 2015; *Meng et al.*, 2015]. In Chapter 2, I introduce the waveform-based matched filter technique and its GPU implementation. In Chapter 3, I present the study of seismicity rate changes near Parkfield along the SAF following the 2003 San Simeon earthquake. Chapter 4 describes the co-existence of static and dynamic triggering in southern California following the 2010 El Mayor-Cucapah earthquake. In Chapter 5, I present evidence of deep creep near the Anza gap along the SJF by examining the aftershock zone of moderate-size earthquakes. Chapter 6 focuses on the aftershock sequence of the 2011 Virginia earthquake, which are likely affected by hurricane Irene.

CHAPTER 2

THE GPU-BASED MATCHED FILTER TECHNIQUE

2.1 Introduction

More than 15 years ago, earthquake data was mostly recorded only when the shaking exceeded certain threshold, known as triggered mode. Thanks to the recent development of cheap and massive data storage devices, earthquake data is now routinely recorded as continuous mode. The resulting data explosion has opened up many new exciting research areas in the field of seismology, such as detection of deep tectonic tremor (previously known as non-volcanic tremor) along major plate boundary faults [*Obara*, 2002; *Peng and Gomberg*, 2010] and imaging of subsurface structures based on cross-correlation of continuous ambient noise recordings [*Shapiro et al.*, 2005]. Another example of such new area is detecting microearthquakes that are not listed in existing earthquake catalogs [*Peng and Zhao*, 2009]. Traditionally, earthquakes were identified through hand-picking and association of seismic phases. However, immediately after a large earthquake or during an earthquake swarm, seismicity rate is extremely high, and seismograms from individual earthquakes tend to overlap with each other. In this case, it is extremely difficult to manually pick and locate all earthquakes, resulting in an incomplete earthquake catalog. Recovering those missing events and obtaining a more complete catalog are not only important for understanding physical mechanism of earthquake interaction [*Stein*, 1999; 2003; *Hill and Prejean*, 2007], but also useful for seismic hazard forecasting and mitigation [*Reasenberg and Jones*, 1989; *Gerstenberger et al.*, 2005].

Earthquakes that occur close to each other and have similar focal mechanism will generate similar waveforms at the same seismic stations. Therefore, an effective way to detect missing earthquakes is to use waveforms of previously identified earthquakes as templates and scan through continuous seismic recordings. This is also known as the matched filter technique [*Gibbons and Ringdal*, 2006; *Shelly et al.*, 2007]. A new seismic event is identified when the waveform similarity between a template event and continuous recordings exceeds certain threshold. However, this technique could be very computational intensive. For example, for a standard desktop computer with 2.27 GHz Xeon processor and 64 GB memory, it takes about 1.5 minutes to scan through 1-day-long continuous data for one template event recorded at 6 3-channel seismic stations with sampling rate of 100 Hz. For 2000 template events, it would take ~50 CPU hours (or ~2 days) to scan through 1-day-long continuous data on the desktop computer. The computational complexity is therefore a major bottleneck that prevents this technique from being applied at a massive scale – typically involving thousands of template events and years of continuously recorded data.

To reduce computation times, I use GPU parallel computing to accelerate the matched filter technique. GPU computing has recently evolved from a fixed-function graphical device into a highly programmable parallel processor and has been successfully deployed to accelerate a broad range of scientific applications [*Macedonia*, 2003; *Buck*, 2007; *Owens et al.*, 2008; *Nickolls and Dally*, 2010]. The matched filter technique exhibits regular computation and memory access patterns and is mostly data parallel, which makes the computation ideal for GPU processing. My results show that GPU algorithm achieves ~40 times speedup over a single CPU core. By using 30 Nvidia

C2070 cards on supercomputing cluster 'Keeneland', the GPU-based method achieves the equivalent performance of 1200 quad-core processors. In this chapter, I describe the standard procedure of the matched filter technique and the GPU implementation.

2.2 Standard Procedure

The standard procedure of the waveform-based matched filter technique was established by *Shelly et al.* [2007] and *Peng and Zhao* [2009] and is briefly described as follows. First, apply the same band-pass filter (e.g., 2-8 Hz or 10-40 Hz) to continuous data and template events to enhance locally generated seismic signals. Then, compute the signal-to-noise ratio (SNR) at all channels for each template event, and channels with low SNR (i.e., SNR<5) are removed. Next, compute the correlation coefficient (CC) in a short time window (e.g., 4 s or 6 s) between the template and continuous waveforms:

$$CC = \frac{\sum_{t_0}^{t_1}[(X(t)-\bar{X})*(Y(t)-\bar{Y})]}{\sqrt{\sum_{t_0}^{t_1}(X(t)-\bar{X})^2 * \sum_{t_0}^{t_1}(Y(t)-\bar{Y})^2}} \quad (2.1)$$

where t_0 and t_1 is the start and end time of the correlation time window, respectively. *X(t)* and *Y(t)* is the time series for the template and continuous waveforms, respectively. The template is set to be around *P*- or *S*-wave arrival times. Then, shift the CC back to the origin time of the template event by subtracting *P*- or *S*-wave arrival time. Next, computation moves forward by one data point and repeats for the entire continuous waveform. After scan through continuous data for all channels, stack all correlation traces to obtain the mean correlation trace. Then, compute the median absolute deviation (MAD) for each mean correlation trace and use 9 times the MAD as the detection threshold. For a normal distribution, the probability of exceeding 9 times the MAD is 6.4×10^{-10}, suggesting that a random detection is unlikely. Finally, combine detections

from all templates. For multiple detections with small time intervals, only the one with the highest CC is kept. The magnitude of the detected event is computed based on the median value of the maximum amplitude ratios between the detected and template event among all channels. The hypocenter of the detected event is assigned to be the same with the corresponding template. Figure 2.1 shows a positive detection along the San Jacinto Fault after the 2010 M_w 7.2 El Mayor-Cucapah earthquake.

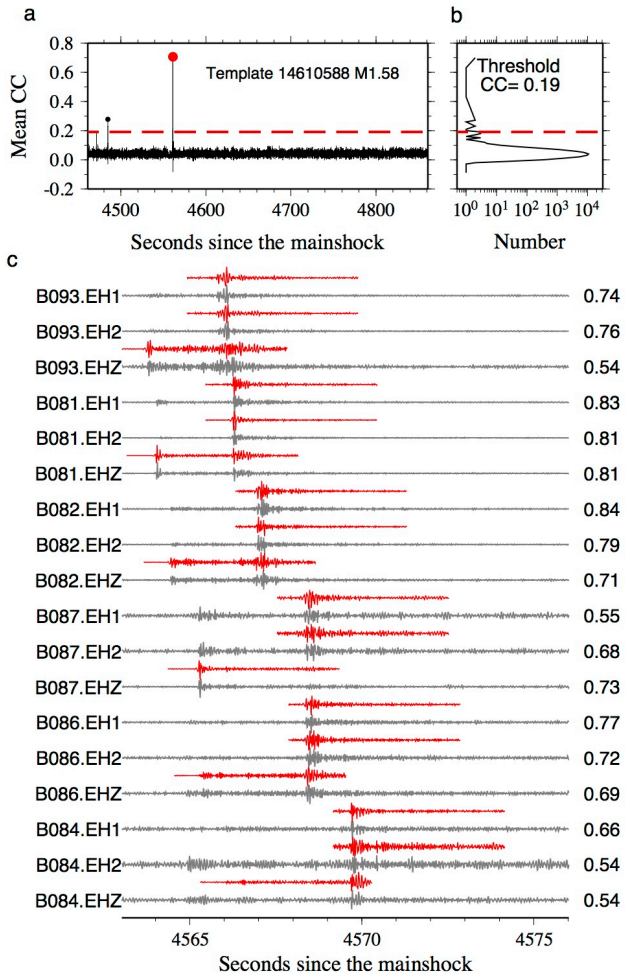

Figure 2.1 An example of a newly detected event in the San Jacinto Fault Zone. (a) Mean CC trace since the 2010 M_w 7.2 El Mayor-Cucapah earthquake. The red dot corresponds to the detected event at ~4,561 s after the mainshock. The red dashed line denotes the threshold of detected events. (b) The histogram of the mean CC trace. (c) A comparison

of the template waveforms (red) and the continuous waveforms (grey) around the origin time of the detected event in (a). The vertical dashed line represents the origin time of the detected event. The channel names and the corresponding CCs are labeled on the left and right sides, respectively.

2.3 GPU Implementation

To improve the computation efficiency of the matched filter technique, I explore the parallelism in the algorithm and use GPU-based systems to achieve significant acceleration, collaborating with Dr. Bo Hong and his group from the School of Electrical and Computer Engineering at Georgia Institute of Technology. The matched filter technique exhibits parallelism at multiple levels: there exists multiple templates, each of which needs to be matched with the continuous waveform data; the continuous waveform itself consists of a long sequence of windows of data points; both the templates and the continuous waveform data contain multiple channels of data recorded by multiple stations; further down the parallelism hierarchy, each channel consists of multiple data points, which forms the input for the correlation analysis.

To explore such hierarchy parallelism, I decompose the computation into multiple tasks that computes the correlation of a template and a window of continuous waveform data, where each task is to match one template with a window of continuous waveform of the same length. The design focus on two algorithmic aspects: (1) task grouping and allocation to the GPU cards, and (2) GPU code optimization for each task.

2.3.1 Task Grouping and Allocation

To allocate the tasks onto GPU cards, the allocation strategy needs to focus on three aspects: (1) Each group should not exceed the GPU card memory capacity; (2) The allocation strategy should cover all the tasks and balance among groups; (3) The

allocation strategy should minimize the cost of communication and redundant computation.

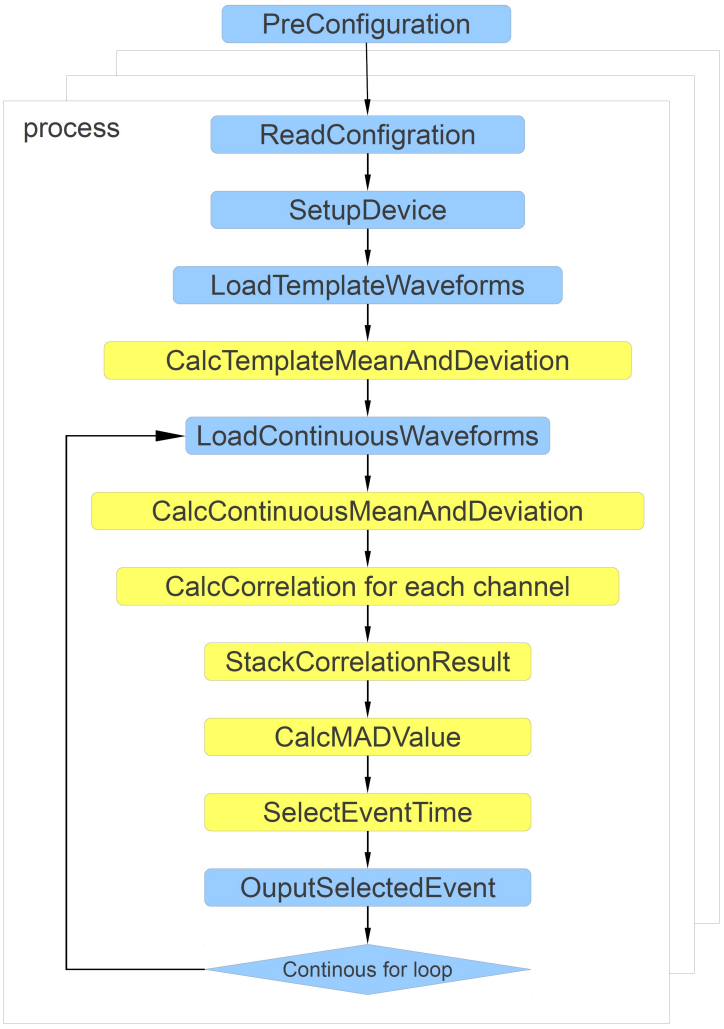

Figure 2.2 Program routines and control flow. Blue blocks represent CPU routines, and yellow blocks represent GPU routines. After Preconfiguration, CPU processes launch a series of routines in parallel.

The first aspect guarantees each GPU card has enough memory to contain the data, including input, output and temporary for the execution. The second aspect ensures that all the tasks are dispatched to a GPU card and the computation time for all GPU cards are relatively equal. For the third aspect, as is illustrated in Figure 2.2, the computation of

each task requires data preparation and movement. Thus a desirable allocation strategy is expected to minimize those costs. Additionally, tasks shared some of their computations. For example, the mean value and variance of a template is shared when matching this template to multiple windows of continuous waveform. The same sharing applies to the continuous waveform as well. It is thus undesirable to repeat such computation when matching each pair of template and continuous waveform. In the task allocation strategy, information about task sizes is used to calculate the memory need so as to maximize the number of tasks that a GPU card can process. Because the templates are of the same size, load balance of multiple GPU cards is relatively easy. Allocating the same number of tasks to the GPU cards would ensure the same computation time.

The cost of data movement and shared computation is minimized as follows. Each task of the correlation computation can be indexed by a tuple (i, j) where i represents the template index and j the continuous waveform. The group size of tasks can also be represented by a tuple (p_i, p_j) so that each card will calculate on p_i templates and p_j continuous waveforms. The group size of tasks (p_i, p_j) should be a solution for the optimization problem,

$$min[(k_{copy\_t} + k_{es\_t}) * p_i + (k_{copy\_c} + k_{es\_c}) * p_j] \tag{2.2}$$

where k_{copy_t} and k_{es_t} are the coefficients for consumed time on copying and calculating mean and variance value for template waveform, and similarly k_{copy_c} and k_{es_c} for continuous waveform. Under the constraints,

$$p_i p_j N_p = N_t N_c \tag{2.3}$$

$$k_{size\_t} p_i + k_{size\_c} p_j \leq C \tag{2.4}$$

$$0 \leq p_i \leq N_t \tag{2.5}$$

$$0 \le p_j \le N_c \tag{2.6}$$

where N_p is the total number of groups; N_t is total number of template waveforms and N_c of continuous waveforms; k_{size_t} is the size of each template data and k_{size_c} is the size of continuous data; C is the GPU memory capacity. The solution to the problem is,

$$p_{i,opt} = \sqrt{\frac{k_{copy\_t}+k_{es\_t}}{k_{copy\_c}+k_{es\_c}} * \frac{N_t N_c}{N_p}} \tag{2.7}$$

$$p_{i,max} = min(N_t, \frac{C}{k_{size\_t}}) \tag{2.8}$$

$$p_{i,min} = max(\frac{N_p}{N_t}, \frac{N_t N_c k_{size\_t}}{N_p C}) \tag{2.9}$$

$$p_{i,optimize} = \begin{cases} p_{i,max}, & if\ p_{i,max} \le p_{i,opt} \\ p_{i,min}, & if\ p_{i,min} \ge p_{i,opt} \\ p_{i,opt}, & if\ p_{i,min} \le p_{i,opt} \le p_{i,max} \end{cases} \tag{2.10}$$

$$p_{j,optimize} = \frac{N_t N_c}{N_p p_{i,optimize}} \tag{2.11}$$

Since the ratio between the data size and the cost of copying time and computation time is approximately fixed, the task allocation strategy can find a solution to minimize the cost based on the data size information collected using Equation (2.2).

2.3.2 GPU Computation Kernels

For a group of tasks (computes the correlation of a template and a window of continuous waveform data) on one GPU card, fine-grained multiple-threaded kernel routines are designed for the GPUs. The design of the kernels mostly concern memory coalescing and shared memory usage. To efficiently utilize the GPU resource, threads should access the global memory in a coalesced pattern, i.e., neighboring threads should access continuous memory addresses. Moreover, shared memory access has a much lower latency than global memory and therefore reusable data should be loaded into

shared memory to improve the performance. Kernels in the program have different memory access patterns, and thus have different coalescing and sharing strategies. The design focuses on the computation of correlation routine (the *CalcCorrelation* function) that dominates the execution time. This computation iterates through all the stations and continuous window pairs to calculate the correlation values. To coalesce the memory access, I reorganize the template data layout so that neighboring template data in the global memory are of different station. Using this data layout, neighboring threads working on different correlation pairs can access different template data in a coalesced manner. The kernel threads also have shared memory accesses to continuous data such that it is beneficial to load continuous data into shared memory. Other kernel routines memory access patterns are adjusted and coalesced to accommodate this memory layout.

Another design factor is the configuration of grid size and block size. In CUDA GPU programming model, large number of threads are grouped into blocks and one kernel routine can launch multiple blocks. Different block size and grid size can affect the performance of kernel because of the hardware resource allocation (e.g., number of registers) for each thread. Currently, I configure the kernels with 56 blocks and 1024 threads manually for Nvidia Tesla C2070 card. The execution time of each kernel is monitored at runtime and the program is designed to be extendible to dynamically reconfigure for other generation of GPU cards or application parameters.

CHAPTER 3

SEISMICITY AROUND PARKFIELD CORRELATES WITH STATIC SHEAR STRESS CHANGES FOLLOWING THE 2003 M_W 6.5 SAN SIMEON EARTHQUAKE

3.1 Introduction

The 2003 M_w 6.5 San Simeon earthquake struck the central California coast on 22 December 2003, 19:15:56 UTC and induced large dynamic and static stress changes in its vicinity [*Hardebeck et al.*, 2004]. The mainshock ruptured a reverse fault striking northwest and dipping northeast and was followed by numerous aftershocks [*Hardebeck et al.*, 2004; *McLaren et al.*, 2008]. About nine months later, an M_w 6.0 earthquake occurred on the Parkfield section of the San Andreas Fault (SAF), ~50 km to the east of the San Simeon epicenter (Figure 3.1a). Because the two earthquakes occurred closely in space and time, it is reasonable to speculate that the San Simeon mainshock may have triggered the Parkfield earthquake. Indeed, the Parkfield section of the SAF experienced positive Coulomb stress changes on the order of 10 kPa (Figure 3.1a), suggesting that the static stress changes may explain their triggering relationship [*Aron and Hardebeck*, 2009]. However, the seismicity rate around Parkfield decreased slightly after the San Simeon earthquake [*Aron and Hardebeck*, 2009], which is inconsistent with either the static Coulomb hypothesis and dynamic stress changes.

Previous studies on earthquake triggering mostly utilize existing earthquake catalogs, which may be incomplete immediately following large earthquakes, mainly due to the intensive seismic activity and masking from the coda waves of the mainshock and

large aftershocks [*Peng et al.*, 2006; *Enescu et al.*, 2007; *Peng et al.*, 2007; *Aron and Hardebeck*, 2009; *Enescu et al.*, 2009]. So, the seismicity rate decrease around Parkfield could be due to the incompleteness of the Northern California Seismic Network (NCSN) catalog immediately after the San Simeon mainshock. Inspired by recent successes in detecting earthquakes and tectonic tremors based on the waveform matched filter technique [*Shelly et al.*, 2007; *Peng and Zhao*, 2009], I apply a modified version of this technique to systematically search for missing earthquakes around Parkfield using 13 borehole stations from High Resolution Seismic Network (HRSN), station PKD from Berkeley Digital Seismic Network (BK network) and 25 surface stations from Northern California Seismic Network (NC network) (Figure 3.1). With a more complete catalog, I can elucidate the genuine seismicity rate changes along the SAF.

3.2 Data and Methods

The continuous seismic data are recorded by 39 stations from the HRSN, BK and NC network around Parkfield (Figure 3.1). For HRSN stations, I use BP channels (short-period 3-component geophone recording at 20 sample/s). For station PKD, I use BH channels (broadband 3-component recording at 20 sample/s). For NC stations, I use the EHZ channel (short-period vertical component) down-sampled from 100 Hz to 20 Hz. The study period is 90 days before to 90 days after the San Simeon earthquake. On 6 November 2003, roughly one and a half months before the San Simeon earthquake, stations CCRB, LCCB, SCYB, and SMNB from HRSN had gain value changes, which caused a significant change in background noise level. Since 23 January 2004, 31 days after the San Simeon earthquake, 8 stations from NC network stopped recording. Because the 8 stations are all in the northwest side of the study region (Figure 3.1b), the detection

ability around these stations may be reduced after that day. Hence, although I use a total of 180 days of continuous waveforms, I primarily focus on the results from 46 days before to 31 days after the San Simeon mainshock. The continuous recordings are daily-long segment relative to the origin time of the San Simeon mainshock. When a significant data gap exists, the length of daily data is determined by the data availability.

I use 3531 earthquakes listed in the relocated catalog [*Thurber et al.*, 2006] within 5 km to the SAF as template events (Figure 3.1). These templates are the same with those used in a previous study [*Peng and Zhao*, 2009]. Templates waveforms are 1 s before and 5 s after the predicted *S*-wave arrival for two horizontal components, and 1s before and 5 s after the predicted *P*-wave arrival for the vertical component. The *P*- and *S*-wave arrival times are computed based on a 1D velocity model in this region [*Waldhauser et al.*, 2004]. In comparison, *Peng and Zhao* [2009] used 2 s before and after the predicted *S*-wave arrival for all three components. The motivation for such change is to enhance the ability of detecting local events along Parkfield section by enforcing a *S*–*P* time constraint. I compare the predicted *P*- and *S*-wave arrival times with the ones picked by Northern California Earthquake Data Center (NCEDC) and confirm that the initial *P*- and *S*-wave arrivals are included in the template time window.

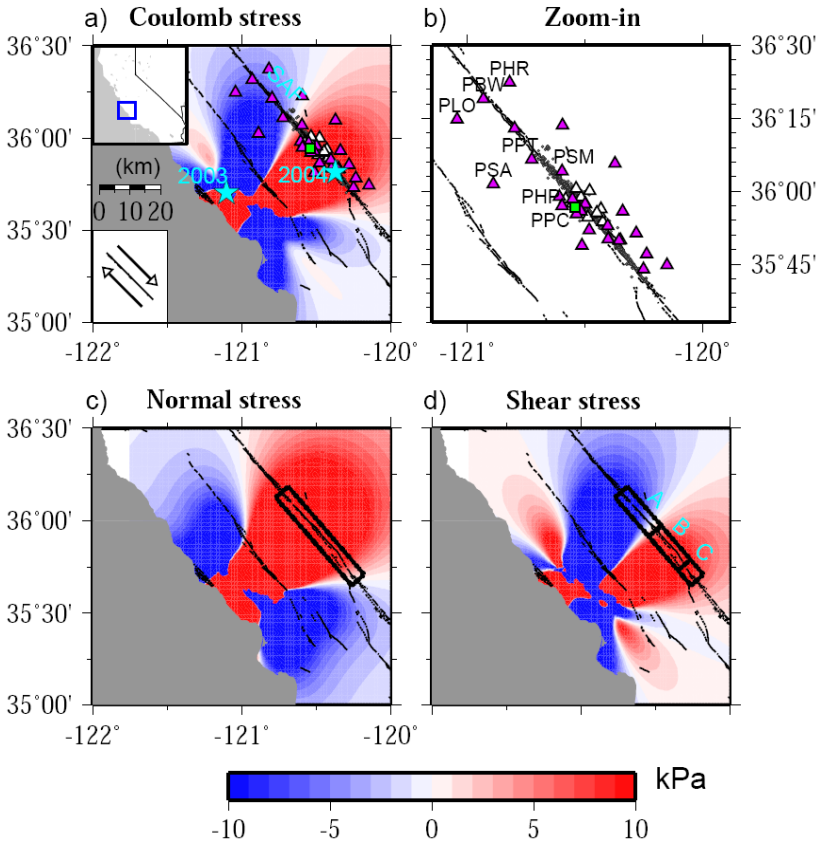

Figure 3.1 Map of central California. The color in the background represents static stress changes induced by the San Simeon earthquake at a depth of 7.5 km. The black lines represent major active faults, including the SAF. (a) The blue stars denote the epicenters of the 2003 M_w 6.5 San Simeon and the 2004 M_w 6.0 Parkfield earthquakes. The grey dots represent 3531 template events. The white triangles represent 13 borehole stations in the HRSN. The magenta triangles represent 25 stations from NC network. Green square represents station PKD from BK network. The lower left inset shows the geometry of receiving faults in central California and the top left inset shows the map of California. (b) The zoom-in figure illustrates the relative location between stations and template events. (c) The black box marks the study region, the along-strike distance between −50 and 20 km relative to the epicenter of the 2004 Parkfield earthquake, and within 5 km to the SAF. (d) The boxes and letters denote three sub-regions.

3.3 Self-detections

Ideally, template events should detect themselves with CC≈1.0, which are referred as perfect self-detection. Evaluating if all the perfect self-detections can be achieved is the best way to examine potential problems in data set and/or analysis procedure. A total

of 198 template events occurred during the 180-day study period. Using the original daily-long continuous data, however, none produces perfect self-detection (Figure 3.2a). The primary cause is the subtle differences in the beginning time of daily-long continuous data among stations. After adding it to the predicted *P*- or *S*-wave arrival time, dividing by sampling rate and rounding, it may cause one data point difference. As a result, the best correlating window of different channels may not be aligned at the same time point, which will significantly lower the mean CC value.

I use the following procedures to fix this problem. First, I shift the reference time of continuous data of all stations to a common time (i.e., middle night at each day). Next, I cut the data so that they have the same starting time to the nearest 0.05 s, which help to reduce the minor starting-time differences among stations. With the corrected continuous data, 152 out of 198 template events can produce perfect self-detections (Figure 3.2a). In order to have all 198 templates achieve perfect self-detections, I allow one data-point shift while stacking. That is, at each time point the highest CC value among itself and its two neighboring points is used for stacking. This is very helpful for achieving all perfect self-detections (Figure 3.2a). More importantly, some local events may not be detected if the best correlating windows of all channels are not aligned at the same time point (Figure 3.2). In this way, I ensure that the best-correlating windows of all channels are stacked together.

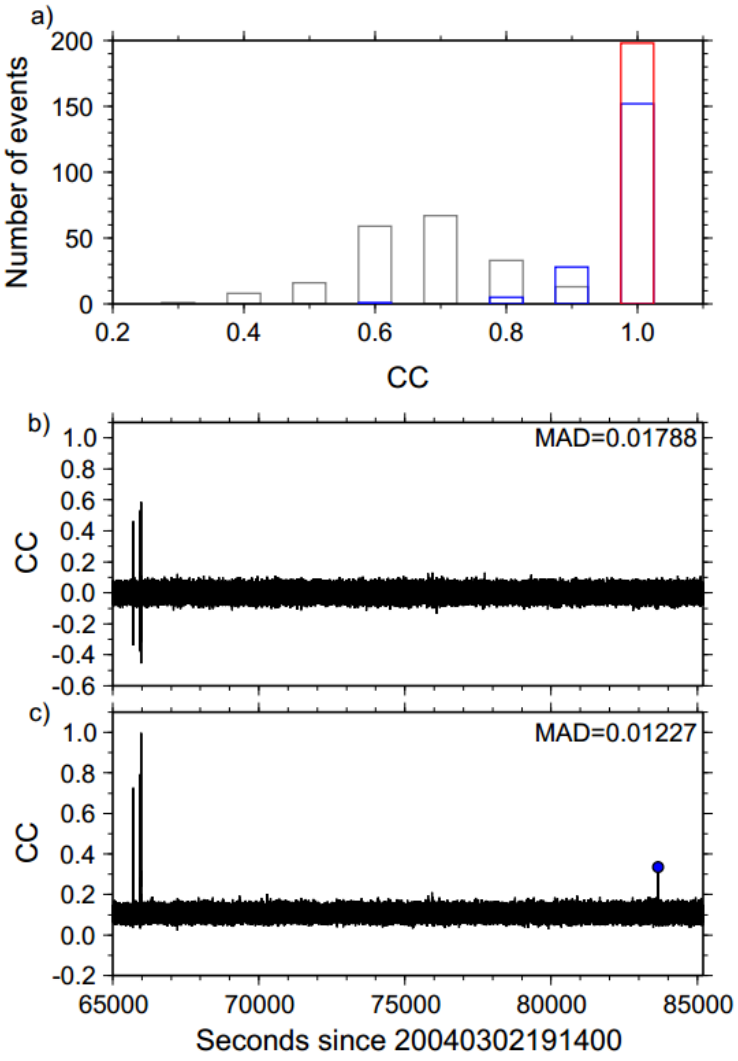

Figure 3.2 (a) The histogram of CC values for 198 self-detections using the original (grey), corrected continuous data (blue) and allowing one data point shift while stacking (red), respectively. (b) and (c) Comparison of mean CC traces before and after allowing one data point shift while stacking by correlating waveforms form an template event 20040303133331 with daily-long continuous data from 2 March 2004 19:14:00, respectively.

3.4 False Detections

Previous studies using the same technique generally define the threshold of positive detections as the sum of the median value and 8 or 9 times the median absolute deviation (MAD) of the mean CC trace [*Shelly et al.*, 2007; *Peng and Zhao*, 2009].

However, allowing one data point shift while stacking would lower the MAD value of mean CC trace. Hence a higher threshold should be applied in this study. I first select 12 times the MAD as threshold, which is roughly equivalent to 8 or 9 times the MAD in previous studies.

Figure 3.3 illustrates a possible 'false detection' using the sum of median value and 12 times the MAD as threshold. The detected event occurred ~42 days after the San Simeon mainshock and was detected by a template beneath Middle Mountain with a mean CC value of 0.21. The correlated window of continuous waveforms appears to be a segment of seismic signals with much longer duration, indicating a distant source. According to the NCSN catalog, an aftershock of magnitude 1.46 occurred in the San Simeon rupture zone just ~7 s prior to this detection. I confirm that the event indeed is the San Simeon aftershock by predicting the *P*- and *S*-wave arrival times of the San Simeon aftershock at all stations. It appears that the template correlates with the *P*-wave train of the San Simeon aftershock. Hence, this kind of detection of a San Simeon aftershock is considered as 'false detections'.

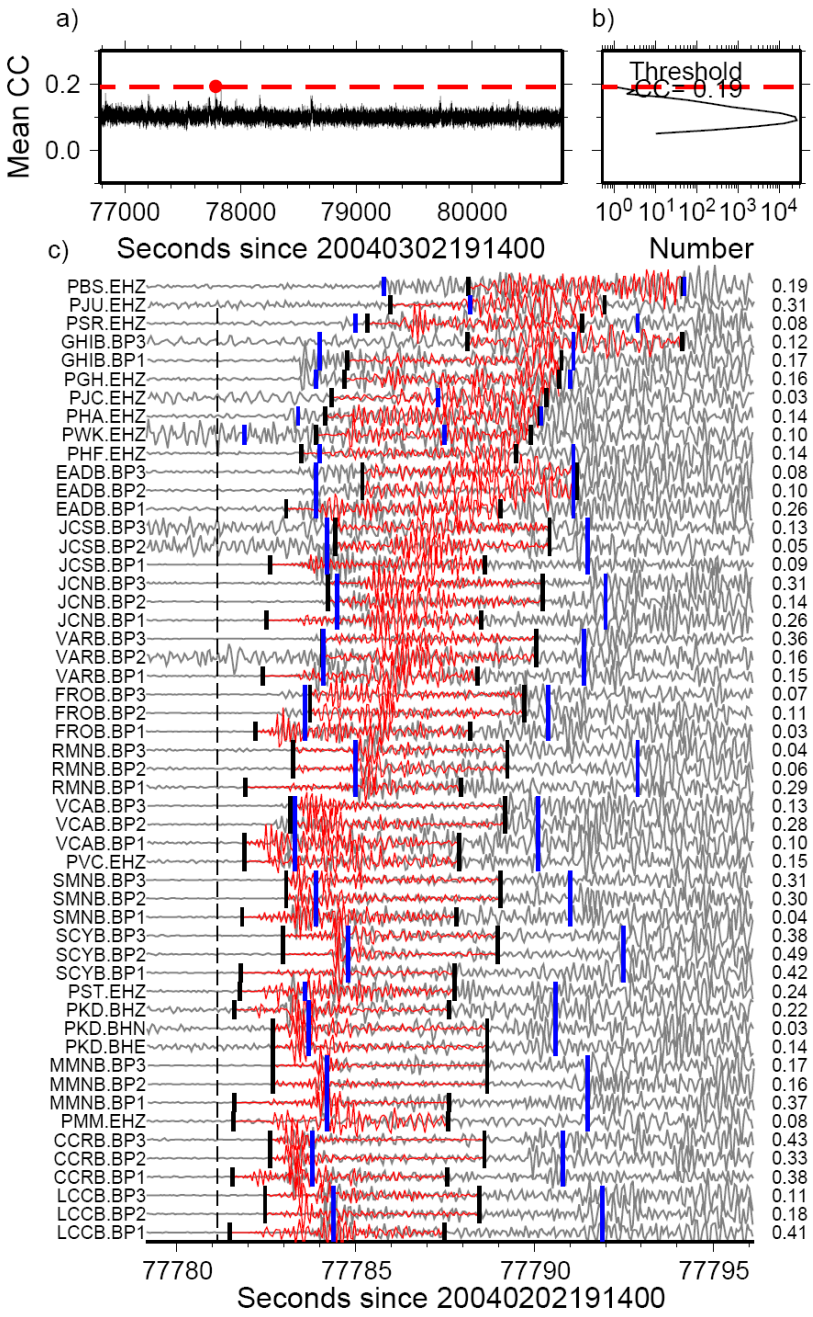

Figure 3.3 Example of a 'false detection' after the San Simeon mainshock. (a) Mean CC trace versus seconds since 2 February 2004 19:14:00 for the template 20040929004616. The red dot corresponds to the detected event. (b) The histogram of the mean CC trace. (c) The blue vertical lines denote the predicted *P*- and *S*-wave arrival times of one San Simeon aftershock occurred on 03 February 2004 16:50:14 listed in the NCSN catalog.

Figure 3.4 shows spatio-temporal distributions of all detected events around the San Simeon mainshock by using a threshold of 12 times the MAD. Many seismic events were detected by templates beneath Middle Mountain (near station MMNB) after the San Simeon mainshock. Most of them have very low CC values, suggesting that they are likely 'false detections'. I hypothesize that a similar moveout (i.e., increasing travel times with distances) between template events along the SAF and the San Simeon aftershocks is most likely the cause of 'false detections'. To test this, I randomly select one San Simeon aftershock and compute its *P*- and *S*-wave arrival times at all stations based on the 1D velocity model [*Waldhauser et al.*, 2004]. I then measure the similarity of moveout by calculating the root mean square (RMS) of the relative arrival time differences at all stations between the San Simeon aftershock and templates. The smaller the RMS value is, the more similar the moveout between a San Simeon aftershock and template is.

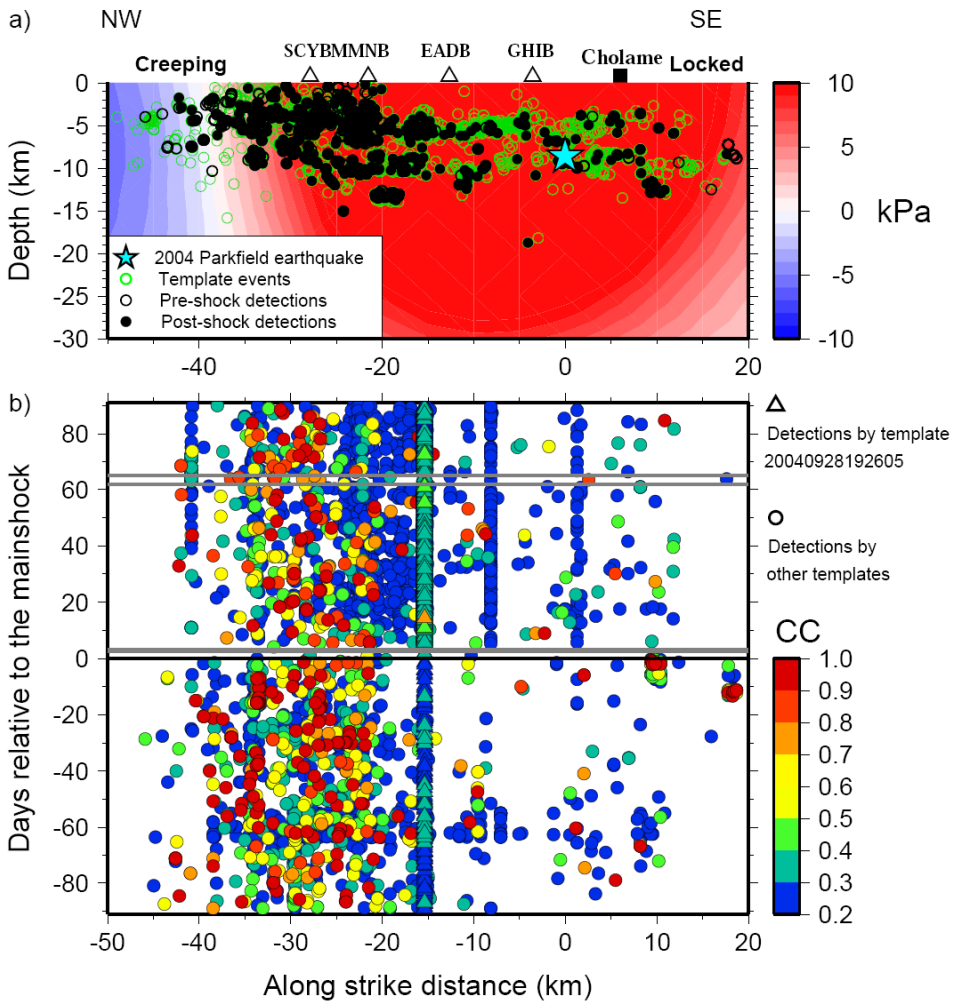

Figure 3.4 (a) The cross-section view of all template events (green) and detected events (black) along the SAF. The threshold is the sum of the median value and 12 times the MAD of mean CC trace. The contours in the background denote the Coulomb stress changes induced by the San Simeon mainshock. (b) Spatio-temporal relationship of all positive detections, which are color-coded by the CC values. The triangles denote to the detected events by template 20040928192605.

Templates with the along-strike distances between -26 km and -10 km tend to have the smallest RMS value (the most similar moveout) with the San Simeon aftershock, where large numbers of 'false detections' are also found following the mainshock. As noted before, such 'false detections' have very low CC values. By increasing the threshold to be the sum of the median value and 15 times the MAD of mean CC trace,

almost all the 'false detections' can be removed. 15 times the MAD in this study is roughly equivalent to 11 or 12 times the MAD in previous studies. The selection of threshold is a tradeoff between the number of detected events and possibility of 'false detections'. By applying a higher threshold, I ensure that 'false detections' are discarded. However some local events might be excluded as well.

Even after removing false detections by raising the threshold to 15 times the MAD, template 20040928192605 still detected ~2800 events, most of which have very low CC values (triangles in Figure 3.4). Template 20040928192605, which correlates with the *P*-wave of an M_d1.78 event listed in NCSN catalog that occurred ~80 km away. The main reason for the unusual high number of detections by this template is that its waveforms have relatively low amplitudes during most of the 6 s time window and large impulsive signals near the end. This results in 'false detection' of the *P*-wave from a distant event. In fact, the impulsive arrivals near the end of the correlating time window actually are from another template 20040928192610, which occurred ~5 s later and ~0.05 km away according to NCSN catalog. By comparing the waveforms of the two templates, it is clear that template 20040928192605 is problematic. Therefore, I remove all detected events by template 20040928192605. I have checked other templates and do not find similar problems.

3.5 Detections in Higher Frequency Range

After removing all possible 'false detections', 1664 detected events are left (Figure 3.5). I finally check all of them in higher frequency range using DP channels (3-component geophone recording at 250 Hz) of HRSN stations. I apply 10-25 Hz band-pass filter to the continuous waveforms and templates recorded by the DP channels. I use this

frequency range because high-frequency signals from distant events (i.e., San Simeon aftershocks) would be attenuated more as compared with local events. Hence, this frequency range would favor detections of local signals on or near the SAF. Next, for each of the 1664 event, I repeat the same detecting procedure with its 'matching template' in DP channels. As a result, 95%, 87%, 82% of remained events can also be detected in 10-25 Hz frequency range when the threshold is set to be the sum of median value and 9, 12, 15 times the MAD of mean CC trace, respectively. The numbers suggest that the majority of the detected events in the 2-8 Hz band could also be detected in the 10-25 Hz band. Because higher frequency seismic signals are less coherent, the correlation between templates and continuous data in higher frequency range is usually lower than in lower frequency range. Hence, the smaller number of positive detections is expected. For the remaining of this paper, I use the 1664 earthquakes detected by a 2-8 Hz band-pass filter.

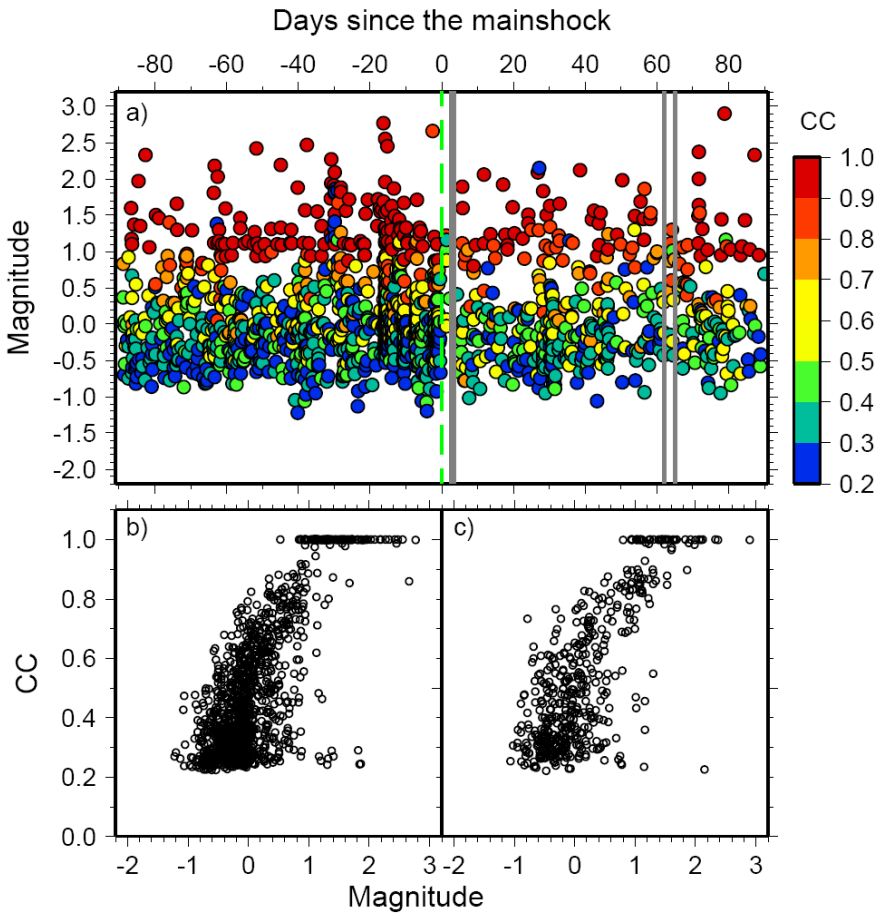

Figure 3.5 The CC and magnitude of all detected events. (a) The magnitude of detected events versus days relative to the mainshock, color-coded by the CC. The green dashed line marks the origin time of the San Simeon mainshock. The grey shaded areas denote to the data gaps of the continuous data. (b) and (c) The CC versus magnitude of detected events before and after the mainshock, respectively.

3.6 Results

The CC-magnitude relationship of detected events before and after the San Simeon mainshock shows essentially the same pattern (Figure 3.5). For same magnitude, no clear decrease of CC can be observed for events that occurred after the mainshock, suggesting no obvious change in detection ability. During the same period, 201 and 198 events were listed in the NCSN and relocated catalog [*Thurber et al.*, 2006], respectively.

As briefly mentioned before, the primary study period for investigating seismicity rate changes is chosen from 46 days before the mainshock, when the network change completed, to 31 days after the mainshock, when 8 NC stations stopped recording. Among 1664 detected events, 1046 events occurred during the primary study period. Figure 3.6a shows the locations of the 1046 detected events in cross-section along the SAF strike. Most of the detected events occurred beneath Stone Canyon (station SCYB) and Middle Mountain (station MMNB). In contrast, there were only a few detected events further northwest in the creeping section and southeast of Gold Hill (station GHIB) near Cholame.

3.6.1 Spatio-temporal Changes of Seismicity

The spatio-temporal evolution of the events shows a marked difference along the SAF strike (Figure 3.6b). Based on the distinct pre-shock behavior of seismicity, I divide the study area into three sub-regions and quantify the seismicity rate changes by computing β-value, which is a measure of the difference between the observed number of events after the mainshock and the expected number from the background rate before the mainshock [*Kilb et al.*, 2002; *Aron and Hardebeck*, 2009]. I also compute the seismicity ratio, which is simply the ratio between the average post-mainshock rate and pre-mainshock rate [*Shelly and Johnson*, 2011]. I compute the magnitude of completeness (M_c) of -0.3, 0, and 0.6 for sub-region A, B, and C using the best-combined method in ZMAP [*Wiemer*, 2001], respectively. I recognize that the obtained M_c may be inaccurate and have temporal variations. Moreover, β-value and seismicity ratio may strongly depend on M_c, hence I compute β-value and seismicity ratio by setting the cutoff magnitude from -1.6 to 2 to avoid potential bias.

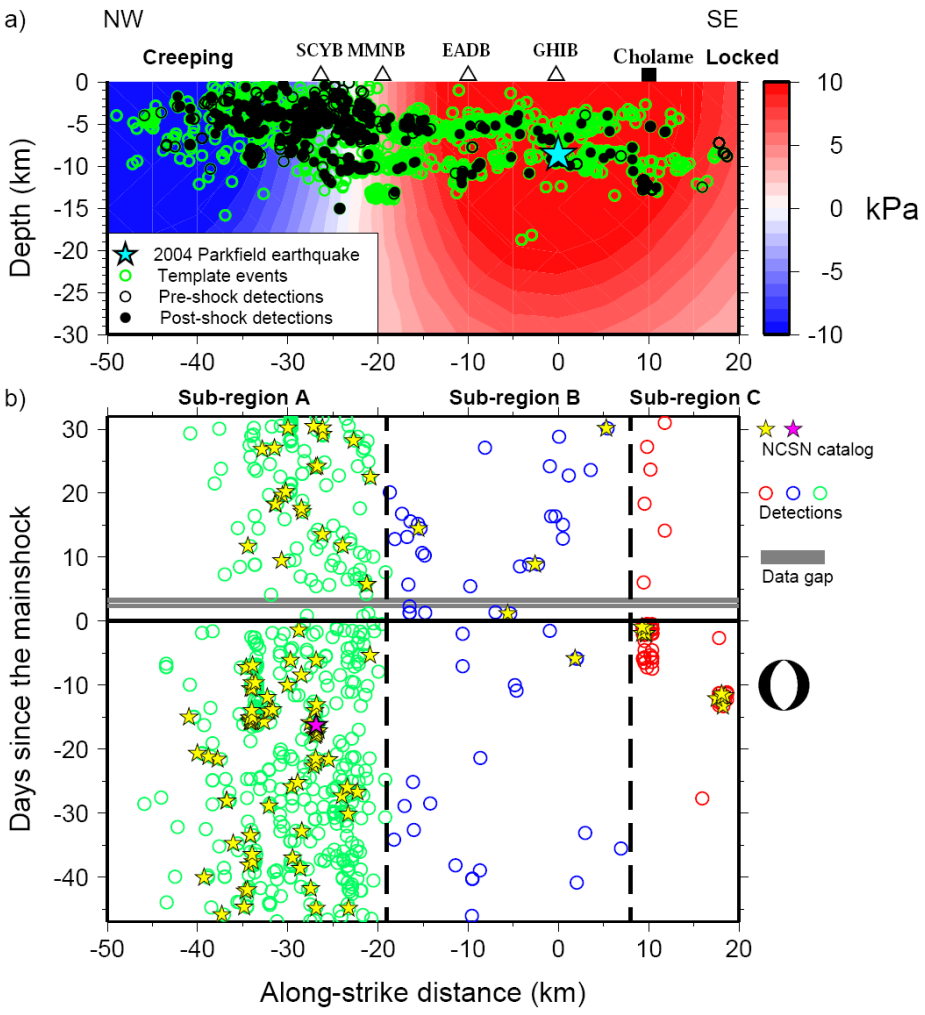

Figure 3.6 Spatio-temporal evolution of detected events from 46 days before to 31 days after the San Simeon earthquake. (a) The cross-section view of all templates (green) and detected events (black) along the SAF. The background contour denotes the static shear stress changes induced by the mainshock. (b) The origin times of all detected events relative to the mainshock (horizontal black line) versus their along-strike distances. The magenta star denotes the M_d 2.77 earthquake occurred ~16 days before the mainshock. The beach ball denotes the focal mechanism of the first earthquake in the swarm occurred around the along-strike distance of 18 km.

In sub-region A (northwest of Middle Mountain, less than −19 km in the along-strike distance), I find a clear seismicity rate decrease across all magnitude bands (Figure 3.7b and c). However, such a decrease may be caused by an abrupt jump in cumulative number ~16 days before the mainshock due to an M_d 2.77 earthquake and its aftershocks

(Figure 3.7a). To further evaluate this, I exclude the time window from the M_d 2.77 earthquake to the San Simeon mainshock and re-calculate β-value and seismicity ratio. For all magnitude bands, the decrease of seismicity rate is still significant at the 95% confidence level (i.e., $\beta<-2$) even after excluding the M_d 2.77 earthquake sequence (Figure 3.7b). Moreover, I predict the expected decay of the aftershock sequence of the M_d 2.77 earthquake after the San Simeon mainshock by fitting the modified Omori's law [*Omori*, 1894; *Utsu et al.*, 1995; *Wiemer*, 2001] using events that preceded the mainshock (Figure 3.7a). The aftershock sequence appeared to be slightly stifled by the San Simeon mainshock for ~30 days. I also examine the potential impact on the Parkfield seismicity patterns by the M_d 2.77 earthquake sequence. I compare the magnitude distributions of detected events before and after the San Simeon mainshock and find no clear change caused by the M_d 2.77 earthquake.

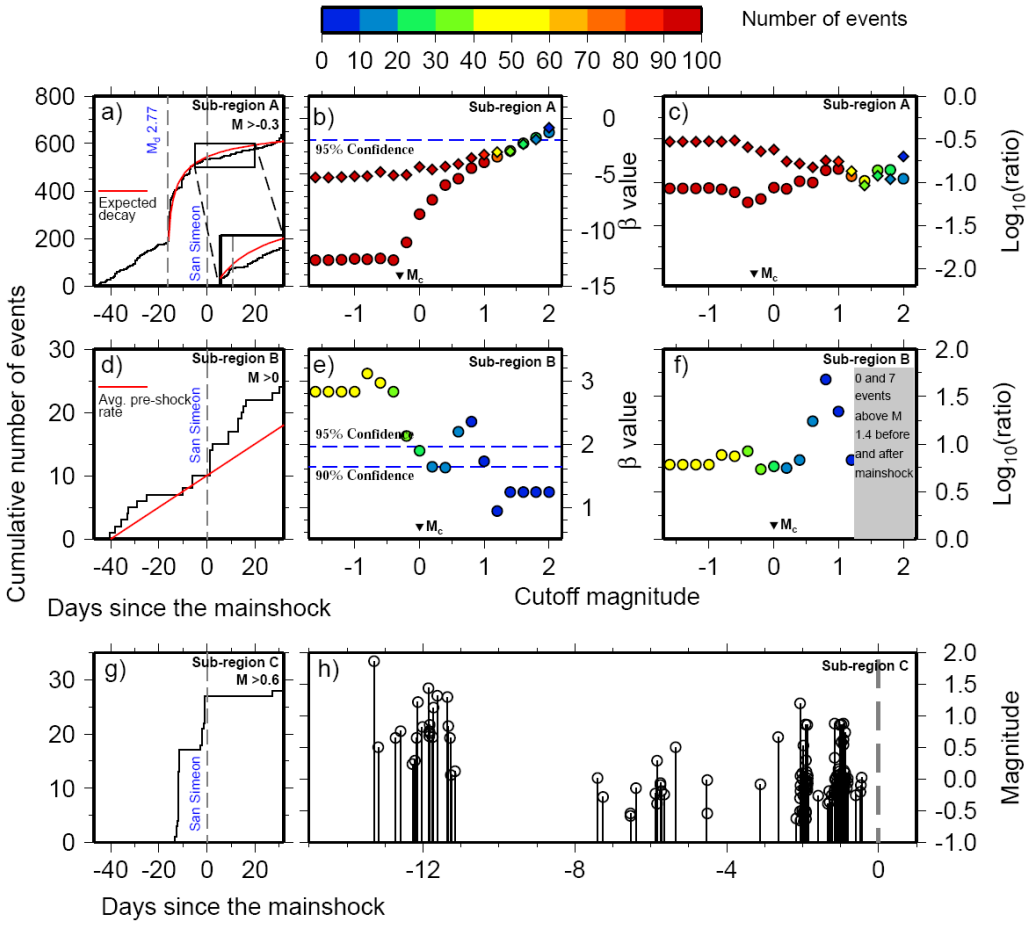

Figure 3.7 Cumulative numbers of earthquakes and corresponding statistical analysis in three sub-regions. (a), (d), and (g) The cumulative number of detected events above M_c in sub-region A, B and C versus days relative to the mainshock, respectively. (b) and (e) β−values versus cutoff magnitude with detected events in sub-region A and B, respectively. Dots denote that background rate is measured prior to the San Simeon earthquake. Diamonds denote that background rate is measured prior to the M_d 2.77 event. (c) and (f) The seismicity ratios versus cutoff magnitude with detected events in sub-region A and B, respectively. (h) The magnitude of detected earthquake swarms in sub-region C immediately before the mainshock.

Finally, the significance of the seismicity rate decrease in sub-region A is also evident in the smoothed β-value changes using all the events listed in the NCSN catalog from 1984 to 2009 (Figure 3.8a). The computing time window is set to be the same as the primary study period (46 days before and 31 days after any given time). The time

window moves forward by 10 data points. I obtain a M_c of 1.2 in this sub-region using the best-combined method in ZMAP [*Wiemer*, 2001] and compute the smoothed β-value changes with events above M_c (Figure 3.8b). The β-values obtained from the detected events in both cases are above two standard deviations, suggesting that the seismicity rate changes around the San Simeon mainshock were indeed abnormal.

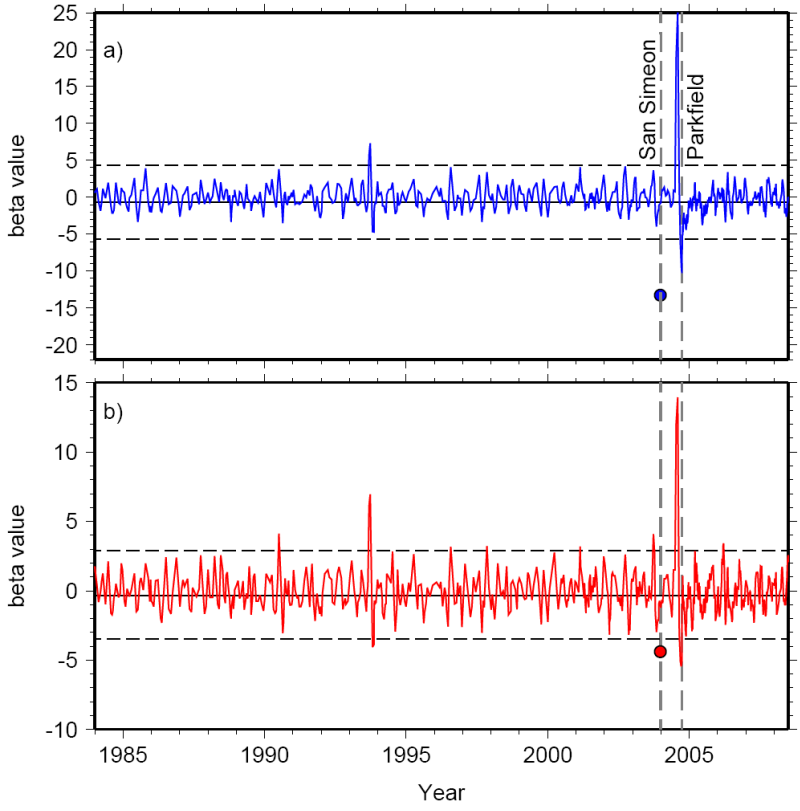

Figure 3.8 The smoothed β-value changes in sub-region A with events listed in the NCSN catalog. (a) β-values versus year using all events in sub-region A from 1984 to 2009 in the NCSN catalog. The blue dot marks the obtained β-value from the detected events. The horizontal solid and dashed lines denote the mean and two standard deviations of β-values prior to the 2004 Parkfield earthquake, respectively. (b) Same with (a) except only events above M_c of 1.2 are used.

The seismic activity changed dramatically across Middle Mountain. In sub-region B (between Middle Mountain and Cholame, the along-strike distance between –19 km

and 8 km), only 21 and 30 seismic events occurred before and after the mainshock, respectively (Figure 3.6b). A significant increase of seismicity rate is evident at the 90% confidence level for cutoff magnitude less than 0 (Figure 3.7e). For cutoff magnitude larger than 0, β-values become statistically unreliable due to the small number of remaining events. The seismicity ratio increases for all cutoff magnitudes (Figure 3.7f).

In sub-region C (southeast of Cholame, with the along-strike distance of > 8 km), the seismicity was quiescent during most of the study period. A few swarms occurred at 15 and 10 days before the mainshock and completely stopped right before the origin time of the mainshock (Figure 3.6b). A dramatic decrease of seismicity rate is evident due to the earthquake swarms (Figure 3.7g and h). However, if I remove the swarm sequences, 2 and 6 events remained before and after the mainshock, respectively. I do not compute β value or seismicity ratio with only 8 events. Nevertheless, a moderate increase of seismicity rate after the mainshock can be inferred without the swarms.

3.6.2 Seismicity Rate Changes 90 Days Before and After the Mainshock

Although 4 HRSN stations experienced gain value changes at ~46 days before the mainshock and 8 NC stations stopped recording ~31 days after the mainshock, I still investigate whether there were significant differences in seismicity rate changes 90 days before to 90 days after the San Simeon earthquake. After extending the time window, the seismicity rate changes pattern remains essentially the same (Figure 3.9a). In particular, the seismicity rate reduction in sub-region A is still significant for most magnitude bands (Figure 3.9c and d). A minor to moderate increase of seismicity rate might be concluded in sub-region B (Figure 3.9f and g).

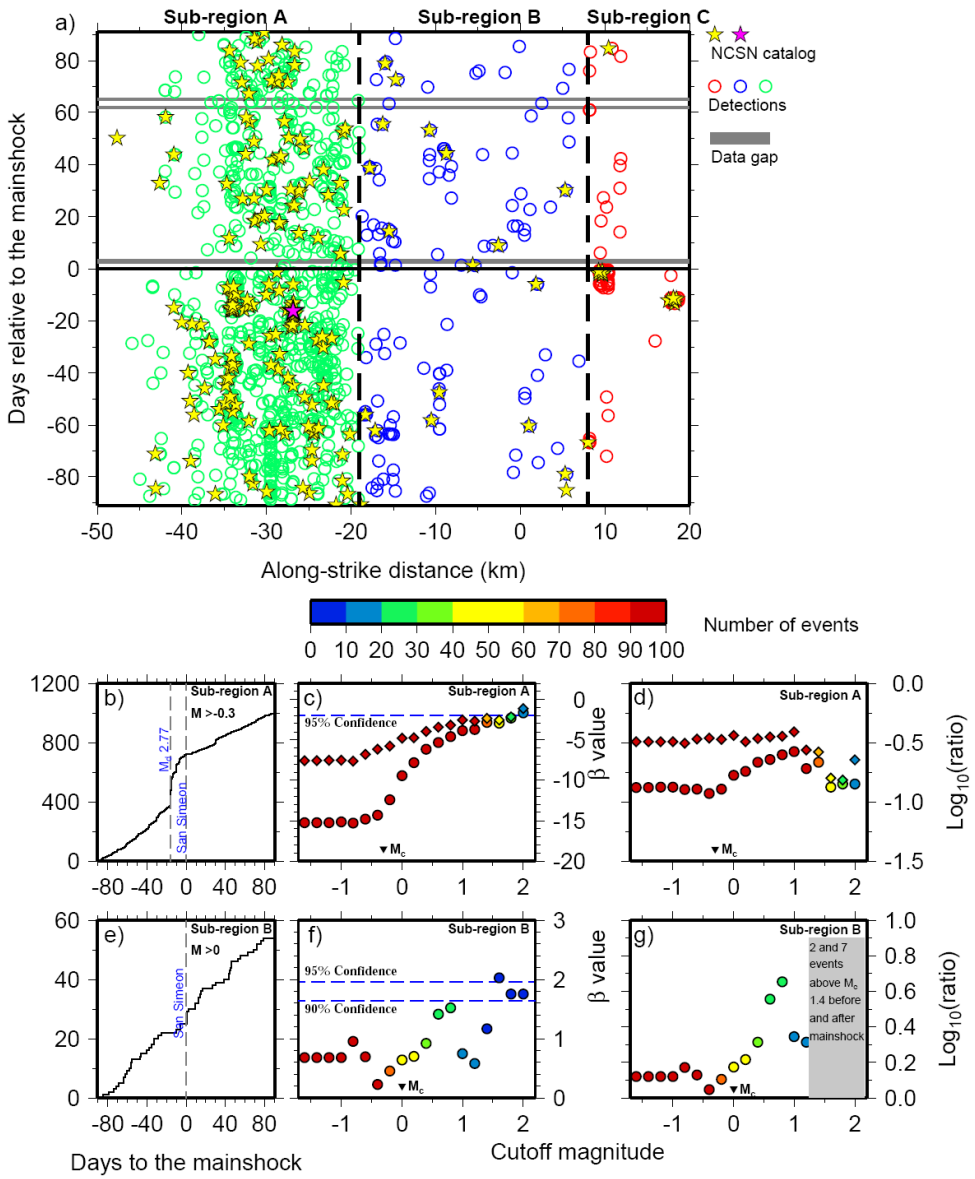

Figure 3.9 (a) Similar plot as Figure 3.6b with detected events from 90 days before to 90 days after the San Simeon mainshock. (b)-(g) Similar plot as Figure 3.7 with detected events from 90 days before to 90 days after the mainshock.

3.6.3 Comparisons with the Static Stress Changes

I calculate the static stress changes produced by the San Simeon earthquake based on an updated finite fault model [*Ji et al.*, 2004]. Because the focal mechanisms of more than 95% of the earthquakes around Parkfield are pure right-lateral on the fault within

their uncertainties [*Thurber et al.*, 2006], the effects of variant geometry of 'receiver' faults can be largely neglected [*Toda et al.*, 2012]. Here I calculate the shear, normal and Coulomb stress changes at 7.5 km depth in map view (Figure 3.1) and along the strike in cross-section (Figure 3.4a and 3.6a) with an effective coefficient of friction of 0.4 [*Aron and Hardebeck*, 2009]. The 7.5 km depth is chosen to be close to the average depth of the detected events.

No apparent consistency between the Coulomb stress and seismicity rate changes is found. Instead, static shear stress changes alone explain the behavior of seismicity across the study region. In particular, a clear negative static shear stress (i.e., stress shadow) is found in the creeping section of the SAF (sub-region A). I also observe a significant decrease of seismicity rate across all magnitude bands (Figure 3.7b, 3.7c, 3.9c, and 3.9d) and a stifled aftershock sequence of an M_d 2.77 earthquake (Figure 3.7a), consistent with the stress shadow effect. An abrupt recovery at ~30 days after the mainshock can be seen for the detected events (Figure 3.7a and 3.9b). In comparison, between Middle Mountain and Cholame the static shear stress increased after the San Simeon mainshock, I find a moderate increase of seismic activity for most magnitude bands (Figure 3.7d-f, 3.9e-g).

3.7 Discussion

In this study, I applied the waveform matched filter technique to detect earthquakes around the Parkfield section of the SAF following the nearby San Simeon mainshock. After removing all possible false and duplicated detections, I have detected ~8 times more events than listed in the NCSN catalog. The seismicity rate beneath the creeping section of the SAF showed a statistically significant reduction following the San

Simeon mainshock, which correlates well with the negative shear stress changes. Interestingly, deep tectonic tremors in that sub-region were also stifled for 3-6 weeks and followed by an accelerated recovery from ~30 days after the mainshock, which agrees well with estimated duration of the stress shadow effect [*Shelly and Johnson*, 2011]. However, the recovery of earthquake activity in this study was transient and the seismicity rate remained low near the end of the study period. The seismicity rate increased moderately in sub-region B around the rupture zone of the 2004 Parkfield earthquake (Figure 3.7e and f), where positive static shear stress changes were induced (Figure 3.6a), suggesting that the San Simeon mainshock loaded this section of the SAF. This is also consistent with the triggered creep events near Parkfield on the SAF observed by the USGS creep meters after the San Simeon mainshock [*Aron and Hardebeck*, 2009] and a minor increase of tremor activity in the lower crust [*Shelly and Johnson*, 2011]. In sub-region C, the turnoff of earthquake swarms is inconsistent with positive static stress changes or oscillatory dynamic stresses. According to the focal mechanism catalog from NCSN, the very first event of the earthquake swarms is a normal faulting event, instead of right lateral (beach ball in Figure 3.6b). The computed static shear and Coulomb stress increase for a receiver fault with normal faulting in this sub-region, which still cannot explain the turnoff. However, the swarms completely stopped about half-day prior to the mainshock (Figure 3.7h). Therefore, while the coincidence of the turnoff of the swarms at the time of the San Simeon earthquake suggests a causal connection, the Coulomb stress changes do not explain the turnoff.

The rupture of the Parkfield earthquake ended close to the boundary of positive static shear stress changes [*Murray and Langbein*, 2006]. Hence, it is tempting to

conclude that the negative static shear stress changes from the San Simeon mainshock may have stopped the rupture propagation of the 2004 Parkfield event. However, the negative shear stress change also coincided with the creeping section of the SAF, where the far-field tectonic loading is mostly released by creeps and numerous small earthquakes. Hence, the overlapping between static stress changes and the main rupture zone of the 2004 Parkfield event could be just by coincidence.

Finally I check whether the observed seismicity rate changes were resolvable using the NCSN catalog alone. In sub-region A, I obtain a M_c of 1.5 for the NCSN catalog. β value and seismicity ratio in sub-region A at cutoff magnitude 1.5 are -1.55 and -0.57, respectively. In sub-region B, only 1 and 4 events listed in the NCSN catalog before and after the San Simeon earthquake during the primary study period, respectively (Figure 3.6b). M_c and β value cannot be measured due to the small dataset. Hence, without newly detected events, one might still conclude the aforementioned seismicity rate changes pattern, but statistical significance can no longer be established.

In summary, the seismicity rate changes at Parkfield correlates well with the static shear stress changes induced by the San Simeon earthquake, suggesting that static stress change is an important, if not the only, agent for near-field triggering in this region. The results are consistent with a recent finding of a stress shadow in the aftershock zone of the 1992 M_w 6.3 Joshua Tree earthquake cast by the 1992 M_w 7.3 Landers earthquake [*Toda et al.*, 2012], indicating that stress shadows do exist and may play an important role in changing seismic activities in the near field. Transient dynamic triggering may have occurred in the study region, but was not detected by the technique because of the

close distance between Parkfield and the San Simeon epicenter, and clipping of the stations in the first ~100 s immediately after the San Simeon mainshock.

In the stress shadow region, I found that β-values increase with increasing cutoff magnitude (Figure 3.7b). Hence, one may argue that the seismicity rate drop is simply due to the reduction in detection ability after the mainshock, especially for small magnitude events, because large San Simeon aftershocks could contaminate the continuous data and increase the noise level at the stations. However, it appears that the San Simeon mainshock and its aftershocks only cause significant increases of the noise levels at the stations for ~3 days. The median noise level decayed back to pre-shock level in 3 to 5 days after the mainshock. Moreover, the relationship between the mean CC and magnitude of detected events before and after the mainshock shows essentially the same pattern (Figure 3.5b and c), suggesting a consistent detection through the study period. Finally, if detection ability indeed lowered after the mainshock, I should observe the stifled seismicity rate and β-values increase with cutoff magnitude in sub-region B as well, which is not the case (Figure 3.7e). Excluding the possibility of changing detecting ability, β-value declining significance with cutoff magnitude could be mainly due to the smaller dataset with increasing cutoff magnitude.

The fact that static shear stress, instead of Coulomb stress, changes were consistent with the seismicity rate changes, as well as the behavior of tectonic tremors [*Shelly and Johnson*, 2011], argues for a very low friction along the Parkfield section of the SAF through the entire crust. This was also suggested by the laboratory measurement from SAFOD drilling samples [*Lockner et al.*, 2011] and previous study on response of the Parkfield section of the SAF to large earthquake [*Toda and Stein*, 2002]. Such fault

weakness may attribute to the fact that the mature SAF developed a thick, impermeable gauge zone that reduces the effective coefficient of friction [*Zoback et al.*, 1987; *Felzer and Brodsky*, 2005].

CHAPTER 4

SEISMICITY RATE CHANGES IN THE SALTON SEA GEOTHERMAL FIELD AND THE SAN JACINTO FAULT ZONE AFTER THE 2010 M_W 7.2 EL MAYOR-CUCAPAH EARTHQUAKE

4.1 Introduction

The 2010 M_w 7.2 El Mayor-Cucapah earthquake is the largest event occurred in the vicinity of southern California since the 1992 M_w 7.3 Landers and 1999 M_w 7.1 Hector Mine earthquakes (Figure 4.1). The El Mayor-Cucapah event is reported to start with a M~6 normal faulting event and was then followed by a combination of normal and right-lateral strike-slip events ~15 s later [*Hauksson et al.*, 2011]. The entire aftershock zone spans ~120 km between the southern end of the Elsinore fault and the northern tip of the Gulf of California. Due to its enormous size, this event caused ~3-40 cm/s peak ground velocities in southern California [*Graves et al.*, 2011], which corresponds to ~0.3-4.0 MPa dynamic stress changes using a nominal shear wave velocity of 3.5 km/s and a shear rigidity of 35 GPa [*Hill and Prejean*, 2007]. *Hauksson et al*. [2011] found that the south portions of the Elsinore fault and the San Jacinto fault experienced a clear increase in seismicity following the El Mayor-Cucapah mainshock, which may have been triggered by either dynamic or static stress changes.

Due to its proximity to the dense seismic networks in southern California, this event provides an excellent case to test whether static or dynamic stress changes are the primary agent for triggering earthquakes in the near field. In this study, I focus mainly on the following two regions: the Salton Sea Geothermal Field (SSGF) and the San Jacinto Fault Zone (SJFZ). I choose these two regions mainly because of their intensive

background seismicity, which allow me to easily identify seismicity rate decrease (i.e., stress shadows) [*Felzer and Brodsky*, 2005]. In addition, both regions are monitored by borehole short-period sensors [*Barbour and Agnew*, 2012], which provide unique, high quality continuous recordings around the origin time of the El Mayor-Cucapah mainshock.

Many previous studies have shown that seismic catalogs are incomplete immediately following a major event [*Peng et al.*, 2006; *Enescu et al.*, 2007; *Kilb et al.*, 2007; *Peng et al.*, 2007]. To avoid issues caused by catalog incompleteness, I apply a waveform-based matched filter technique [*Shelly et al.*, 2007; *Peng and Zhao*, 2009; *Yang et al.*, 2009] to systematically detect earthquakes in both regions. The study spans from 1 March 2010 to 1 August 2010, which is ~1 month before to ~4 months after the mainshock. My goal is to detect the genuine seismicity rate changes in the SSGF and the SJFZ using the new catalog.

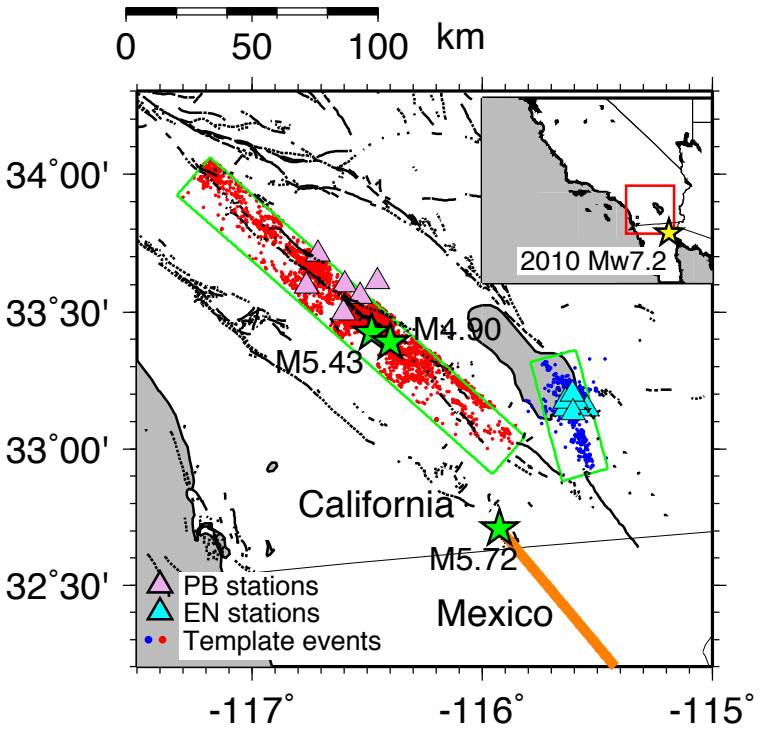

Figure 4.1 The study region in southern California. The black lines denote active faults. The green boxes denote the two study regions: SSGF and SJFZ. The red and blue dots denote 2,916 and 11,911 templates in the SSGF and the SJFZ, respectively. The red and blue triangles denote 6 borehole stations from the PBO and EN networks, respectively. The green stars denote the 13 June 2010 M_w 4.90, the 15 June 2010 M_w 5.72, and the 7 July 2010 M_w 5.43 earthquake. The orange thick line marks the approximate rupture plane of the 2010 El Mayor-Cucapah mainshock. The inset map shows southern California. The red box denotes the study region. The yellow star denotes the epicenter of the El Mayor-Cucapah mainshock.

4.2 Data Preparation and Analysis Procedure

The continuous seismic data are recorded by 6 borehole stations from the Plate Boundary Observatory (PBO) network in the SJFZ and the Calenergy subnetwork (EN) in the SSGF, respectively (Figure 4.1). I segment the continuous data into 24-hour segments relative to the origin time of the mainshock. I compute the median absolute deviation (MAD) of the 24-hour continuous data for all channels as a measure of the noise level. If a channel has frequent occurrences of abnormal fluctuating signals during one day, it will have a very large MAD and thus is excluded from the data set. For some days, stations B081 and B086 from the PBO network are excluded because they recorded frequent occurrence of large impulse-like signals during these days, which contaminates the continuous waveforms. Station OBS from the EN network is also excluded because it stopped recording for the most study period after the mainshock.

To obtain the optimal SNR, I band-pass filter both continuous and template waveforms by 10-40 Hz. Moreover, the high frequency range helps to suppress lower frequency signals associated with the distant El Mayor-Cucapah mainshock and its large aftershocks. Since such high frequency signals from small earthquakes are usually attenuated in the near surface, I only use borehole stations in this study. From the 10-40 Hz band-pass filtered waveforms from the borehole stations in the SSGF and the SJFZ, I

find many high-frequency energy spikes immediately after the El Mayor-Cucapah mainshock. Many of these events are not listed in the Southern California Seismic Network (SCSN) catalog. Since high-frequency energy of aftershocks from the immediate vicinity of the mainshock is mostly attenuated, the most likely source is locally triggered earthquakes.

I use the waveforms of 2,916 and 11,911 earthquakes listed in a waveform relocated catalog (hereafter, relocated catalog) [*Hauksson et al.*, 2012] from January 2008 to December 2010 as templates in the SSGF and the SJFZ, respectively (Figure 4.1). The template waveforms are 1s before to 4s after the *P*-wave arrival time for vertical component and 1s before to 4s after the *S*-wave arrival time for horizontal components. In the SSGF, I manually pick the *P*- and *S*-wave arrival times of 2,916 templates. In the SJFZ, because of the large number of template events, I predict the *P*- and *S*-wave arrival times at the borehole stations based on a 1-D velocity model in that region (Debi Kilb, personal communication, 2012). Comparing the predicted arrival times with the ones picked by the SCSN, I find that more than 99% of the time differences are less than 0.7s, which is much less than the 5s window used for waveform matching.

Following *Meng et al.* [2013], I allow one data point shift while stacking the resulting cross-correlation traces for all station-components. This helps to reduce potential time shift due to rounding and achieve self-detection with mean correlation coefficient (CC) of 1. In addition, I compute the magnitude of the detected event based on the median value of the peak amplitude ratio between the detected and template events among all channels [*Peng and Zhao*, 2009].

4.3 False Detections

The detection threshold is set as the sum of the median value and 15 times the MAD of the mean CC trace [*Meng et al.*, 2013]. By using this relative high threshold, most false detections of regional earthquakes can be removed. However, some earthquakes that occurred on the neighboring Elsinore fault are still falsely detected by one template event in the SJFZ. This template event has a magnitude of 1.53 and occurs on 5 April 2010. Except the self-detection (i.e., CC=1.0), all detected events by this template have very low CC values. It appears that a few channels of the template correlate well with a segment of an event with longer duration. According to the SCSN catalog, this event with longer duration occurred on the Elsinore Fault. I include ~500 templates along the Elsinore fault to remove such false detections, because those templates would match better with events on the Elsinore Fault than templates in the SJFZ. Indeed, after including the ~500 templates along the Elsinore Fault, all falsely detected events are removed. Similarly, I find that some aftershocks near the northern tip of the El Mayor-Cucapah mainshock rupture are falsely detected by templates in the SJFZ and the SSGF. Therefore, I include ~700 templates near the northern tip of the mainshock rupture. In this way, almost all the false detections can be removed.

4.4 Seismicity Rate Changes

In summary, I detect 8,986 events in the SSGF (Figure 4.2a) and 43,262 events in the SJFZ (Figure 4.3a). During the same space-time window, ~400 and ~3,500 events are listed in the SCSN catalog in the SSGF and the SJFZ, respectively. I also compute the magnitude of completeness (M_c) using ZMAP [*Wiemer*, 2001]. As shown in Figure 4.4, the M_c for both regions is significantly reduced from ~1.2 to ~–0.5. I also compute a fluctuating M_c with time [*Toda et al.*, 2012; *Kato et al.*, 2013] using a data window of

200 events with 50% overlap. Not surprisingly, the M_c increases temporarily right after the El Mayor-Cucapah mainshock and moderate size local earthquakes due to the masking effect [*Peng et al.*, 2006; *Kilb et al.*, 2007; *Peng et al.*, 2007], but it remains stable during the other time periods.

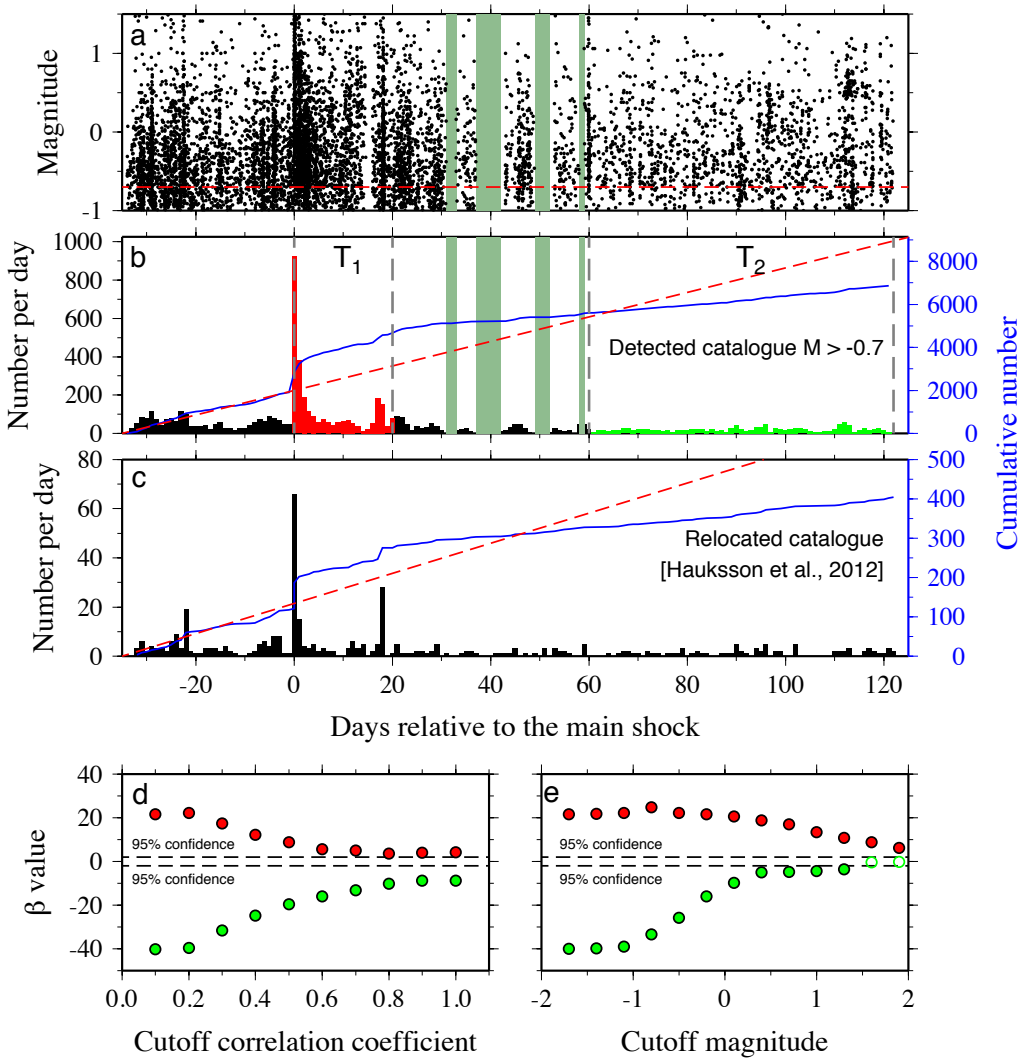

Figure 4.2 The seismicity rate changes in the SSGF. (a) Magnitude of all detected events in the SSGF versus days since the El Mayor-Cucapah mainshock. The red dashed line denotes the M_c of –0.7 in the SSGF. The green shaded areas denote gaps in the continuous data. (b) Number of detected events per day (vertical bar) versus times around the mainshock. The blue line denotes the cumulative number of detected events. The red dashed line denotes the average pre-mainshock rate. The grey dashed lines define the short- and longer-term time window, T_1 (red) and T_2 (green) used for calculating the statistical β-value. (c) Same with panel b using events listed in the relocated catalog. (d-e)

β-values in T_1 (red) and T_2 (green) versus cutoff CC and magnitude, respectively. Solid dots and open circles denote β-values calculated from more and less than 50 events, respectively. The horizontal dashed lines mark the β-value of ± 2.

In the SSGF, the detected catalog shows a significant increase of seismic activity immediately after the El Mayor-Cucapah mainshock (Figure 4.2b). The intense seismicity lasted ~3 days and then quickly decayed back to pre-mainshock level. Approximately 20 days after the mainshock, the seismicity rate dropped well below the pre-mainshock level. The apparent quiescence in the SSGF remained up to 120 days after the mainshock (Figure 4.2b). To further evaluate the evolution of seismicity rate changes in the SSGF, I define the short-term and the longer-term time windows: between 0-20 (i.e., T_1) and 60-121 (i.e., T_2) days after the mainshock, respectively. I define these time windows partially to avoid data gaps in the continuous recordings (Figure 4.2b). I then calculate β-values [*Matthews and Reasenberg*, 1988; *Kilb et al.*, 2002; *Aron and Hardebeck*, 2009] in T_1 and T_2 as a measure of the significance of the seismicity rate changes in the short- and longer-term, respectively. β-value compares the deviation of seismicity during a time period from the expected seismicity in that time period assuming a constant seismicity rate and normalized by the standard deviation of the expected seismicity [*Matthews and Reasenberg*, 1988]. If β-value is larger than 2 or smaller than –2, it indicates a statistically significant seismicity rate increase or decrease, respectively [*Hill and Prejean*, 2007]. The resulting β-values in T_1 and T_2 are 10 and –39, respectively, suggesting that the short-term increase and longer-term decrease of the seismicity rate in the SSGF are statistically significant.

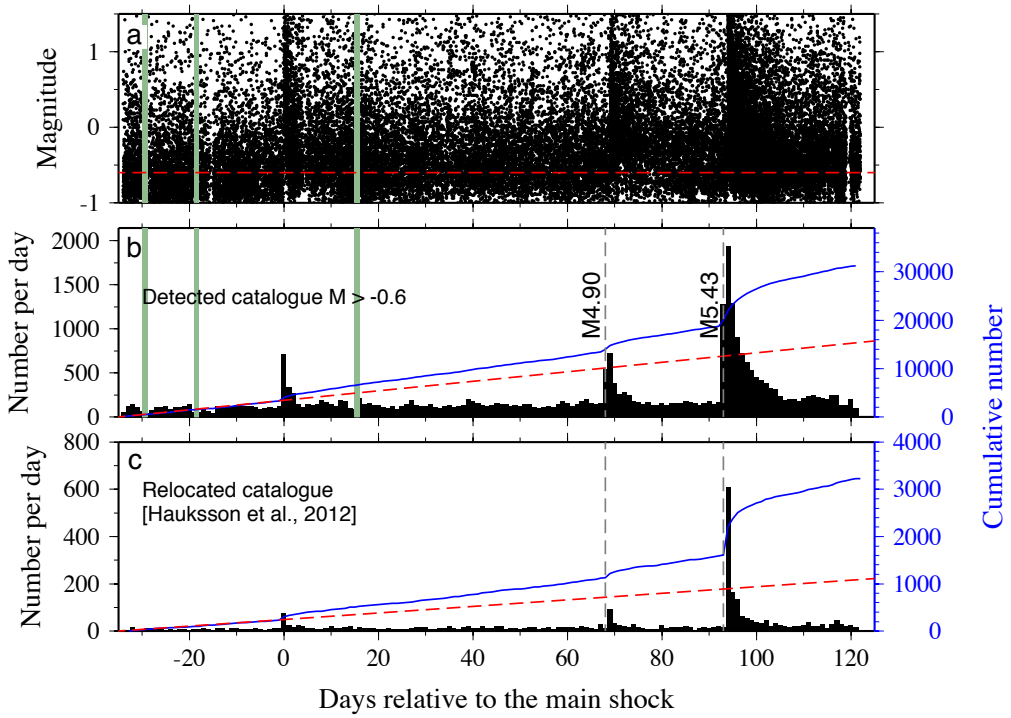

Figure 4.3 The seismicity rate changes in the SJFZ. All the denotations are the same as in Figure 6. (a) Magnitude of all detected events in the SJFZ versus days since the mainshock. (b) Number of detected events per day (vertical bar) versus times around the mainshock. The grey dashed lines denote the origin times of the 13 June 2010 M_w 4.90 and 7 July 2010 M_w 5.43 earthquake. (c) Same with panel b using events listed in the relocated catalog.

With possible false detections in mind, I test the robustness of the seismicity rate changes in the SSGF with varying detection thresholds. I calculate β-values in T_1 and T_2 from the sub-catalogs after applying a cutoff CC from 0.1 to 1.0. When the cutoff CC is set to 1.0, the detected and relocated catalogs are the same. The significance of the short-term increase and long-term decrease of the seismicity rate are still valid for all cutoff CC (Figure 4.2d). Similarly, I recognize that β-values may strongly depend on the M_c, which fluctuates with time (Figure 4.4c). I explore the dependence of β-value on the M_c and further confirm that the aforementioned rate changes in the SSGF are significant for most of the M_c values (Figure 4.2e). Finally, I compute β-values and seismicity ratio in a

sliding time window. The sliding time window is the same length with the pre-mainshock period (i.e., 33 days) and moves forward by 10 days. The obtained values are assigned to the median point of the sliding time window. The results also echo an immediate seismicity rate increase followed by a significant decrease.

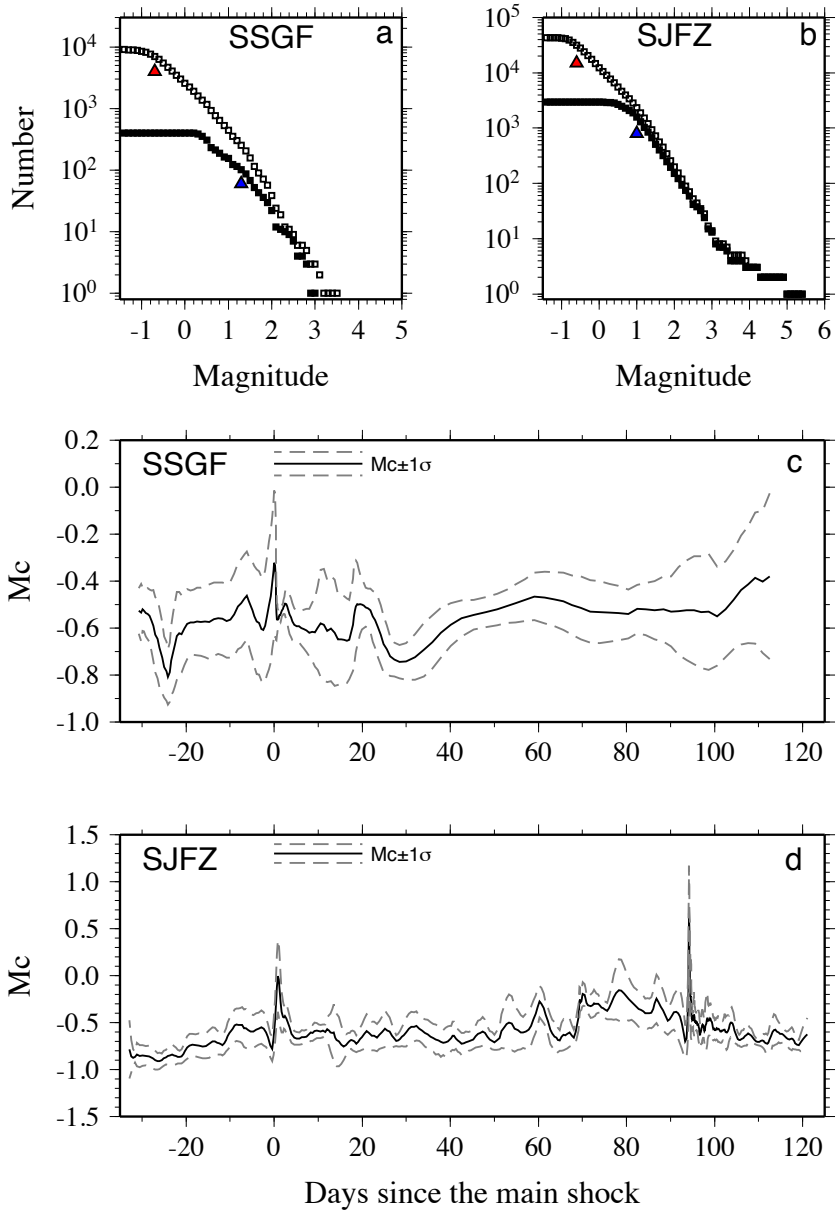

Figure 4.4 (a-b) The frequency-magnitude relationship in the SSGF and the SJFZ, respectively. The open squares denote the newly detected events. The black squares denote events listed in the relocated catalog. The triangles denote the M_c. (c-d) The M_c versus days since the mainshock in the SSGF and the SJFZ, respectively.

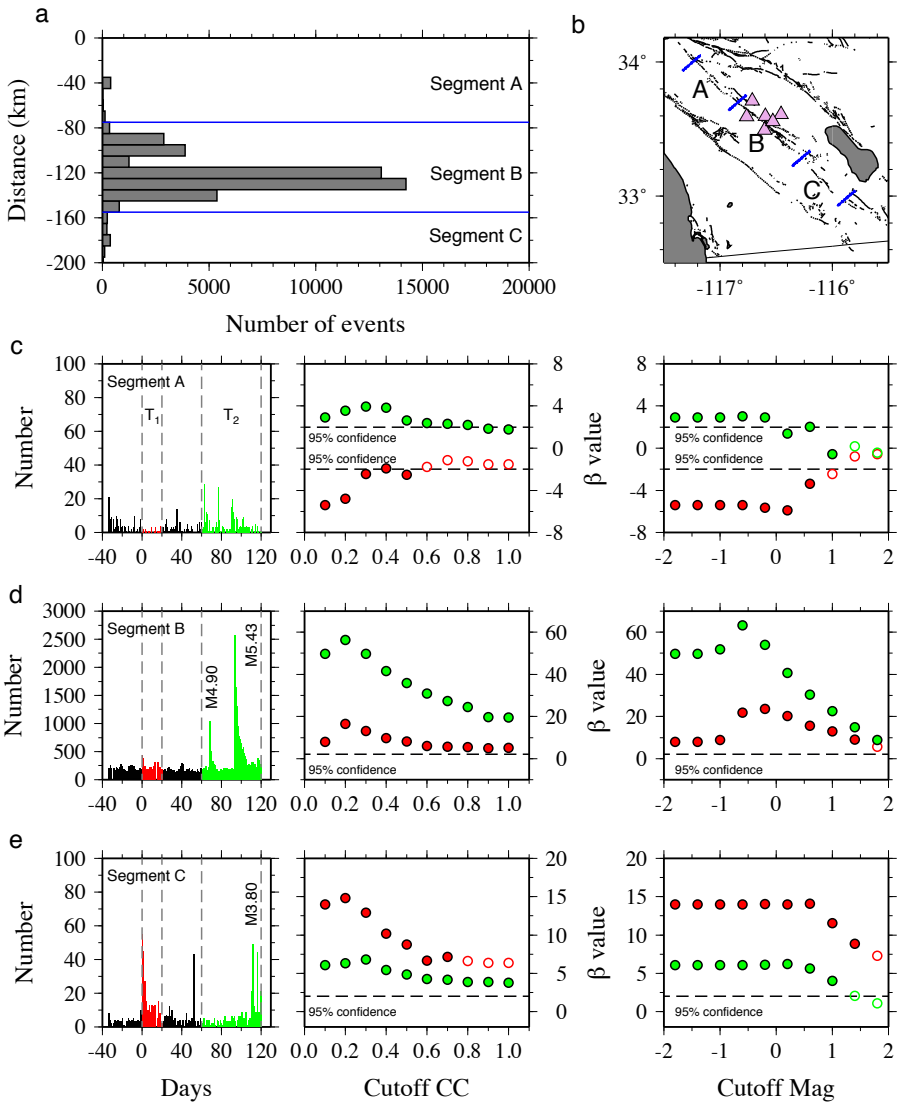

Figure 4.5 The seismicity rate changes in three segments in the SJFZ. (a) Number of detected events versus the along-strike distance. The blue lines mark the approximate boundary of the three segments. (b) A map view of three segments in the SJFZ. (c-e) The seismicity rate changes in three segments. Left panels denote number of detected events per day versus days since the mainshock. Middle panels denote β-values in T_1 (red) and T_2 (green) versus cutoff CC. Right panels denote β-values in T_1 (red) and T_2 (green) versus cutoff magnitude. Solid dots and open circles denote β-values calculated from more and less than 50 events, respectively.

In the SJFZ, the seismic rate shows a clear increase following the El Mayor-Cucapah mainshock for 2 to 3 days (Figure 4.3b). The seismicity rate remained slightly

higher than the pre-mainshock level for ~70 days. On 13 June 2010 (69 days after the mainshock), an M_w 4.90 earthquake occurred in the SJFZ (green star in Figure 4.1). This event and its own aftershock sequence caused a clear increase of seismicity rate for a few days (Figure 4.3b). Again on 7 July 2010 (94 days after the mainshock), an M_w 5.43 earthquake occurred in the SJFZ (green star in Figure 4.1) and produced the largest jump of seismicity during the study period (Figure 4.3b). The seismicity rate then gradually decayed approximately following Omori's law [*Utsu et al.*, 1995]. To be consistent with the SSGF, I define the short- and longer-term time windows to be 0–20 (i.e., T_1) and 61–120 (i.e., T_2) days after the mainshock, respectively. The β-values in T_1 and T_2 are 19 and 64, respectively, suggesting significant seismicity rate increase in both time periods.

Since the study region extended ~170 km along the strike of the SJFZ, the seismicity rate may vary substantially along the fault. I then divide the SJFZ into three segments based on their seismicity levels and investigate the seismicity rate changes in T_1 and T_2 of the three segments separately (Figure 4.5). In Segment A (the northern portion), the seismicity rate decreased briefly following the mainshock and then increased to a higher rate than the pre-mainshock level (left panel in Figure 4.5c). The significance of the seismicity rate changes is only valid for certain cutoff CC and magnitude (middle and right panels in Figure 4.5c). Since the majority of detected events in the SJFZ occurred in Segment B (the central portion), the evolution of the seismicity rate in Segment B is almost identical to that of the entire SJFZ described earlier (left panel in Figure 4.5d). The increases of the seismicity rate in the short- and longer-term are both significant with all cutoff CC and magnitude (middle and right panels in Figure 4.5d). In Segment C (the southern portion), the seismicity rate increases immediately following the mainshock (left

panel in Figure 4.5e), which was also reported by *Hauksson et al.* [2011]. This short-term increase is statistically significant for all cutoff CC and magnitude (middle panel in Figure 4.5e). On 25 July 2010 (112 days after the mainshock), an M_w 3.80 earthquake occurred, which is the largest event in Segment C during the study period. This event and its aftershocks caused another abrupt jump of seismicity and the significant seismicity rate increase in the longer-term for all cutoff CC and magnitude (right panel in Figure 4.5e). Similar with the SSGF, I also compute β-values and seismicity ratio in the sliding time window to further illustrate the aforementioned evolution of seismicity rate changes in all three segments.

4.5 Coulomb Stress Changes

To compute the Coulomb stress changes caused by the El Mayor-Cucapah mainshock, I use a complex finite-fault model inverted from InSAR observations by Dr. Yuri Fialko (http://sioviz.ucsd.edu/~fialko/baja.html), which has two planar surfaces that are divided into 369 patches, each with its own slip, strike, and dip. For the receiver faults, I investigate the distributions of strike, dip and rake angles for earthquakes that occurred in the SSGF and the SJFZ since 1981 based on the preferential focal mechanism solutions [*Yang et al.*, 2012]. I find that the vertical, right-lateral strike-slip fault (strike=150 deg clockwise from North) is the dominant fault geometry in both regions and hence is used as the receiver fault geometry.

I use the Coulomb 3.3 software package to calculate the static stress changes in southern California at a depth of 5 km, which is the average depth for earthquakes in the study region. As was done before [e.g., *Toda et al.*, 2012], the effective coefficient of friction is set to 0.4. Figure 4.6 shows the computed static Coulomb, shear, and normal

stress changes. In the SSGF, the mainshock induced a Coulomb stress decrease of ~10 kPa. On the other hand, the majority of the SJFZ experienced the Coulomb stress increase of 5-10 kPa. I also calculate the Coulomb stress changes with different depths and effective coefficient of friction, and the patterns remain similar.

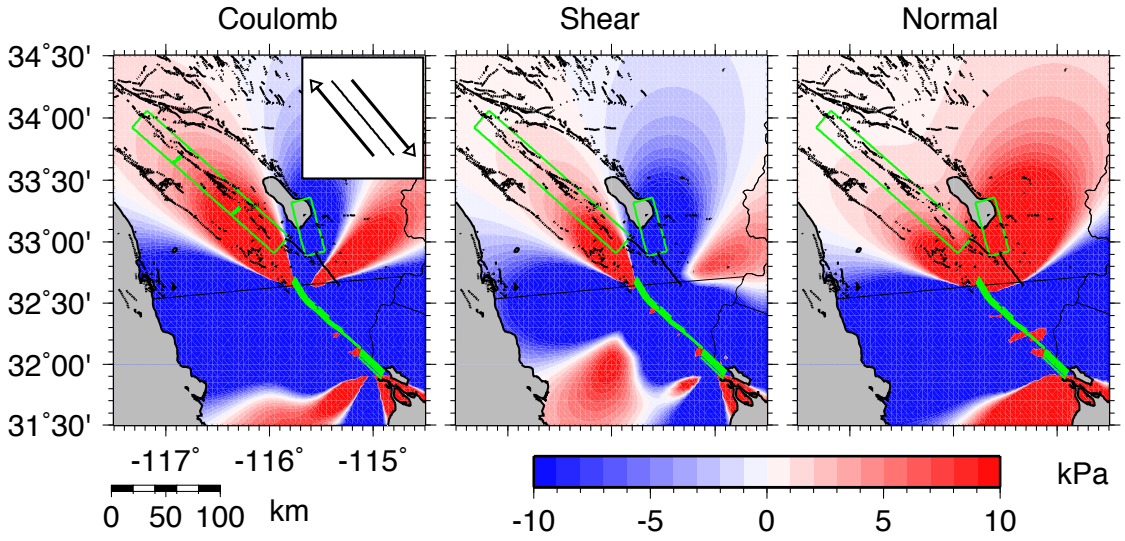

Figure 4.6 The static Coulomb (a), shear (b) and normal (c) stress changes in southern California following the El Mayor-Cucapah mainshock. The green boxes denote the study regions in the SSGF and the SJFZ. The green thick lines denote the finite-fault model of the mainshock. The inset denotes the receiver fault geometry.

4.6 Comparisons Between Seismicity Rate and Stress Changes

In the SSGF, the immediate increase of seismicity following the El Mayor-Cucapah mainshock (Figure 4.2b) is opposite to the prediction of the 'stress shadow' (Figure 4.6a). On the other hand, the widespread dynamic stress increase [*Graves et al.*, 2011] can explain the abrupt jump of seismicity. The peak ground velocity at station RXH in the SSGF is 4-7 cm/s (COSMOS data center, http://strongmotioncenter.org/), which corresponds to significant dynamic stress changes of 0.4-0.7 MPa. Moreover, two earthquakes in the SSGF are detected during the mainshock's surface wave, which are

most consistent with dynamic triggering (Figure 4.7). The template events that detected the two earthquakes are both located near station HAT at shallow depths of 4.1 and 2.4 km. The CC values of the two detected events are 0.20 and 0.28, which are relatively low and may due to contamination from the mainshock coda wave. Alternatively, this reflects a minor difference in hypocenters between the detected events and templates. *Hough and Kanamori* [2002] found that an earthquake was instantaneously triggered by the surface wave of the 1999 M_w 7.1 Hector Mine earthquake within a few km of station SSW in the SSGF. By comparing the peak amplitude at station SSW with that of a close earthquake listed in the SCSN catalog, they assigned magnitude 4.7 to that triggered event. I follow their method and compare the peak amplitude at station RXH between the two triggered events and ~150 nearby events listed in the relocated catalog. Assuming a linear relationship between magnitude and logarithmic amplitude, I estimate magnitude ~3 for both triggered events. While examining the band-pass filtered waveforms, it appears that a third event may also be contained in the surface wave of the mainshock (Figure 4.7), but is not detected. The third event produced even larger amplitude at station ELM and RXH than the first two events did. However, it has indistinguishable signals at all other stations, so it is not detected by the technique. The hypocenter of the third event therefore is likely very close to stations ELM and RXH and extremely shallow.

The longer-term (i.e., T_2) seismicity rate in the SSGF is significantly lower than the pre-mainshock level (Figure 4.2b), which is consistent with the static Coulomb and shear stress decrease (i.e., stress shadow) in this region (Figure 4.6). Since dynamic stress changes only promote failure, any shadow effect is typically attributed to static triggering. The late emergence of the 'stress shadow' effect suggests that static triggering may

replace dynamic triggering as the dominant triggering mechanism after a certain time point. Due to the gaps in the continuous recordings, it is difficult to find the exact time point between 20 and 60 days after the mainshock (Figure 4.2b).

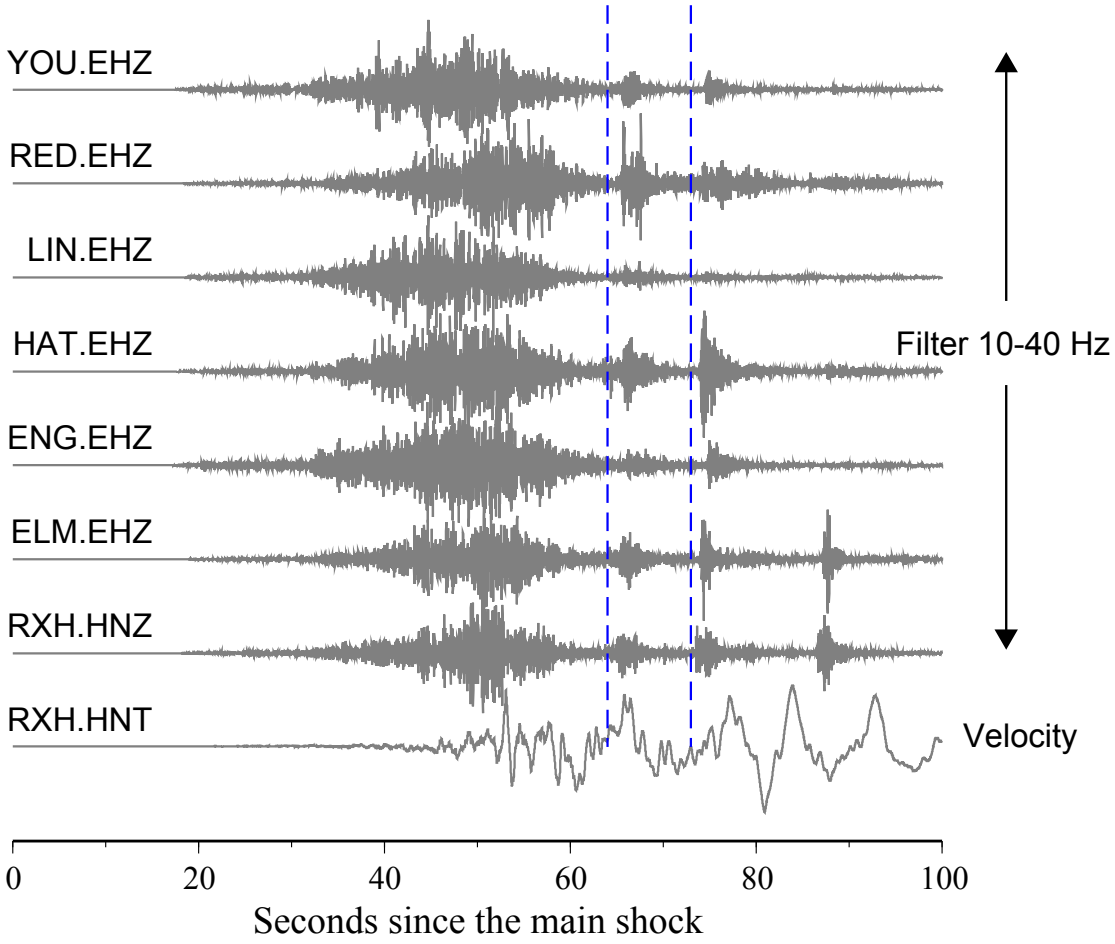

Figure 4.7 10-40 Hz band-pass filtered seismograms showing evidence of dynamic triggered events in the SSGF during the El Mayor-Cucapah mainshock. The band-pass filtered waveforms are from the vertical channel at 6 borehole stations and 1 surface station RXH in the SSGF. The bottom trace denotes the transverse velocity integrated once from the acceleration recording at station RXH. The blue dashed lines denote the origin times of two detected events.

In the SJFZ, the seismicity rate in Segment A decreased in the short-term after the El Mayor-Cucapah mainshock (Figure 4.5c), which is in contrast to both dynamic stresses and the 2-3 kPa Coulomb stress increase (Figure 4.6). However, two M>4

earthquakes occurred in Segment A shortly before the study period, which are the largest ones since 1985 (Figure 4.8a). Therefore, it is possible that the short-term decrease I observed here simply reflects the Omori-decay of the aftershock sequence of the two M>4 events. The mainshock did not disturb the aftershock sequence, likely due to a relatively large (i.e., ~230 km) distance. Alternatively, the region may not be responsive to distant triggering because of a recent failure sequence. There might be a minor increase of the seismicity rate in the longer-term after 60 days, although the increase is only significant for smaller cutoff CC and magnitude (Figure 4.5c).

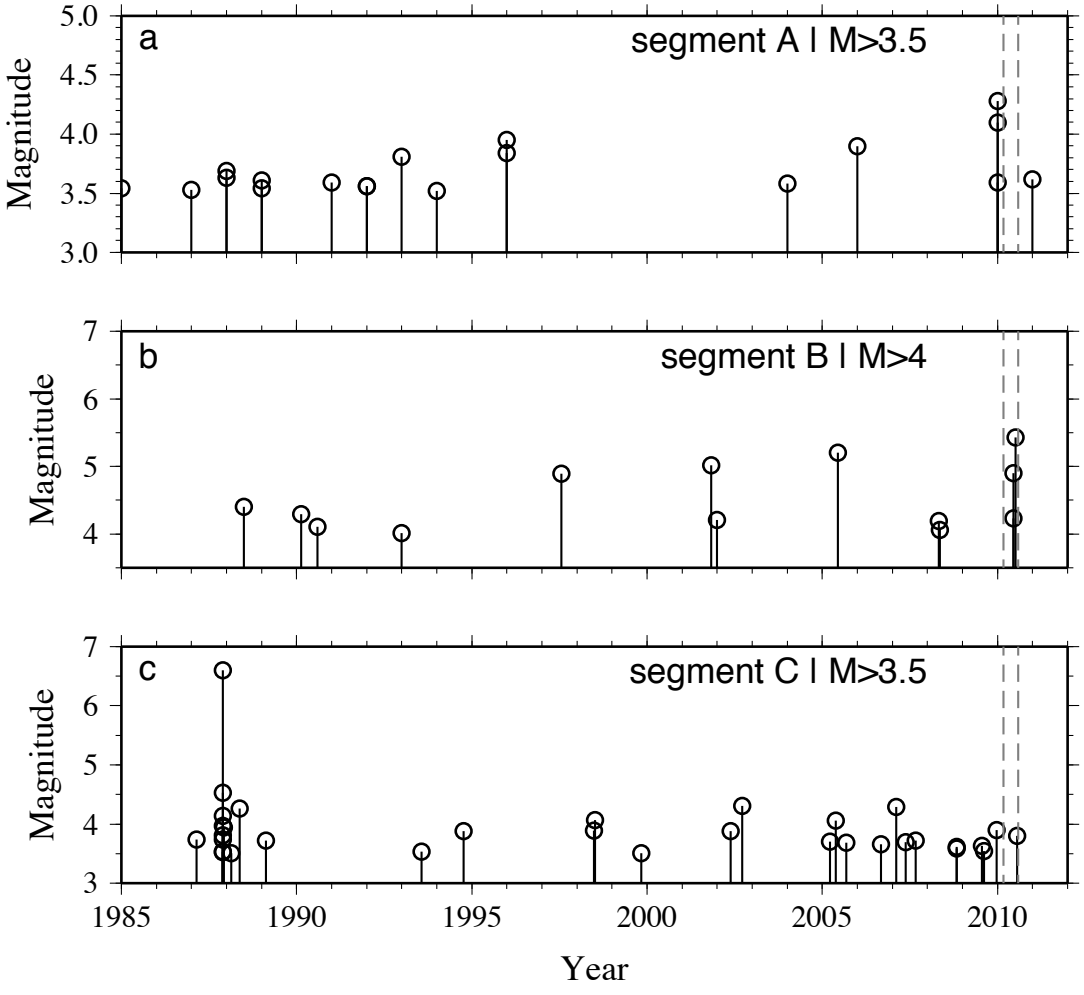

Figure 4.8 (a-c) Earthquakes larger than M3.5, M4 and M3.5 in Segment A, B and C of the SJFZ, respectively. The grey dashed lines denote the study period.

In comparison, in Segments B and C the significant seismicity rate increase is evident in both short- and longer-term regardless of cutoff CCs and magnitudes (Figure 4.5d and e). The short-term rate increases are consistent with both dynamic and static stress increase, which requires further scrutinization. The longer-term increase of seismicity in Segment B and C are primarily contributed by several moderate-size earthquakes and their aftershock sequences at least 60 days following the mainshock (Figure 4.5d and e), hence can be best explained by permanent static Coulomb stress increase (Figure 4.6).

4.7 Discussion

Besides the two instantaneously triggered earthquakes in the SSGF (Figure 8), I also observe a high seismicity rate up to ~10 days after the El Mayor-Cucapah mainshock (Figure 4.2b). Such 'delayed dynamic triggering' is well documented but remains enigmatic. *Brodsky* [2006] suggested that the elevated seismicity rate may be aftershocks of instantaneously triggered events and decay following Omori's law. While other studies proposed secondary triggering mechanisms, such as fault weakening [*Parsons*, 2005], pore-fluid redistribution [*Brodsky and Prejean*, 2005] and triggered creep [*Shelly and Johnson*, 2011]. The decay of the seismicity in the SSGF in T_1 generally follows Omori's law (Figure 4.9a). I obtain a *p*-value of 0.65 by a least-squares fitting. The *p*-value is 0.9 if I exclude the first day after the mainshock. The Omori-like decay suggests that most seismicity in T_1 could be aftershocks of the two M~3 triggered events. Finally, I decluster the detected catalog in the SSGF using the stochastic method [*Zhuang et al.*, 2002; 2004; *Zhuang*, 2006] based on the epidemic-type aftershock

sequence (ETAS) model [*Ogata*, 1988]. The cumulative background seismicity is computed as follow [*Zhuang et al.*, 2005]:

$$S(t) = \sum_{t_i<t} \varphi_i \tag{4.1}$$

where φ_i is the background probability and i runs over the events in the SSGF. Although many earthquakes in T_1 have been removed as aftershocks after declustering, I still observe clear seismicity rate increase in the first ~10 days after the mainshock (Figure 4.10a), which suggests that a small fraction of earthquakes may be triggered by one or more secondary triggering mechanisms.

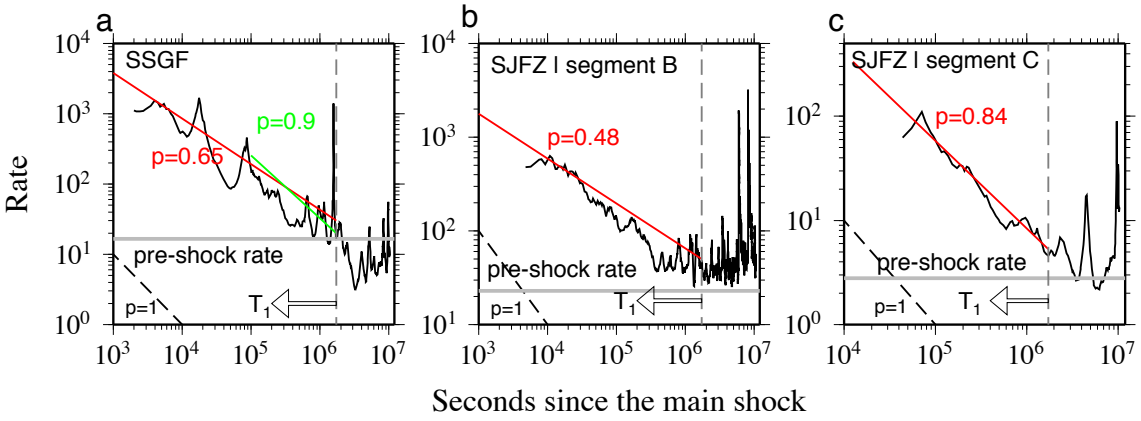

Figure 4.9 Seismicity rate changes following the El Mayor-Cucapah mainshock. Only earthquakes with M>0 are used to correct for the transient increase of M_c immediately after the mainshock. (a) The seismicity rate (events per day) from the detected catalog (black line) in the SSGF versus the time since the mainshock. The grey line denotes the average pre-mainshock rate. The red line denotes the least-squares fitting of the Omori's law from the mainshock to 20 days afterwards. The green line denotes the least-squares fitting of the Omori's law from 1 to 20 days after the mainshock. (b-c) The seismicity rate following the mainshock in Segment B and C of the SJFZ, respectively. The red line denotes the least-squares fitting of the Omori's law up to 20 days after the mainshock.

To further evaluate the quiescence in T_2 in the SSGF, I compute the smoothed seismicity rate from the relocated catalog [*Hauksson et al.*, 2012] since 2007, when the borehole network EN was installed (Figure 4.11a). I first obtain the M_c of 1.3 in the

SSGF using ZMAP [*Wiemer*, 2001]. I then compute the smoothed seismicity rate from January 2007 to January 2011 based on a sliding window technique with a fixed data window of 10 events [*Peng et al.*, 2007]. Figure 4.11a shows that the SSGF has frequent sporadic swarm activities [*Lohman and McGuire*, 2007], which are always followed by a relative quiescence period. Hence, one may argue that the low seismicity rate in T_2 may be just another quiescence period following the swarm or aftershock sequence in T_1, instead of resulting from the Coulomb stress decrease caused by the El Mayor-Cucapah mainshock. However, I do not favor this hypothesis because the quiescence that I observed in T_2 is unique in two aspects. First, the level and the duration of the quiescence in T_2 is the lowest and longest during the 4-year time span (Figure 4.11a). In addition, the largest event during the T_1 time period is only ~M3, which is relatively small as compared with other sequences long before and after the mainshock. Hence, the quiescence is unlikely due to the large event in the T_1 time period alone. Second, for all previous swarms in the SSGF, the seismicity rate afterwards is either slightly higher or roughly equal to that precedes the swarm. The only exception is the quiescence in T_2, whose rate is significantly lower than that before the swarm in T_1 (Figure 4.11a). Therefore, I conclude that the seismicity in T_2 is unique and most likely stifled by a 'stress shadow' from the mainshock.

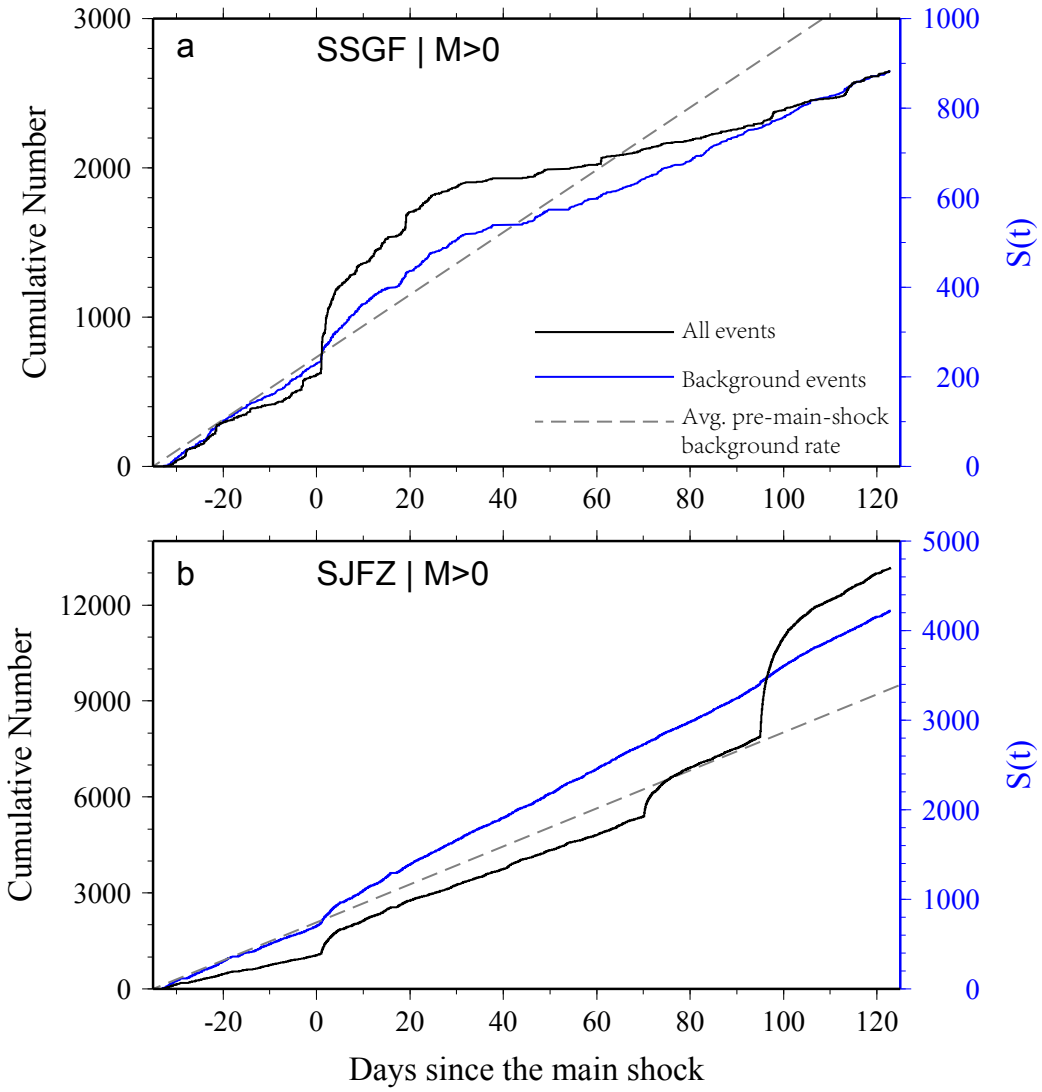

Figure 4.10 The cumulative number of all detected earthquakes (black) and declustered background events in the SSGF (a) and the SJFZ (b). The grey dashed line denotes the mean pre-mainshock background seismicity rate. Only earthquakes with M>0 are used to correct for the transient increase of M_c immediately after the mainshock.

Unlike the SSGF, no instantaneously triggered earthquakes during the surface wave of the mainshock are detected in the SJFZ. The very first earthquake after the mainshock was delayed triggered ~5 minutes afterwards. Therefore, it is more difficult to differentiate static and dynamic triggering in the short-term. Nonetheless, I prefer dynamic triggering in the short-term for two reasons. First, the SJFZ lies in the rupture

direction of the mainshock. The strong motion recordings show that the peak ground velocity in the SJFZ is ~3-4 cm/s (http://strongmotioncenter.org/), which corresponds to ~0.3-0.4 MPa dynamic stress changes and is more than one order of magnitude larger than that of static stress changes (5-10 kPa) at the same location in the SJFZ. Second, the seismicity rates in T_1 decays as predicted by Omori's law in both Segment B and C (Figure 4.9b and c), which are consistent with short-term dynamic triggering [*Brodsky*, 2006]. Similar with the SSGF, after declustering there is still a slight increase of seismicity rate immediately following the mainshock in the SJFZ, which indicates that not all those 'delayed triggered' earthquakes can be regarded as secondary aftershocks.

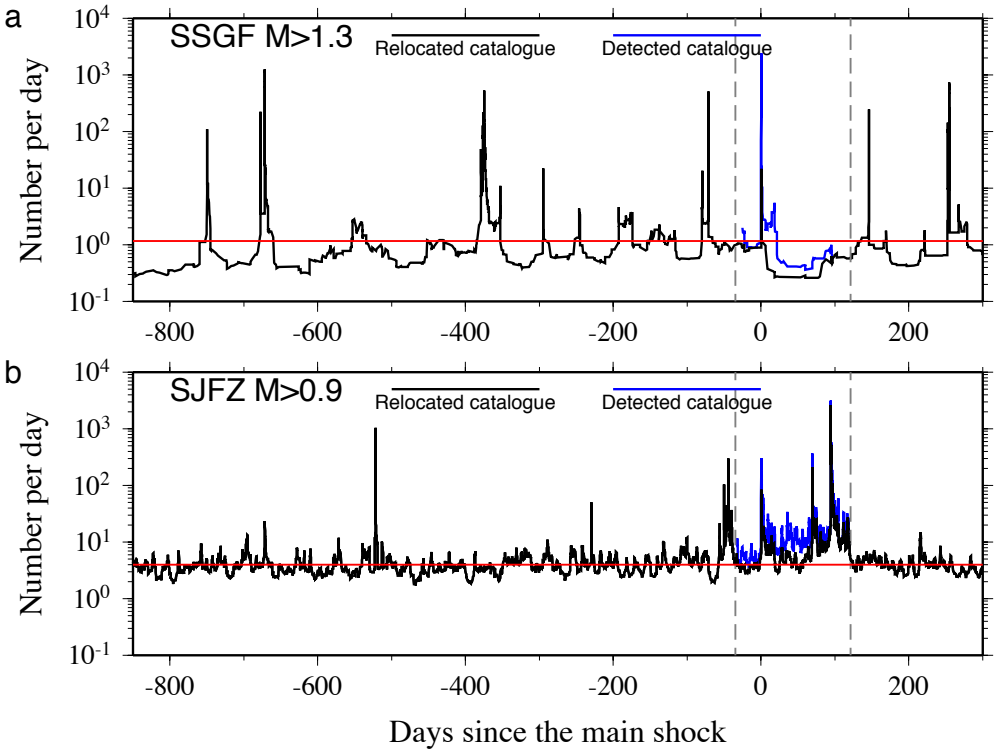

Figure 4.11 The smoothed seismicity rate of events listed in the relocated catalog in the SSGF (a) and the SJFZ (b). I only use events above the M_c in each region to compute the seismicity rate. The grey dashed lines denote the study time period. The red line denotes the approximate background level right before the mainshock. The blue curves denote the smoothed seismicity rate from the detected catalog.

Is the longer-term seismicity rate increase in the SJFZ solely caused by the intensive aftershock sequences of several moderate size earthquakes (Figure 4.5c and d)? Based on the sliding time window analysis, I observe clear seismicity rate increase even prior to the occurrences of the moderate size earthquakes in Segment B and C. Moreover, the declustered background seismicity rate in the SJFZ is clearly elevated by the mainshock throughout the study period (Figure 4.10b). Another natural question to ask is whether the moderate size events are triggered by the El Mayor-Cucapah mainshock. To evaluate the triggering significance of these moderate size earthquakes, I investigate the history of moderate-size earthquakes in Segment B and C (Figure 4.8b and c). In Segment B, the M_w 4.90 and M_w 5.43 events are the fourth and largest event since 1985. They are separated by only 25 days, with another M_w 4.02 event occurring in between. The unprecedented size and short interval of the moderate-size earthquakes suggest that their occurrences are out of the norm and are likely related to the El Mayor-Cucapah mainshock. Both events are pure right-lateral strike slip faulting [*Yang et al.*, 2012], which receives ~10 kPa Coulomb stress increase loading from the mainshock (Figure 4.6a). Since the moderate-size events occurred more than two months after the mainshock, the most likely cause is the Coulomb stress increase that brought the fault segment closer to failure. Similarly, in Segment C the occurrence of the M_w 3.80 earthquake, which is also a pure right-lateral event, is consistent with the Coulomb stress increase. However, since 12 M~3.5 events occurred in Segment C between 2005 and 2010, it is possible that it would have occurred without the El Mayor-Cucapah mainshock (Figure 4.8c). Therefore, the static stress increase likely activated the background seismicity in the SJFZ, as well as promoted the failure of the moderate size earthquakes.

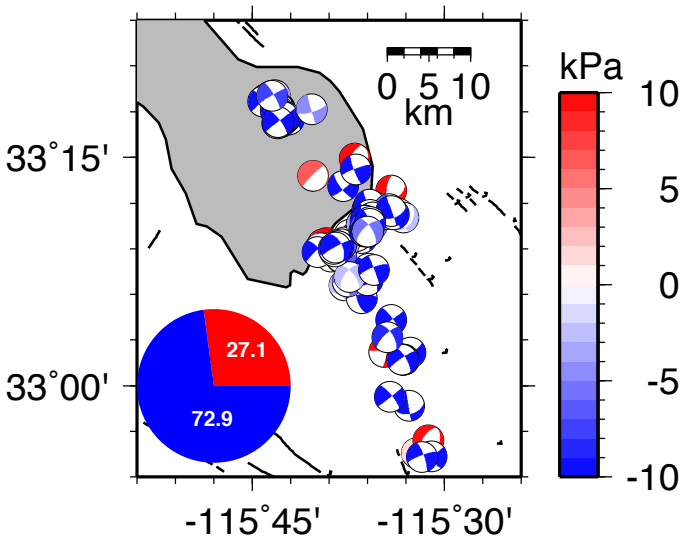

Figure 4.12 Coulomb stress changes imparted on 188 focal mechanisms during five years prior to the mainshock in the SSGF. Blue and red denote Coulomb stress decrease and increase, respectively. The pie chart denotes the percentage distribution of Coulomb stress changes.

4.8 Alternative Models

A delayed shutdown of seismicity rate in the 'stress shadow' has been observed following the 1999 Chi-Chi [*Ma et al.*, 2005], 1983 Coalinga [*Toda and Stein*, 2002] and 1992 Landers [*Marsan and Nalbant*, 2005; *Toda et al.*, 2012] earthquakes. *Toda et al.* [2012] demonstrated that if a fraction of earthquakes in the 'stress shadow' have positive Coulomb stress changes, a seismicity rate jump followed by a delayed shutdown in one-day to three-month can be modeled by a rate/state friction implementation of Coulomb stress transfer [*Dieterich*, 1994]. Hence, the immediate increased rate may not be solely caused by dynamic triggering, especially for a diverse fault geometry region as the SSGF. Following *Toda et al.* [2012], I compute the stress imparted by the El Mayor-Cucapah mainshock on the focal mechanisms in the SSGF prior to the mainshock (Figure 4.12). I use 188 focal mechanisms from *Yang et al.* [2012] with the quality of A during five years

prior to the mainshock. Then, I predict the seismicity rate changes by a rate/state friction implementation of Coulomb stress transfer [*Dieterich*, 1994; *Toda et al.*, 2012]. The quiescence in the SSGF lasted ~150 days after the mainshock until several M>3 earthquakes occurred (Figure 4.11a). Therefore, the aftershock duration t_a is set to 150 days. The rate and state constitutive friction parameter $A\sigma$ is more difficult to constrain, so I apply different values in a wide range from 1 kPa to 500 kPa, which well covers the previously reported 25-100 kPa range [*Cochran et al.*, 2004 and references therein]. Assuming the shear modulus of 35 GPa, the corresponding shear strain rate range is ~0.06-30 μstrain/yr, which brackets the reported shear strain rate of 0.5 μstrain/yr in the SSGF [*Anderson et al.*, 2003]. Figure 4.13 shows the predicted seismicity rate changes from Coulomb stress changes resolved on focal mechanisms in Figure 4.12. I do observe a delayed shutdown of seismicity rate from the prediction of the rate/state friction implementation, but the predicted increase immediate after the mainshock is significantly smaller than that in the detected catalog no matter what $A\sigma$ value is used (Figure 4.13). Hence, while I cannot completely rule out its contribution, the diverse fault geometry in the SSGF probably is not the primary cause for immediate rate increase.

Recently, it is suggested that the net fluid extraction in the SSGF tracks the long-term seismicity rate changes with little time lag, suggesting that seismicity in the SSGF may respond to elastic compaction and subsidence from fluid removal [*Brodsky and Lajoie*, 2013]. Similarly, I examine the correlation between the monthly geothermal injection/production data and smoothed seismicity rate in the SSGF from 2007 to 2011 from the relocated catalog. During the study period, the net production in the SSGF was at a relative low level, which might contribute to the quiescence in T_2. However, most

earthquake swarms and quiescence periods in the SSGF from 2007 to 2011 did not match well with the peaks and troughs in the net production data, respectively. Hence, although the long-term seismicity rate in the SSGF may be influenced by the geothermal production, individual swarm and quiescence may not necessarily be driven by it.

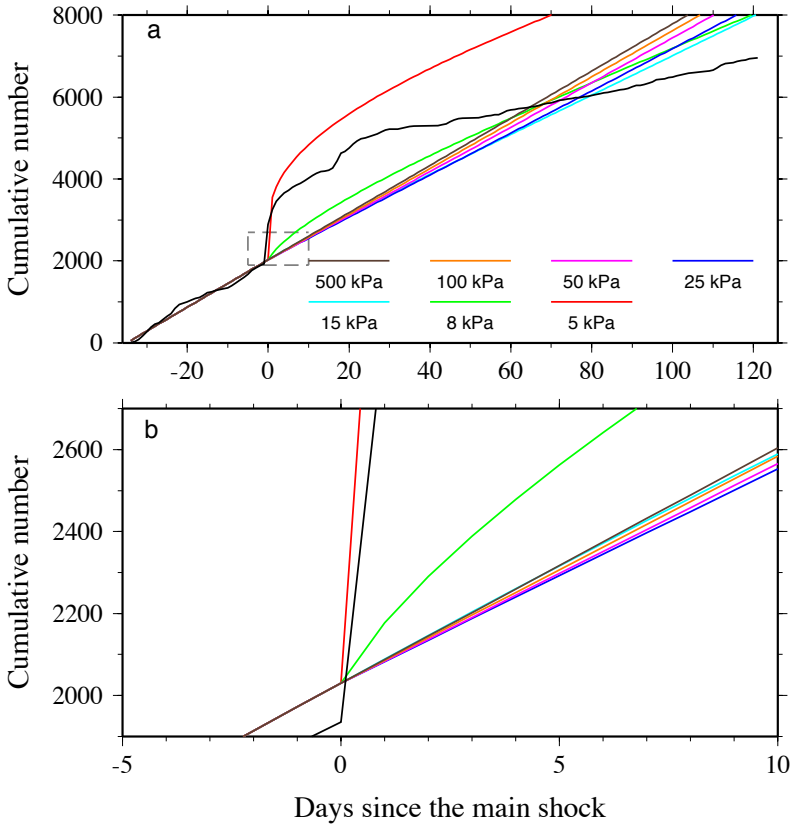

Figure 4.13 (a) Prediction of the cumulative number of earthquakes in the SSGF from the rate/state friction implementation of Coulomb stress transfer. The black curve denotes the observed cumulative number of detected events. The colored curves denote the mean predicted cumulative number for all focal mechanisms in Figure 4.12 with different constitutive friction parameter $A\sigma$. (b) A zoom-in plot of (a) around the time of the mainshock.

Postseismic relaxation, including afterslip [*Peng and Zhao*, 2009], poroelastic rebound [e.g. *Peltzer et al.*, 1998], and viscoelastic relaxation [e.g. *Freed and Lin*, 2001], has also been proposed to explain various triggering cases, especially the 'delayed

triggering'. Moreover, *Dieterich* [1994] shows that if the stress increases with the logarithm of time, the seismicity rate decay also follows Omori's law with the *p*-value close to 1. Using far-field GPS observations, *Pollitz et al.* [2012a] found that the transient postseismic deformation from 2 weeks to 6 months in the epicentral area of the El Mayor-Cucapah mainshock is most likely caused by viscoelastic relaxation of the lower crust and upper mantle. In the SSGF, the transient deformation is ~5 mm from 2 weeks to 6 months after the mainshock, while it is negligible in the SJFZ [*Pollitz et al.*, 2012a]. For vertical strike-slip faults, regions in which coseismic stress changes are positive and negative tend to become more positive and negative, respectively, due to viscoelastic relaxation [*Freed*, 2005]. Therefore, the longer-term seismicity rate in the SSGF might be further prohibited by postseismic relaxation. However, the seismicity rate increase in the SJFZ may not be affected by postseismic relaxation.

Finally, one may argue that the quiescence in the SSGF is a result of most accumulated stresses spent by earthquakes immediately following the mainshock. That is, a rate increase by clock-advance followed by apparent rate decrease [*Gomberg et al.*, 1997]. If true, the total number of earthquakes should be similar or higher than that extrapolated from the background rate, since only transient dynamic stresses have been added to the system. However, the total number of earthquakes in the SSGF is evidently lower than that predicted by the background rate (Figure 4.2b), hence the longer-term seismicity in the SSGF is more likely halted by the 'stress shadow' than clock-advanced by dynamic stresses.

4.9 Conclusion

By applying the matched filter technique, I obtained a more complete catalog in

the SSGF and the SJFZ around the occurrence time of the 2010 El Mayor-Cucapah mainshock. With the detected catalog, I found a statistically significant increase of seismicity rate immediately after the mainshock in both study regions. Such short-term increases can be best explained by dynamic triggering, due to the evidences of surface wave triggering and Omori-decay of seismicity rate. In the longer-term, the seismicity rate changes in both regions are consistent with the static Coulomb stress changes pattern induced by the mainshock.

At the current stage, I cannot completely rule out other factors that may also contribute to the seismicity rate changes, such as diverse focal mechanisms, anthropogenic activity (i.e., geothermal production), postseismic relaxation (i.e., afterlip, poroelastic rebound and viscoelastic relaxation) and secondary triggering mechanisms. However, the observations found in this and other recent studies [*Shelly and Johnson*, 2011; *Toda et al.*, 2012; *Meng et al.*, 2013] suggest that 'stress shadow' does exist and likely play a very important role in controlling the seismicity patterns in the immediate vicinity of a mainshock. In summary, dynamic stress changes are larger in amplitude but transient, while static stress changes decay much faster with distance but are permanent. Hence, in the short term immediately after the mainshock, dynamic stress change is the dominant mechanism, but is likely replaced by static stress change after certain time.

CHAPTER 5

IMPROVED UNDERSTANDING OF MODERATE-SIZE EARTHQUAKE SEQUENCES ON THE SAN JACINTO FAULT AND THEIR RELATIONSHIP WITH DEEP CREEP

5.1 Introduction

Interseismic strain accumulations between the North America and Pacific plates are mostly accommodated by the San Andreas Fault System (SAFS). In southern California, the SAFS branches into the southern San Andreas Fault (SSAF), the San Jacinto Fault (SJF) and the Elsinore Fault (Figure 5.1). The slip rate across the SAFS varies significantly. Along the SSAF and SJF, the best-fitting model suggests a slip rate of 25 mm/yr and 21 mm/yr, respectively, while no significant slip occurs on the Elsinore Fault [*Fialko*, 2006]. Although the SSAF and SJF have very similar slip rates, the seismic activities along the two faults are markedly different. The SJF hosted more than 10 earthquakes with magnitude between 6 and 7 in the last century [*Rockwell et al.*, 1990], as well as numerous smaller ones. In contrast, the SSAF was completely devoid of seismicity, from microearthquakes to large ones, in historical times. Using geodetic data, *Fialko* [2006] inferred that the entire seismogenic zone is locked beneath the SSAF (i.e., 0-17 km), while the locking depth is only ~12 km beneath the SJF, well above the bottom of the seismogenic zone (17 km). The disagreement between geodetic and seismic data led *Wdowinski* [2009] to speculate that, between the locking depth and the bottom of the seismogenic zone, the SJF releases elastic strain both seismically (small to moderate-size earthquakes) and aseismically (creep).

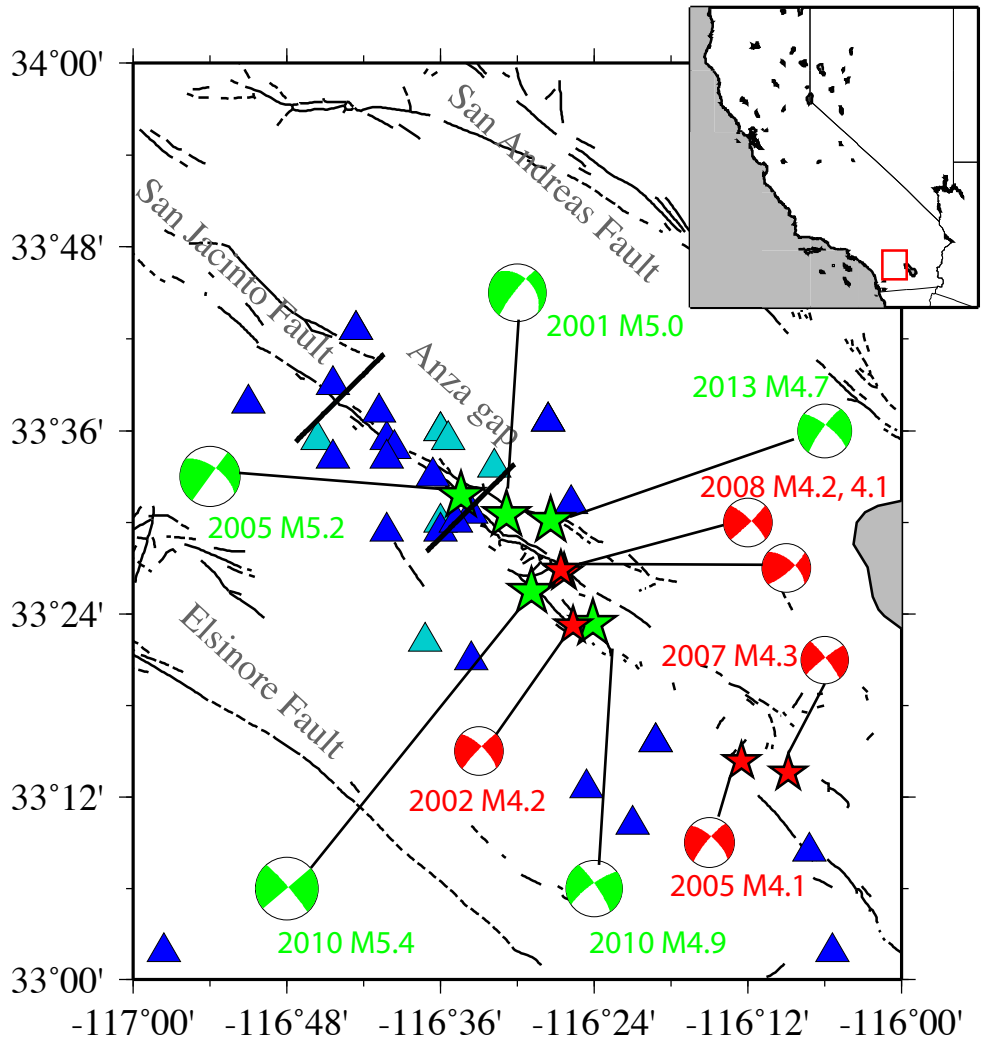

Figure 5.1 Map of the study region. Black lines denote the active faults. Green and red stars denote the epicenters of M>4.5 and M<4.5 earthquakes, respectively. Beach balls denote the focal mechanisms of 10 moderate earthquakes. Cyan and blue triangles denote the PBO and AZ network, respectively. The thick black lines mark the Anza gap. The zoom-in plot shows the location of the study region in the state of California.

A 20-km-long segment along the central SJF, termed the Anza seismic gap [*Sanders and Kanamori*, 1984], has not experienced any major seismic activity since instrumental records have been kept (Figure 5.1). Many studies suggested that the stored shear strains in the Anza gap is likely released by a large earthquake (M~7) in the near future and impose great seismic hazard to southern California [*Thatcher et al.*, 1975;

Sanders and Kanamori, 1984; *Sykes and Nishenko*, 1984; *Rockwell et al.*, 1990]. As a result, the Anza gap is one of the most closely monitored regions in California. Since 1980s, a dozen of permanent broadband seismometers from the AZ network have been continuously recording local and regional seismicity around the Anza gap since 1980s [*Fletcher et al.*, 1987]. Six borehole seismometers were deployed around the Anza gap as a part of the Plate Boundary Observatory (PBO) network in 2006. Although devoid of major events, moderate-size earthquakes (i.e., M 4-5) occur frequently around the Anza gap. Those events are of particular importance because they may provide seismological evidences on whether deep creep occurs along the root of the SJF, which could help to better define the locking depth and the maximum magnitude of future earthquakes in the Anza gap.

Using standard Southern California Seismic Network (SCSN) catalog, [*Wdowinski*, 2009] found anomalously long aftershock zones of the 2001 M5.0 and 2005 M5.2 earthquakes near the southern end of the Anza gap and proposed that they were driven by deep creep along the SJF. However, many studies have shown that standard seismic catalogs are incomplete, especially right after moderate-to-large earthquakes [*Peng et al.*, 2006; *Peng et al.*, 2007]. Specifically, *Kilb et al.* [2007] has shown that a significant fraction of early aftershocks was missing following the 2001 M5.0 Anza earthquake. Those early aftershocks are crucial for illuminating the genuine seismicity rate changes and migration pattern, and hence could shed new insight on the triggering mechanism.

Since the publication of *Wdowinski* [2009], 3 more earthquakes with M~5 occurred near the Anza gap (Figure 5.1). Moreover, 5 earthquakes with slightly smaller

magnitudes (M~4) occurred in the same region since 2000 (Figure 5.1). Therefore, the dense seismic instrumentation and abundant seismic activity provide an ideal dataset to evaluate the physical mechanism of aftershock triggering along the SJF. In addition, I apply a recently developed matched filter technique [*Peng and Zhao*, 2009] to automatically detect missing early aftershocks and use them to better quantify spatial-temporal evolutions of aftershocks, and their possible relationships with deep creep along the SJF.

Table 5.1 10 moderate earthquakes along the SJF since 2001

Date	Time	Lon.	Lat.	Depth	M_w	Strike	Dip	Rake
10/31/2001	07:56:16	-116.50	33.50	16.83	5.0#	218#	82#	-47#
01/02/2002	12:11:29	-116.43	33.39	11.28	4.2#	223#	85#	-18#
05/21/2005	00:39:33	-116.21	33.24	10.65	4.1*	322*	83*	-175*
06/12/2005	15:41:46	-116.57	33.53	15.48	5.2#	216#	90#	-28#
02/09/2007	03:33:44	-116.14	33.22	10.16	4.3*	313*	71*	-170*
05/01/2008	03:55:36	-116.44	33.45	8.13	4.2#	49#	77#	29#
05/09/2008	22:38:08	-116.44	33.45	8.04	4.1*	314*	78*	175*
06/13/2010	03:08:57	-116.40	33.39	8.35	4.9#	234#	77#	-9#
07/07/2010	23:53:33	-116.48	33.42	12.83	5.4#	49#	90#	5#
03/11/2013	16:56:06	-116.46	33.50	12.33	4.7#	216#	86#	-16#

The parameters are obtained from *Ross et al.* [2015].
* The parameters are from *Yang et al.* [2012].

5.2 Data and Method

In this study, I select 10 M>4 earthquakes and their aftershock sequences near the Anza gap since 2000 (Table 5.1). The origin times and hypocenters of the 10 earthquakes are obtained from the relocated catalog [*Hauksson et al.*, 2012] and its updated online

version

(http://service.scedc.caltech.edu/ftp/catalogs/hauksson/Socal_focal/fm_2011_2013.hash). *Ross et al.* [2015] applied the generalized 'Cut and Paste' method to 7 out of the 10 targeted earthquakes and derived their focal mechanisms and moment magnitude M_w, which are used in this study. For the remaining 3 earthquakes, I use the focal mechanisms and M_w derived by *Yang et al.* [2012]. The continuous data is 4 days before to 7 days after each targeted earthquake. I use both AZ and PBO network for 6 earthquakes after 2006 and AZ network only for 4 earthquakes before 2006 (Figure 5.2 and S5.1). The template events are earthquakes half year before and after each targeted mainshock in its vicinity (i.e., within ~50 km from the epicenter) from the relocated catalog [*Hauksson et al.*, 2012] and the updated online version (Figure 5.2 and S5.1). Both continuous and template waveforms are band-pass filtered from 2 to 8 Hz and then down-sampled to 20 Hz.

The detection procedure follows that described in Chapter 2 and is briefly described here. I compute the correlation-coefficient (CC) between the template and continuous waveform in a 5 s time window starting 1 s before the *P*-wave on the vertical component and 1 s before the *S*-wave on the two horizontal components. The computing time window moves forward by one data point (i.e., 0.05 s). Then, I compute the mean CC for all channels at each time point allowing one data point shift. The detection threshold is set to be the sum of the median value and 12 times the MAD of the mean CC trace. The location of the detected event is assigned to be the same with that of the corresponding template event with the highest mean CC. The magnitude of detected

event is computed based on the peak amplitude ratios between the detected and template event.

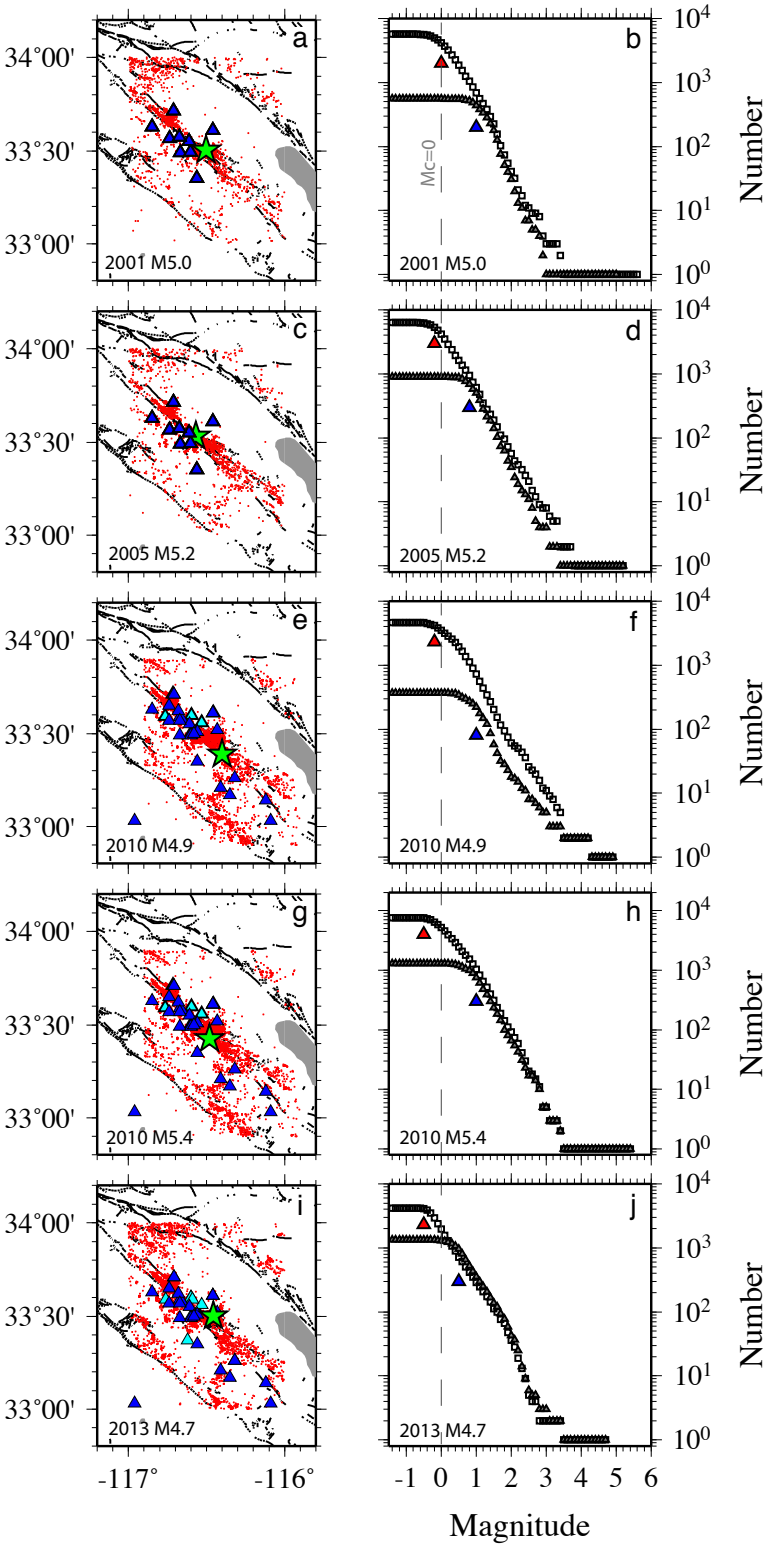

Figure 5.2 (Left) Cyan and blue triangles denote the PBO and AZ network, respectively. Red dots denote template events. Green star denotes the epicenter of the mainshock. (Right) Frequency-magnitude relationship of the SCSN (black triangle) and detected catalog (open square). Blue and red triangle denote the M_c for the SCSN and detected catalog obtained by ZMAP [*Wiemer*, 2001], respectively. Grey dashed line marks the actual M_c used for analysis in this study.

5.3 Results

I obtain 10 newly detected catalogs for all targeted earthquake sequence. The detected catalogs contain at least 5 times more earthquakes than the Southern California Seismic Network (SCSN) catalog in the same time-space window (Figure 5.2 and S5.1). Many early aftershocks that are missing from the SCSN catalog are recovered in the detected catalogs (Figure 5.3). The magnitude of completeness (M_c) is also reduced by half to one order of magnitude after detection. To keep consistency among 10 earthquake sequences, I conservatively select M_c=0 for all detected catalogs and use it for the analysis throughout the paper.

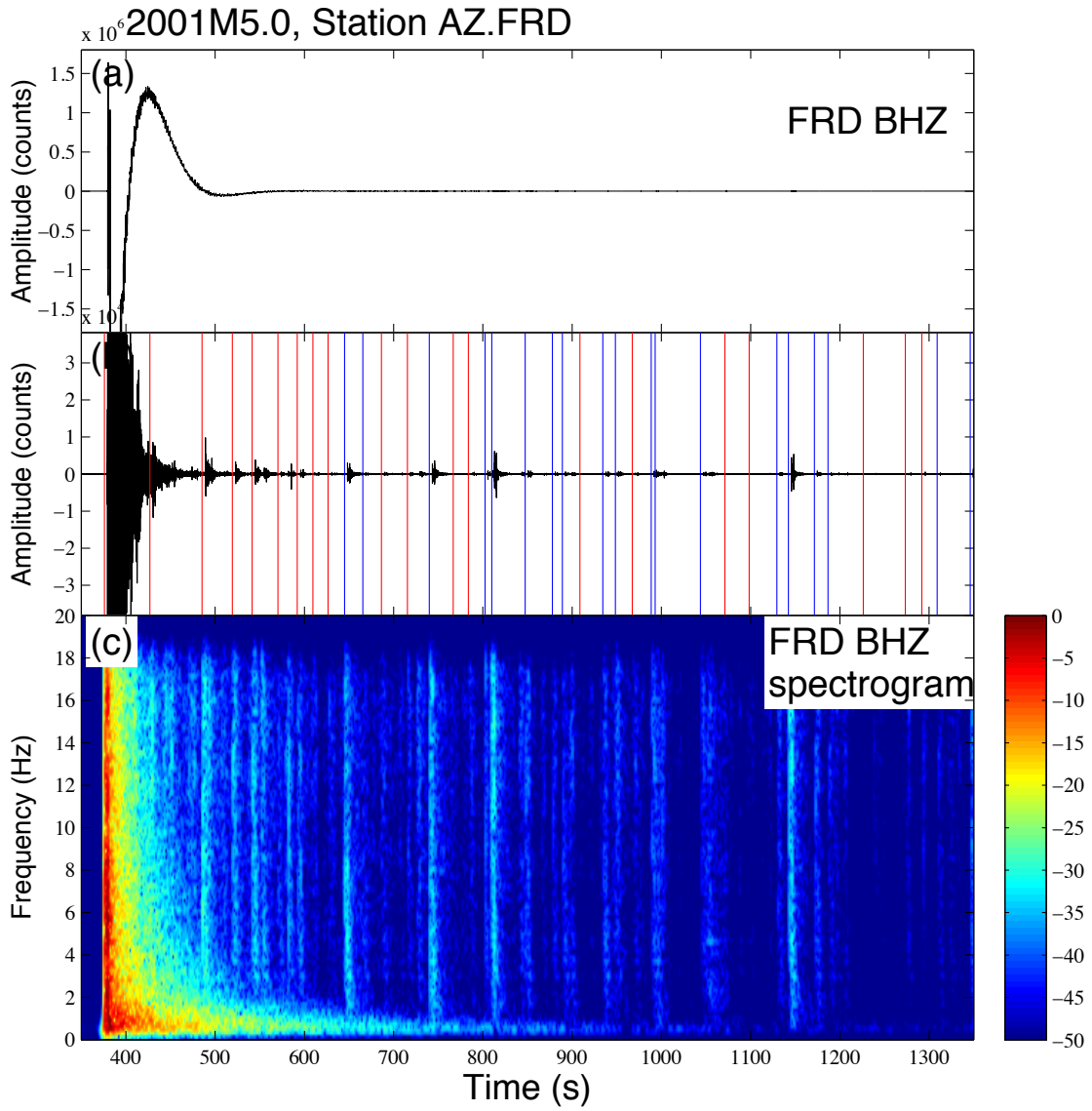

Figure 5.3 Early aftershocks of the 2001 M5.0 earthquake. (a) Raw data recorded by the vertical channel at station FRD. (b) 2-8 Hz band-pass filtered waveform. Red lines denote the detected aftershocks. (c) Spectrogram immediately following the 2001 M5.0 event.

5.3.1 Aftershock Zone

I first quantify the aftershock zone for each M>4 earthquake. The definition of aftershock zone is ambiguous [*Kagan*, 2002]. Many studies outline aftershock zone by simply examining the spatial distribution of seismicity following the mainshock [e.g.,

Das and Henry, 2003]. However, in regions with very high background seismicity (e.g., the SJF), this approach may overestimate aftershock zone by including areas that are already active before mainshock. In this study, I define aftershock zone as regions with significant seismicity rate increase comparing to pre-mainshock level. The significance of seismicity rate change is quantified by the β-value, which measures the deviation of seismicity rate in interested time period from the background rate [e.g., *Reasenberg and Matthews*, 1988; *Aron and Hardebeck*, 2009]. β-value larger than 2 is regarded as significant rate increase at 95% confidence level [*Hill and Prejean*, 2007].

Since I am mostly interested in deep creep propagating along the SJF, I focus on the along strike extension (hereafter, length) of the aftershock zone. I first divide the SJF trace into non-overlapping 1-km-long and 10-km-wide segments, starting from the epicenters and extending toward both NW and SE. The dimension of segment reflects a compromise between enough number of earthquakes in each segment and the resolution of the aftershock zone. Then, I compute the β-value in each segment with at least 10 earthquakes in the newly detected catalog with M>0, otherwise the β-value is set as 0. The aftershock zone is defined as segments experienced significant rate increase (Figure 5.4 and S5.2). For a few events, I observe gaps within the region with significant seismicity rate increase. If the gap spans no more than 2 km, I disregard the discontinuity (e.g., the 2001 M5.0 and 2010 M5.4 events); otherwise I consider it as the terminus of the aftershock zone (e.g., the 2005 M5.2 event).

As a result, I find clear along strike extension of aftershocks for 5 M>4.5 events and the 2002 M4.2 event (Figure 5.4). For each sequence, more than 90% earthquakes following the mainshocks were located in the defined aftershock zone, which further

validate the identification of the aftershock zone. Despite similar magnitudes, remarkable variations are identified in the lengths of aftershock zone for 5 M>4.5 events. For the event (i.e., the 2010 M4.9) occurred in the shallow part of the seismogenic zone (<10 km in depth), its aftershocks were tightly clustered around the hypocenter and showed very little extension along the SJF strike. The other 4 M>4.5 events occur near or below the inferred locking depth of the SJF (i.e., 12 km), and their aftershocks clearly extend bilaterally and form significantly longer aftershock zones. Another interesting feature is that their aftershocks were located exclusively updip to the respective mainshocks (Figure 5.4). For the 5 M<4.5 events, only the 2002 M4.2 earthquake, which is the deepest one (~11.3 km in depth), has a distinguishable aftershock zone. The lengths of aftershock zone of the other 4 M<4.5 events are equal to or smaller than the resolution of 1 km (Figure S5.2).

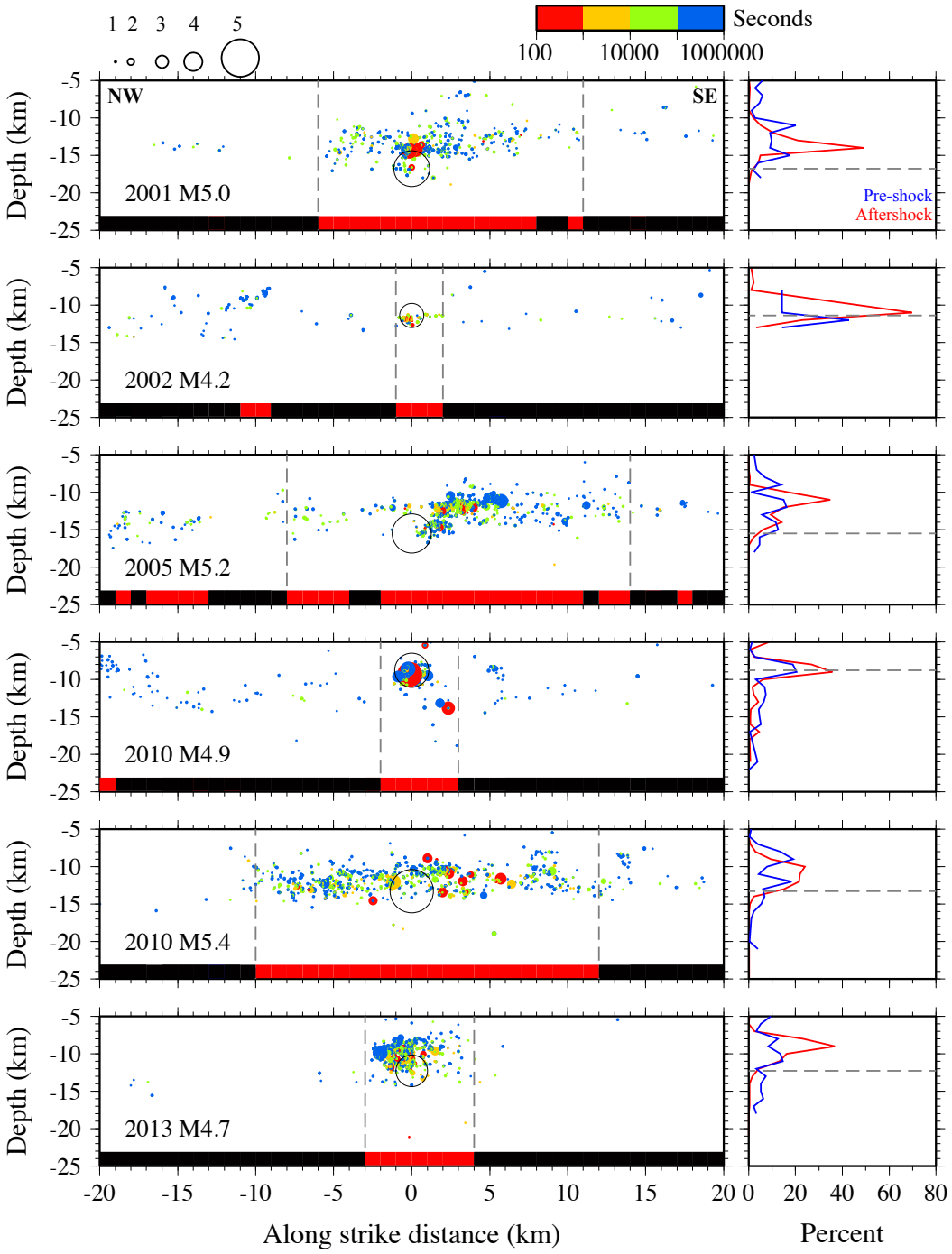

Figure 5.4 (Left) The cross-section view of aftershock distribution of 5 M>4.5 and the 2002 M4.2 earthquakes. Circles denote locations of the aftershocks, which are scaled by magnitude and color-coded by origin time. Black and red bars at bottom denote segments with β<2 and β>2, respectively. The grey dashed lines mark the defined aftershock zone. (Right) The histogram of depth distribution of earthquakes before (blue) and after (red) the mainshock, respectively. The grey dashed line denotes the focal depth of the mainshock.

5.3.2 Aftershock Rate Changes

The 5 M>4.5 earthquakes triggered numerous aftershocks in the whole study regions (Figure 5.5). The seismicity rate decayed with time, but remained higher than the background level at the end of the study periods (7 days). In contrast, 5 M<4.5 earthquakes only caused moderate increase of seismicity in the vicinity, and the seismicity rate decayed to background level within one day (Figure S5.3). I then examine the aftershock rate changes in detail within the previously defined aftershock zones for 5 M>4.5 events and the 2002 M4.2 event by computing the smoothed seismicity rate using a sliding data window of 20 events (Figure 5.6). The evolutions of aftershock rate of 5 M>4.5 events are virtually identical, despite the marked differences in the lengths of aftershock zone. From 1,000 s to 10,000 s following the mainshocks, the aftershock rate remains high and shows very little decay. Later, I observe acceleration in the decay rate, but still lower than the typical Omori decay (i.e., p=1) [*Omori*, 1894; *Utsu et al.*, 1995], till the end of the study period. The aftershock sequence of the 2002 M4.2 event, on the other hand, has a typical Omori decay with p very close to 1. The other 4 M<4.5 events produced too few aftershocks to establish meaningful aftershock decay curve.

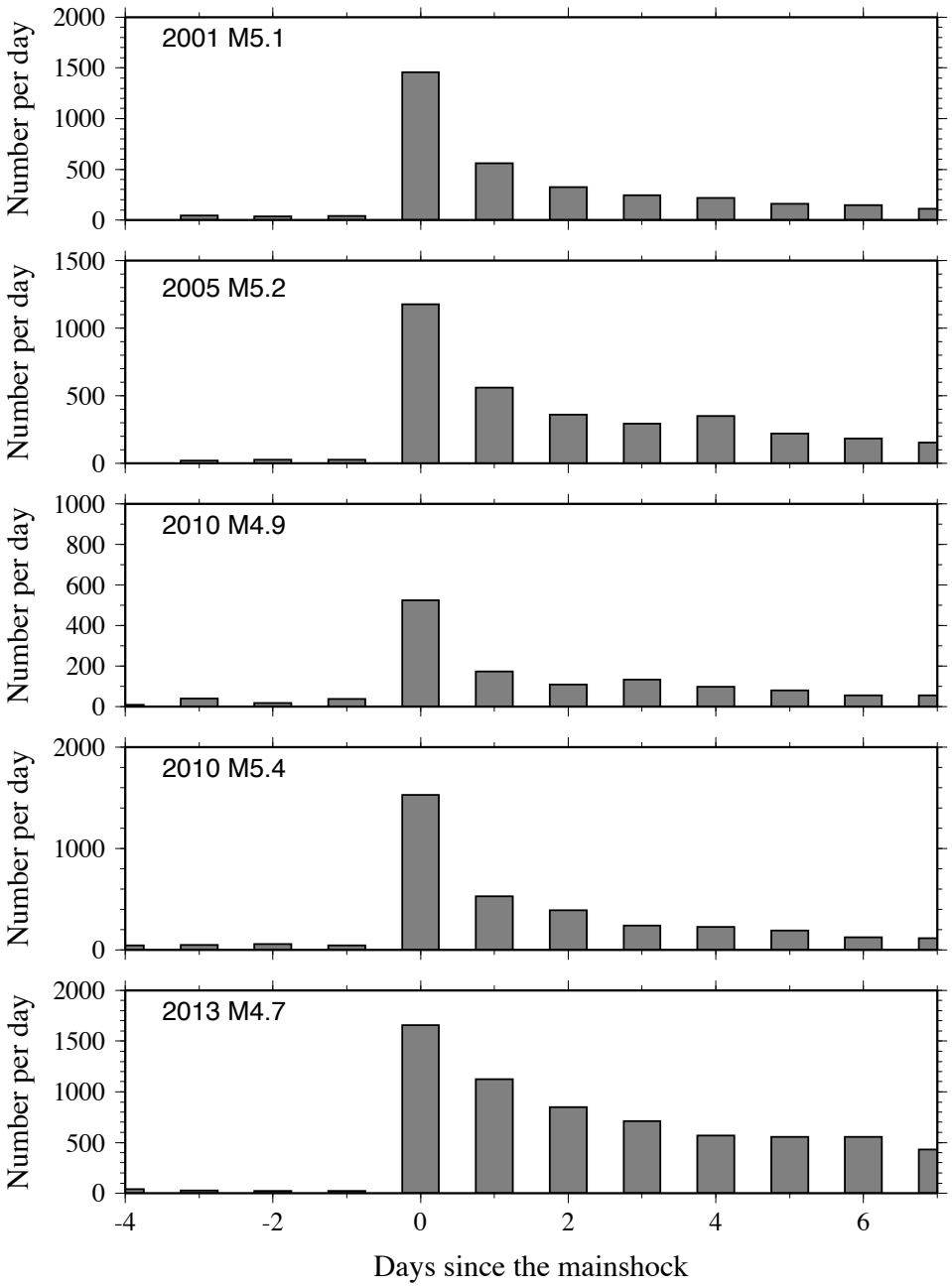

Figure 5.5 Daily seismicity rate for 5 M>4.5 earthquakes.

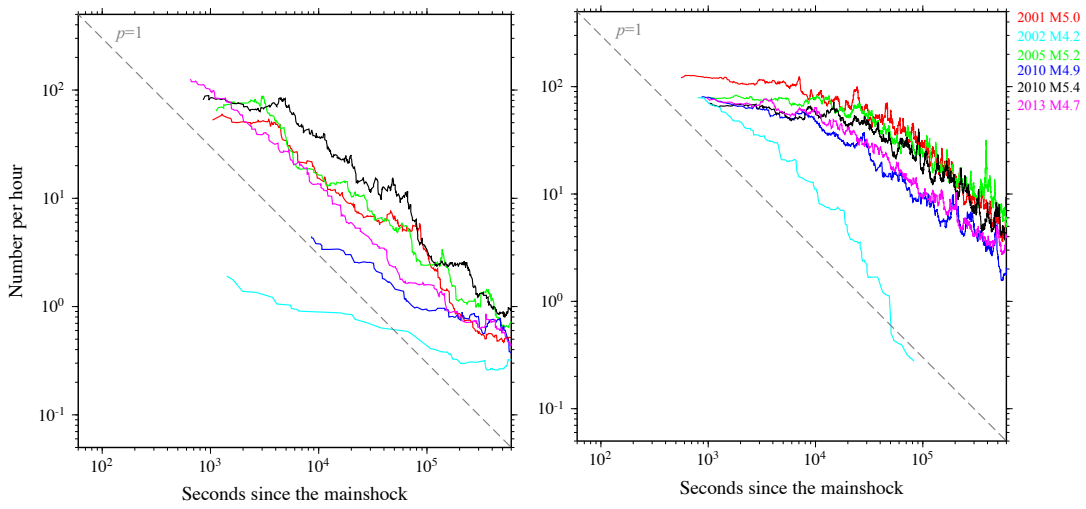

Figure 5.6 (Left) Smoothed aftershock rate changes following the 5 M>4.5 and the 2002 M4.2 earthquakes from the SCSN catalog with M>1. **(Right)** Same figure from the detected catalogs with M>0.

5.3.3 Migration of Aftershocks

Next, I investigate whether migration of aftershocks and/or repeating earthquakes occur following the mainshocks (Figure 5.7). Repeating earthquakes, or repeaters, are a set of events that rupture the same fault patch and produce highly similar waveforms at recording stations [e.g., *Nadeau et al.,* 1995; *Peng et al.*, 2005; *Zhao and Peng*, 2009]. Those patches can be loaded and rupture repeatedly during creep episodes, hence repeaters are often used to identify creep and/or slow slip [*Kato et al.*, 2012]. However, because of the short study period, I could not well establish families of repeaters. Instead, I identify events that are highly correlated (i.e., CC>0.9) with one or more templates, which may be members of repeater families. Among 5 M>4.5 events and the 2002 M4.2 event, I do not observe clear migration of aftershocks following any mainshock (Figure 5.7). For the 2005 M5.2 and 2010 M5.4 events, there might be bilateral migration within the aftershock zone, but the migration fronts are outlined by handful aftershocks and thus

not reliable. Similar observation can be made for highly-correlated events as well. That is, no evident migration pattern can be concluded. Then, I compute the lengths of aftershock zone using the same method in section 3.1 at 5,000 s, 10,000 s, 20,000 s, 50,000 s and 1 day following the mainshocks (Figure 5.7). For the 2002 M4.2 and 2010 M4.9 earthquakes, due to the small size of their aftershock zones, I do not see expansion of aftershocks with time. The lengths of aftershock zone of the 2001 M5.0, 2005 M5.2 and 2013 M4.7 earthquakes expand gradually with time. The aftershock zone of the 2010 M5.4 event increases very fast in the first 20,000 s and remained stable afterwards.

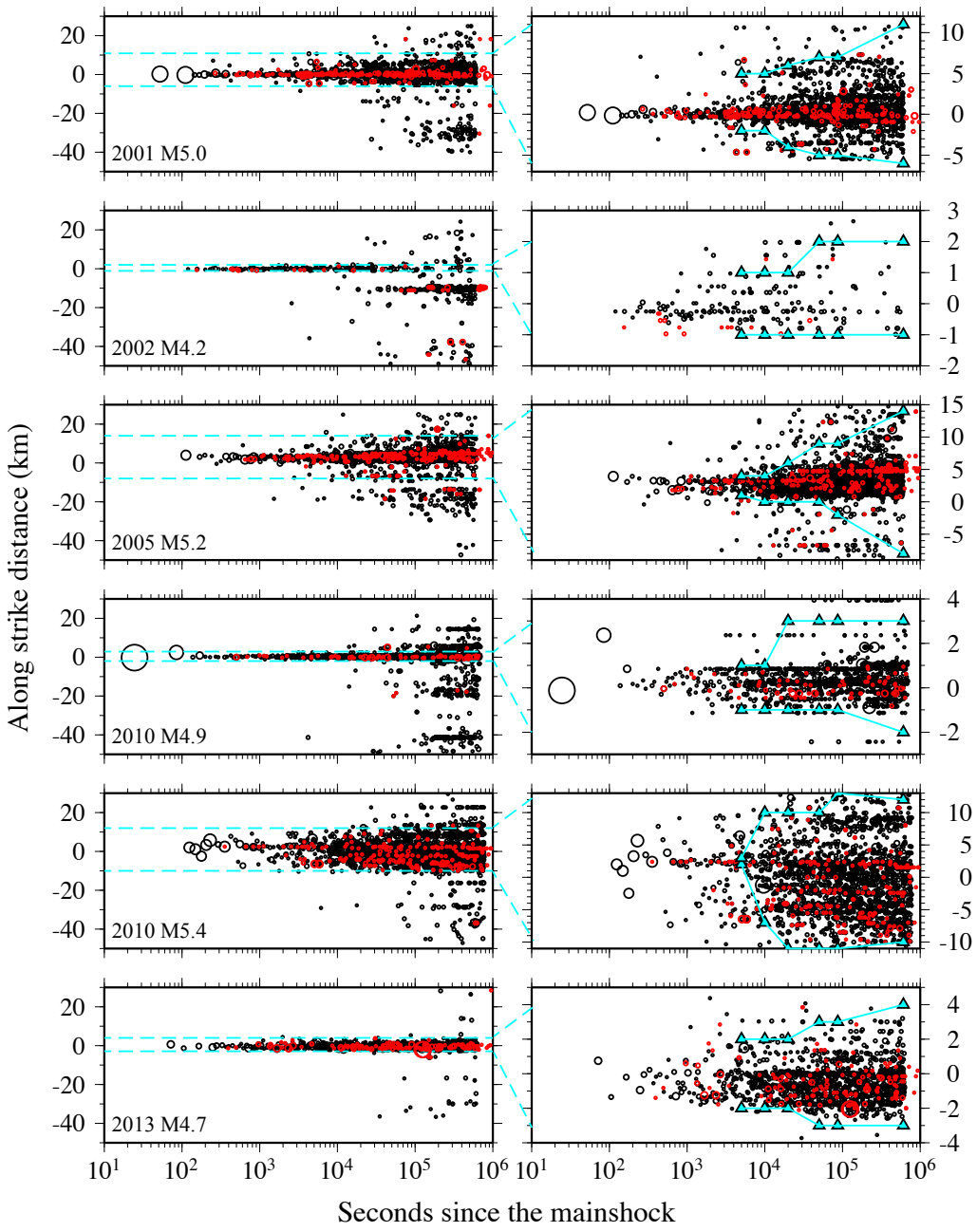

Figure 5.7 Migration pattern of aftershock sequences. (Left) Along strike distance versus time for all aftershocks (black circle) and highly-correlated events (red circle). Cyan dashed lines mark the defined aftershock zone from Figure 2. (Right) The zoom-in plot around the defined aftershock zone. Cyan triangles mark the aftershock zone at 5,000 s, 10,000 s, 20,000 s, 50,000 s, 1 day and 7 days after the mainshock.

5.4 Discussion

The computed lengths of aftershock zone of 10 M>4 earthquakes near the Anza gap demonstrate a dependence on focal depth (Figure 5.4 and S5.2). To better illustrate their relationship, I plot the length of aftershock zone versus focal depth (Figure 5.8). It is worth noting that, for the 2005, 2007 and 2008 M~4 events, their aftershock zones are not well resolved (Figure S5.2), hence their lengths in Figure 5.8 may be overestimated. It is evident that the lengths of aftershock zone contrast sharply between events occurring in the shallow and deep part of seismogenic zone. However, the contrast in the sizes of aftershock zone can also be contributed by the variations in moment magnitude M_w, fault geometry and stress drop. Hence, I need to examine how the aforementioned factors affect the observed depth dependence of aftershock zone.

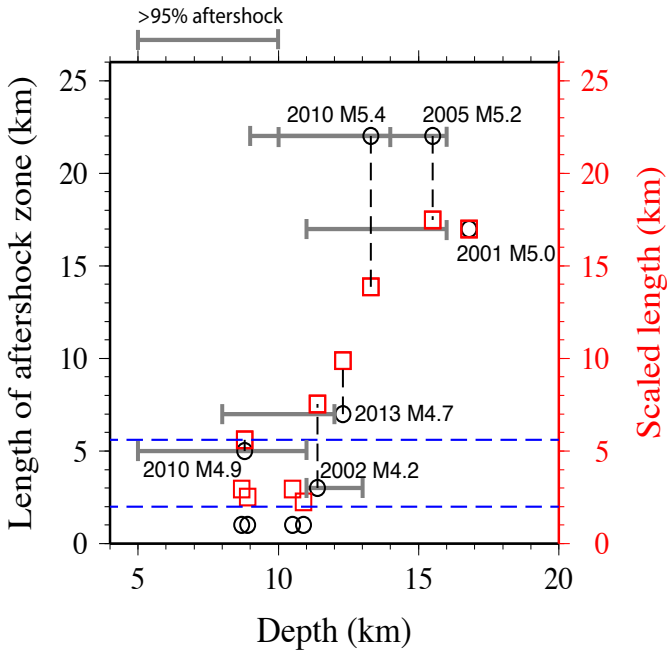

Figure 5.8 Lengths of aftershock zone versus focal depth for 10 moderate earthquakes. Black circles denote the original lengths of aftershock zone from Figure 5.4 and S5.2. Grey horizontal lines denote the depth distribution of >95% aftershocks. Red squares denote the scaled lengths of aftershock zone. Blue dashed lines mark the upper and lower limit of the aftershock zone of M_w 5 earthquakes by *Wells and Coppersmith* [1994].

M_w is the primary factor in controlling the size of aftershock zone. To correct for the differences, I scale the lengths of aftershock zone to that of 5 events. Assuming a constant stress drop, it is well established that $M_0 \sim S^{1.5}$ and $M_0 \sim L^3$ [e.g., *Kanamori and Brodsky*, 2004], where M_0 is the seismic moment, S is the rupture area and L is the rupture length. After scaling, the length of aftershock zone still correlates positively with focal depth (Figure 5.8). The rupture lengths of 5 strike-slip earthquakes generally lie in 3-6 km [*Wells and Coppersmith*, 1994], which is comparable to that of the shallow 2010 M4.9 event. For the 2002 M4.2 and 2013 M4.7 events that occur near the locking depth, the scaled aftershock zones are slightly larger than the maximum rupture length. Below 12 km, aftershocks of the deep events extend 2 to 3 times the average rupture length of 5 events. The boundary between normal and anomalously large aftershock zones coincides with the geodetically inferred locking depth of 12 km, which strongly indicates that deep creep triggered by mainshocks drive the aftershock sequences well beyond the rupture length.

Fault discontinuities, such as terminus, bend and stepover, can also control the size of aftershock zone [e.g., *Wesnousky*, 2006]. The study region is one of the most complicated tectonic areas in California [e.g., *Allam et al.*, 2014], where the SJF branches into three segments (i.e., Trifurcation area). From southwest to northeast, the three segments are the Coyote Creek Fault, the Clark Fault and the Buck Ridge Fault, which are all NW striking right-lateral faults. The right and left stepping of the Coyote Creek Fault and the Buck Ridge Fault form a releasing bend and restraining bend, respectively. Moreover, many secondary fault segments and discontinuities can be clearly seen through the surface expression [*Sanders and Kanamori*, 1984] and revealed by the rather

heterogeneous focal mechanisms in the study region [*Bailey et al.*, 2010]. With the 10 M>4 earthquakes occurring on different fault segments, the rather complex fault geometry may play an important role in the size of aftershock zone. For example, the 2010 M4.9 event ruptured a small fault segment that appears disconnected with main fault traces on surface (Figure 5.1). If the disconnection extends to the focal depth, the fault terminus may limit the size of the aftershock zone. However, at current stage, I am not able to accurately evaluate the effects of fault discontinuities due to the poor understanding of fault structure at depth.

The size of aftershock zone is also a function of focal mechanisms [*Wells and Coppersmith*, 1994]. Although focal mechanism solutions for the 10 M>4 earthquakes all show strike-slip events with one nodal plane aligned with the SJF strike (Figure 5.1), it is possible that earthquakes with relative small aftershock zones ruptured a cross fault instead (i.e., NE striking left-lateral fault) [e.g., *Mori*, 1993], which results in the limited extension along the SJF. It is also suggested that the 2001 M5.0 and 2005 M5.2 events, which have the longest aftershock zones, may be left-lateral strike-slip events that occur on cross faults.

To better evaluate the actual rupture planes, I compute the β-value map for each moderate earthquake. I divide the study region into grids of 0.01° by 0.01° and compute the β-value in each grid with no less than 10 earthquakes. Similarly, I can identify aftershock zone for 5 M>4.5 events and the 2002 M4.2 event (Figure 5.9), all of which have comparable normal-to-fault extension with along strike extension. Therefore, it is difficult to differentiate the rupture plane and the auxiliary plane simply based on the shape of aftershock zone. Nevertheless, to avoid the bias toward the events on cross faults,

I also obtain the area of aftershock zone as the total number of grids with β>2. In some cases, I find that a few grids with β>2 are well separated from the main cluster, which are more likely caused by random chances and hence are not counted toward the area of aftershock zone. The 2001 M5.0, 2005 M.2 and 2010 M5.4 events have significantly larger aftershock zones than the others (Figure 5.10). After scaling assuming $M_0 \sim S^{1.5}$, I find two groups of events are well separated around the depth of 11 km. In summary, the previously observed trend in the lengths of aftershocks zone is still evident. It is undisputed that deeper mainshocks near the Anza gap tend to have larger aftershock zones, no matter which fault plane is ruptured.

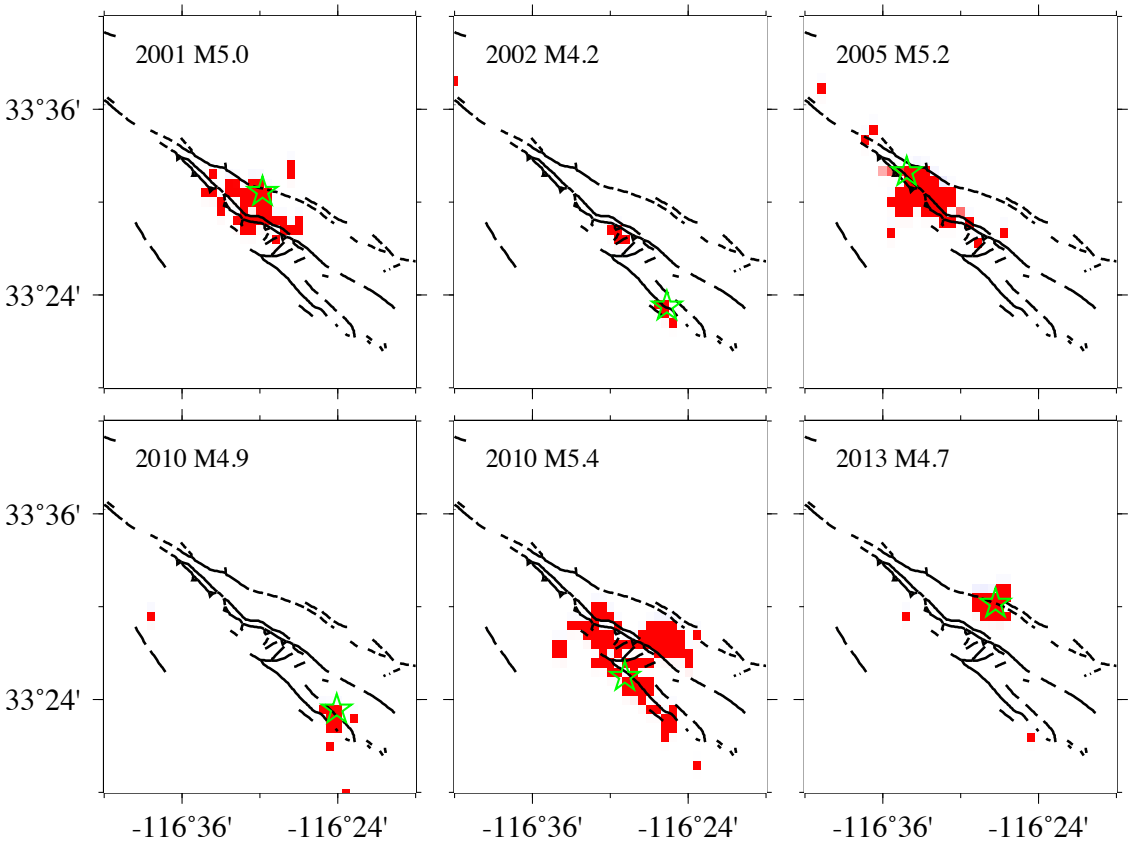

Figure 5.9 The β-value map of 5 M>4.5 and the 2002 M4.2 earthquakes. Red grids denote β >2. Green star denotes the epicenter of the mainshock.

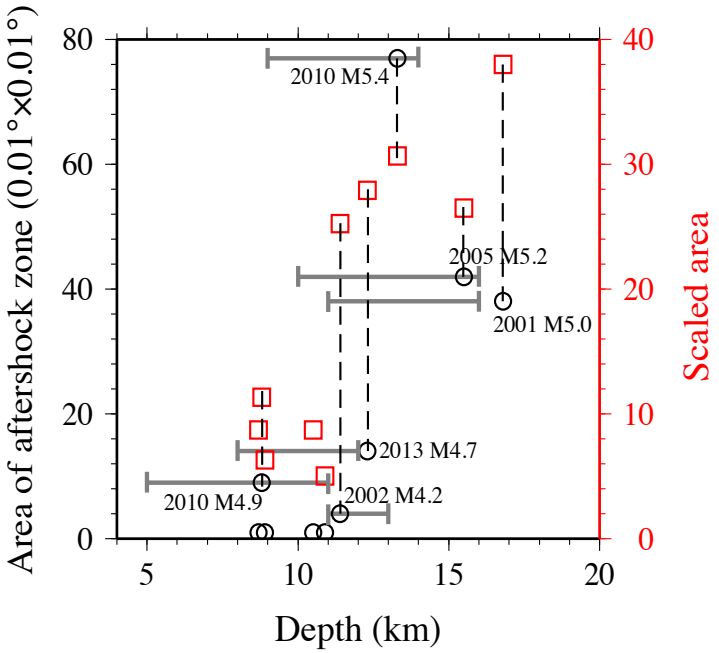

Figure 5.10 Areas of aftershock zone versus focal depth for 10 moderate earthquakes. Black circles denote the original areas of aftershock zone. Red squares denote the scaled areas of aftershock zone. Grey horizontal lines denote the depth distribution of >95% aftershocks.

Earthquakes with lower stress drop tend to have larger aftershock zone [e.g., *Kanamori and Brodsky*, 2004]. Previous scaling relationships assume constant stress drop for all earthquakes, which is generally a good assumption for a large dataset. However, individual event can also have stress drop significantly deviated from the average value. For example, *Mori* [1993] found that the 1990 M4.2 Buck Ridge earthquake has a much smaller stress drop and larger aftershock zone than other 2 earthquakes with similar magnitude along the SJF. Stress drop does show depth dependence as well [*Hardebeck and Aron*, 2009 and references therein]. Deeper earthquakes tend to have larger stress drop and thus smaller aftershock zone, which contradicts the observation in this study.

However, stress drop also varies with shear strength of the fault [*Hardebeck and Aron*, 2009]. If true, the anomalously larger aftershock zone, thus smaller stress drop, of deeper earthquakes also reflects a much weaker deep seismogenic zone along the SJF as inferred by geodetic data.

The presence of deep creep near the Anza gap has also been directly observed or interpreted from geodetic measurements. *Agnew and Wyatt* [2005] reported clear strain rate changes from long-base strainmeters at Pinon Flat Observatory (PFO) over 7 days after the 2005 event and interpreted them as deep aseismic slip triggered by the mainshock. A two-week-long strain transient was recorded by long-base strainmeters at PFO and newly deployed borehole strainmeters from the PBO network following the 2013 M4.7 event [*Hodgkinson*, 2013]. Such strain transients can be explained as re-equilibrium process of disturbed pore pressure distribution or deep creep. Similar responses of strainmeters were observed for the 2001 M5.0 event at PFO and the 2010 M5.4 event from the PBO network, but not for the shallow 2010 M4.9 event. Recently, *Lindsey et al.* [2014] found anomalously high strain rate within the shear zone of the SJF near the Anza gap, using high-density GPS and InSAR data and incorporating the recent tomographic results [*Allam et al.*, 2014]. The anomalously high strain rate can be explained by deep creep at near the full long-term slip rate.

Migration of seismic events is usually used as the hallmark of the presence of creep and/or slow slip within the fault zone. For example, it is suggested that slow slip leads up to the 2011 M_w 9.0 Tohoku-Oki earthquake because of foreshocks migrating toward the eventual nucleation point of the mainshock [*Kato et al.*, 2012]. Similarly, the aftershocks of the 2004 M_w 6.0 Parkfield earthquake migrate along the creep section of

the SAF due to afterslip [*Peng and Zhao*, 2009]. However, I do not see well-defined migration pattern of aftershocks associated with deep earthquakes, although creep likely occurred. Comparing to the 2004 Parkfield and 2011 Tohoku-Oki earthquakes, the absence of migration may be contributed by the less energic creep episodes triggered by relative small mainshocks, which triggered too few aftershocks to outline the migration front. Plus, high background seismicity in the study region also impedes me from identifying migration of aftershocks. Finally, the hypocenters of detected events are assigned to be the same with that of templates. Hence, it is possible that many aftershocks along the migration front collapse into one location and make it indistinct. Although no clear migration of aftershock, I do observe that the aftershock zones of deeper events increase with time, which indicates the existence of creep.

Last but not least, dynamic triggering can also explain aftershocks well beyond the rupture plane [e.g., *Hill and Prejean*, 2007]. *Felzer and Kilb* [2009] found that the seismicity density following the 2001 M5.0 and 2005 M5.2 event decayed with distance at a constant rate similar with elsewhere in California up to ~50 km in the first two days, which can be only explained by dynamic triggering. However, *Richards-Dinger et al.* [2010] demonstrated that a similar decay can be observed for earthquakes prior to the mainshock, as well as aftershocks occurred before the arrival of seismic waves, therefore the decay is not necessarily associated with mainshock. Moreover, if dynamic triggering is the dominant triggering mechanism, one expects that similar magnitude events will have similar size of aftershock zone, due to similar dynamic stress changes. In this study, I examine the aftershock sequences up to 7 days following the mainshocks, while *Felzer and Kilb* [2009] focused on the first 2 days. Therefore, it is still possible that dynamic

triggering dominates immediately after the mainshock, while deep creep takes over after certain time. A similar argument was made by *Meng and Peng* [2014], that is, the seismicity rate in southern California after the 2012 M_w 7.2 El Mayor-Cucapah earthquake was modulated initially by dynamic stresses and later by static stress changes.

5.5 Conclusion

I conduct systematic detection of microearthquakes around 10 M>4 earthquakes near the Anza gap since 2000. With the more complete catalogs, I find significantly larger aftershock zones for earthquakes below 11-12 km at depth than the shallower ones. Such anomalous aftershock zones are most likely caused by deep creep along the SJF. However, I do not observe clear migration of aftershocks associated with the deep creep, which may due to the relative small magnitude of mainshocks and high background seismicity. Alternatively, the large aftershock zones can be explained by the lower stress drop for the deeper earthquakes. Both the deep creep and lower stress drop for deep events suggest that the SJF has a rather week part below ~12 km in depth. The seismologic observation agrees very well with the geodetically inferred model, that is, the SJF is only locked in the top 10-12 km. The lower part of the SJF does not accumulate significant amount of strain and is unlikely ruptured during the future major events near the Anza gap, which limits the maximum magnitude of the future events.

5.6 Supplementary Figures

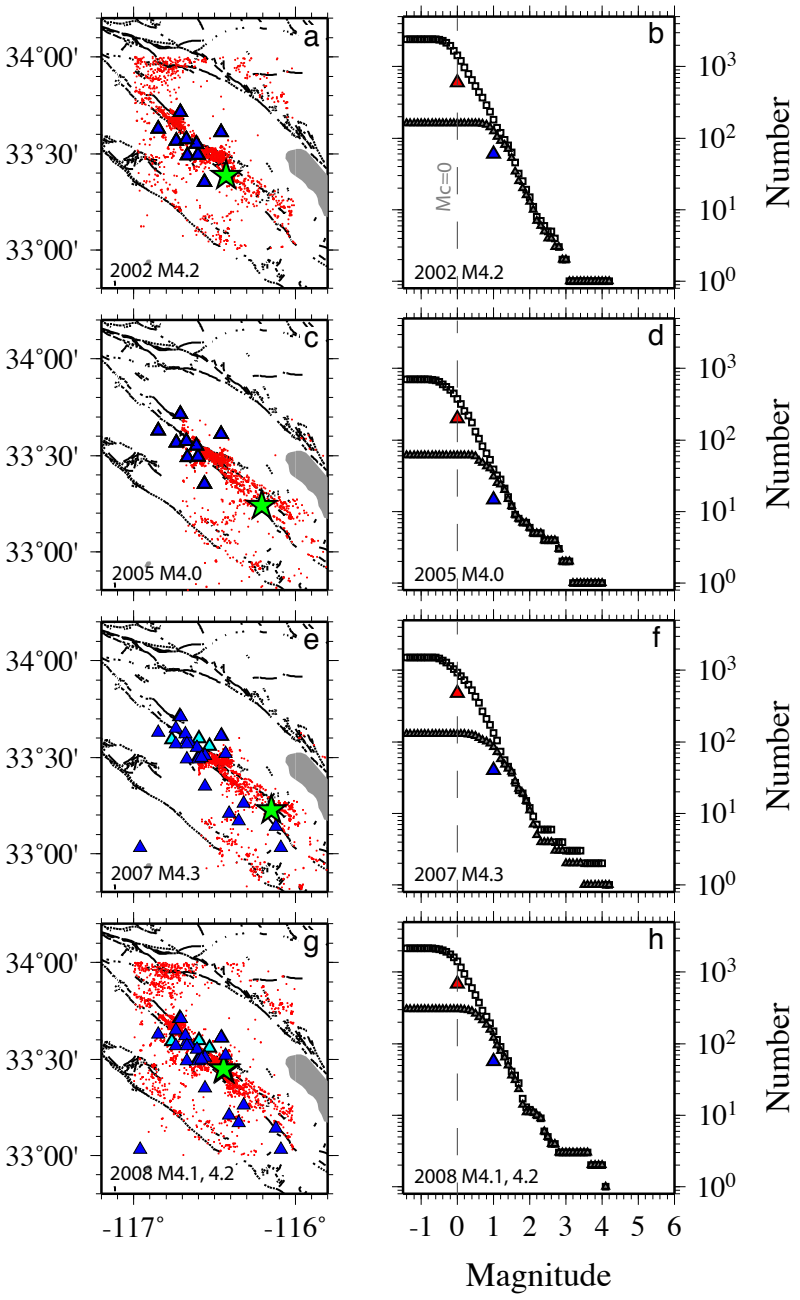

Figure S5.1 Similar with Figure 5.2 for M<4.5 events.

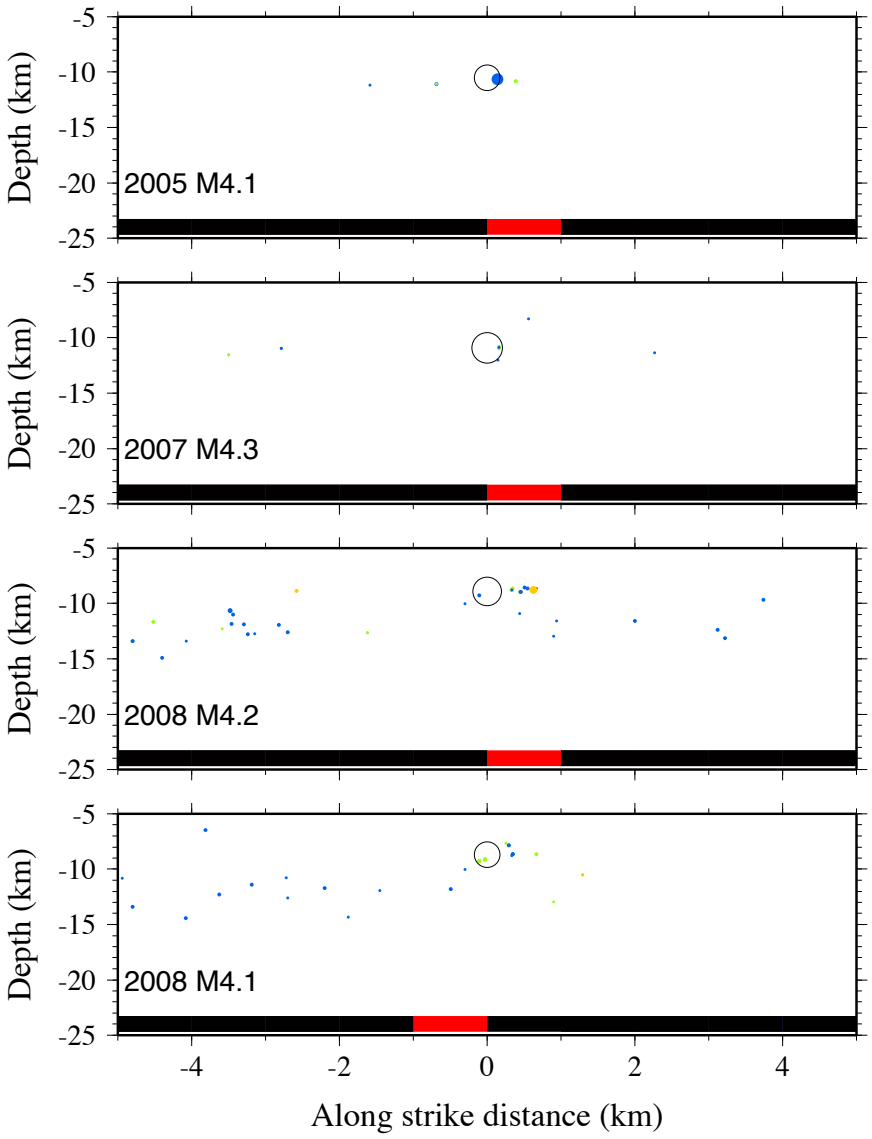

Figure S5.2 Similar plot with Figure 5.4 for 4 M<4.5 earthquakes.

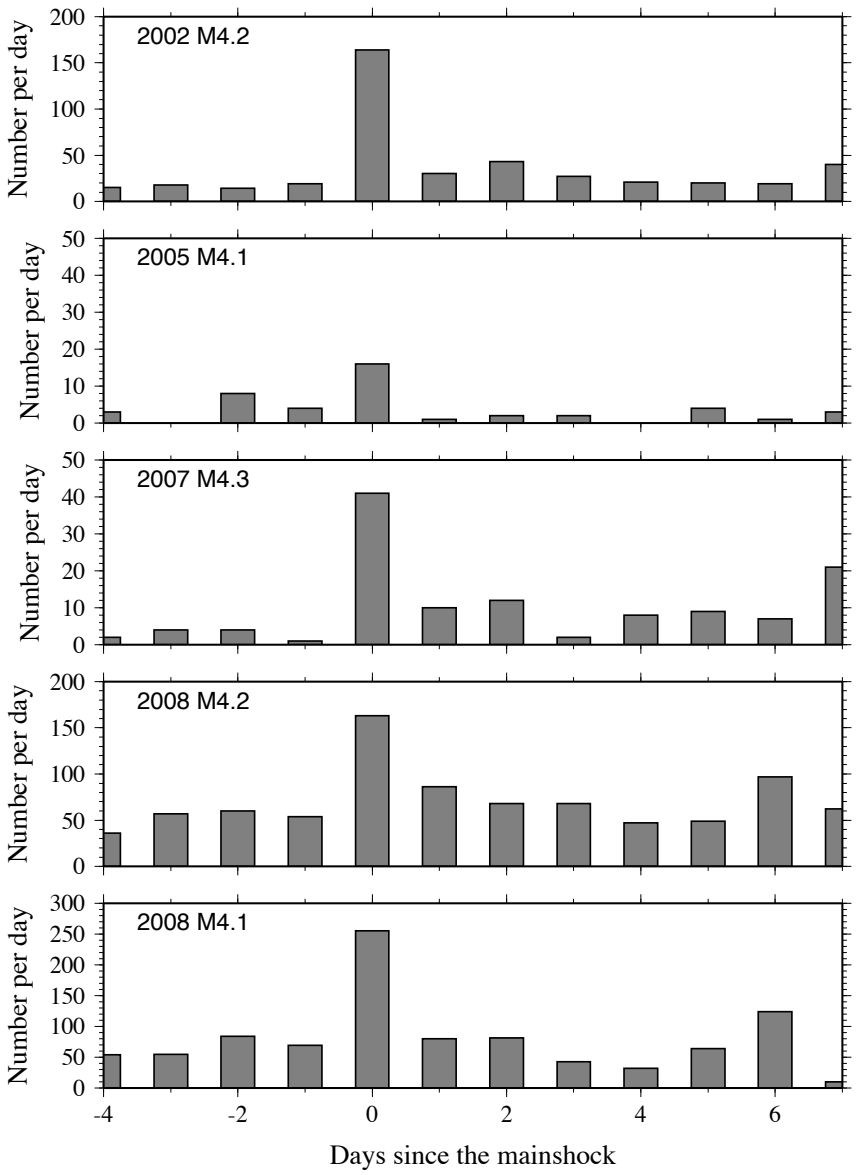

Figure S5.3 Daily seismicity rate for 5 M<4.5 earthquakes.

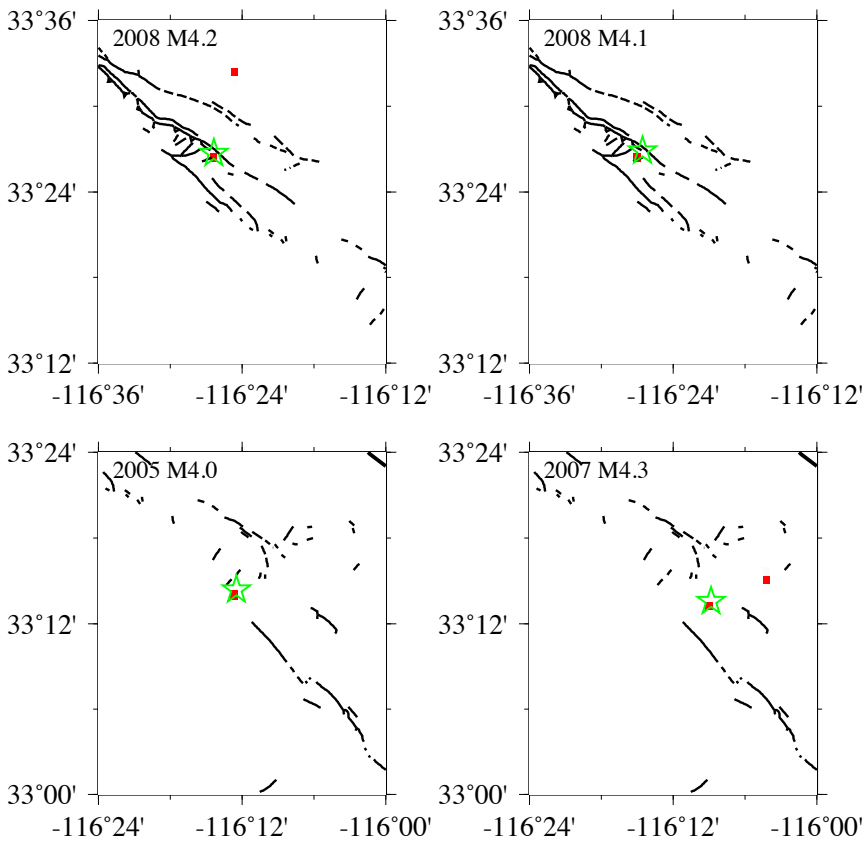

Figure S5.4 Similar plot with Figure 5.9 for 4 M<4.5 earthquakes.

CHAPTER 6

HURRICANE IRENE TRIGGERED ADDITIONAL AFTERSHOCKS OF THE 2011 M_W 5.7 VIRGINIA EARTHQUAKE

6.1 Introduction

In critically stressed (i.e., shear stress levels are very close to failure) tectonic settings such as seismic zones within intraplate regions, small stress perturbations from natural and anthropogenic processes are capable of triggering seismic events. First, many studies reported a close spatio-temporal relationship between anthropogenic activities, such as hydraulic fracturing and wastewater disposal, and the occurrence of intraplate earthquakes in central and eastern United States [*Ellsworth*, 2013 and the references therein], which are termed as induced earthquakes. Second, intraplate earthquakes closely related to hydrological cycle (e.g., rainfall during hurricane or typhoon) have also been observed worldwide [e.g., *Hainzl et al.*, 2006; *Costain and Bollinger*, 2010; *Hainzl et al.*, 2013]. For both anthropogenic and hydrological triggered earthquakes, pore-fluid pressure diffusion in subsurface are usually considered as the dominant triggering mechanism. Comparing to other triggering mechanisms, the positive cases of hydrological triggering are still too sparse to establish a causal relationship. Lastly, atmosphere pressure variations may trigger slips on critically stressed faults as well. *Liu et al.* [2009] found that the onsets of many shallow thrust slow-slip events on the Longitudinal Valley Fault in Eastern Taiwan matched well with those of atmosphere pressure decrease associated with typhoons. They hypothesized that the atmosphere pressure decrease unclamps the thrust faults and effectively increases the Coulomb

stresses on the fault plane. Although Taiwan is a typical interplate region, for the very small unclamping acting as a trigger, the faults must be critically stressed as well. *Gao et al.* [2000] illustrated an annual modulation of the triggered earthquake rate in California following the 1992 M_w 7.3 Landers earthquake. They proposed that the most likely cause for the annual modulation in such a large area is the coherent atmosphere pressure changes, which may reduce/increase the normal stress and prompt/inhibit seismicity. To my best knowledge, the aforementioned two studies are the only ones documenting the possible correlation between atmosphere pressure changes and fault slips.

For studies on earthquakes triggering in intraplate regions, the major difficulties include sparse seismic network and low background seismicity. Sharing the similar difficulties, the cases of induced earthquakes are much more abundant than triggering by hurricanes/typhoons. Unlike the continuous and small impact area of anthropogenic activities, hurricanes/typhoons impact intraplate regions in a much larger area but much shorter time period, which make it much more difficult to identify triggered earthquakes. Therefore, the rareness of triggering by hurricanes/typhoons does not necessarily reflect its genuine triggering potential. The ideal condition to study seismic events triggered by hurricanes/typhoons occurs when hurricanes/typhoons pass by densely monitored intraplate faults that is critically stressed with ample background seismicity. Fortunately, such requirements are fulfilled by the 2011 M_w 5.7 Virginia earthquake and hurricane Irene.

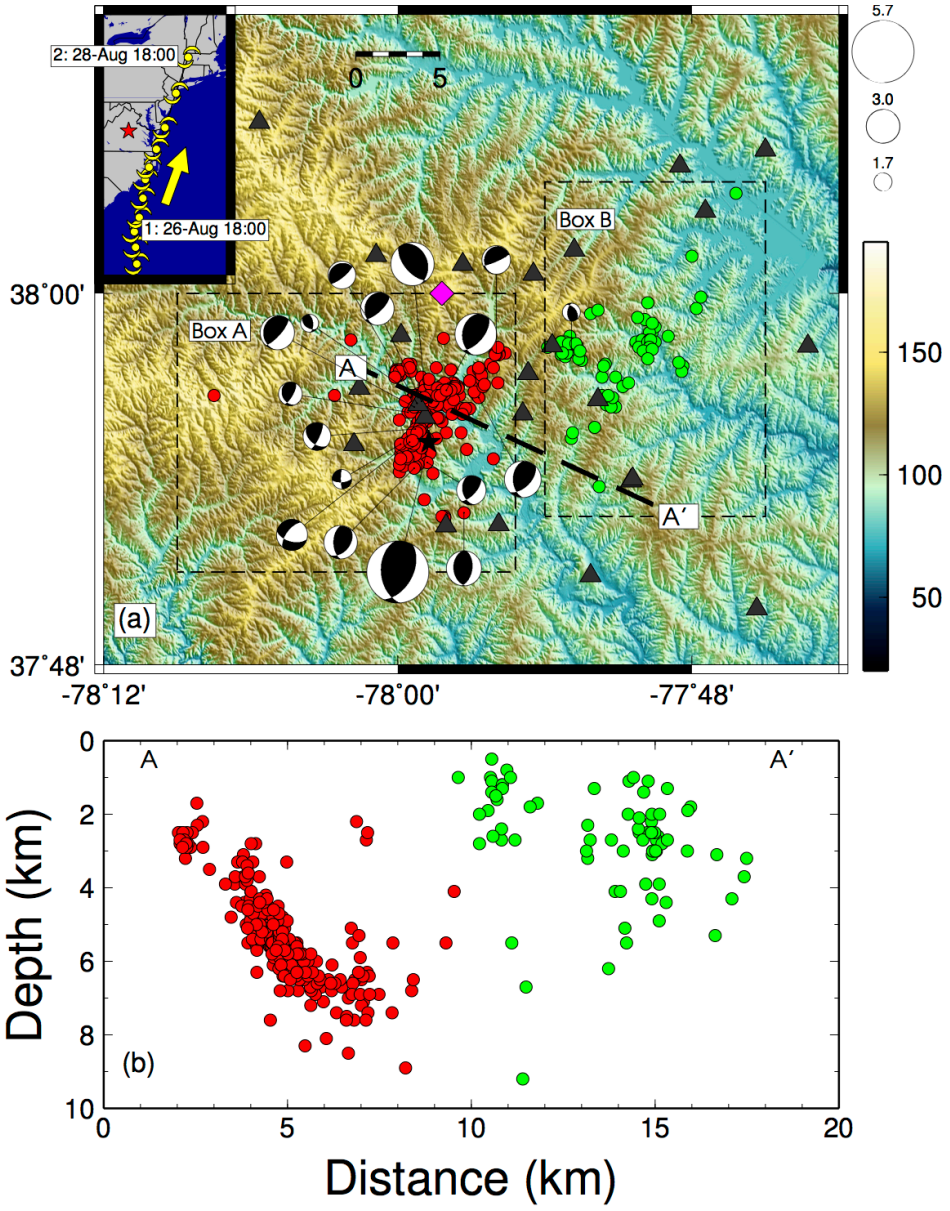

Figure 6.1 The study region and aftershock locations of the 2011 Virginia earthquake. (a) A map showing the study region around the epicenter of the Virginia mainshock (black star). The red and green dots denote the template events in Box A and B, respectively. The black triangles denote temporary seismic stations used in this study. The purple diamond denotes the NOAA station. The inset map shows the east coast of United States. The yellow symbols denote the trace of Irene's eye. The locations of Irene's eye at 26 August 2014 18:00 and 28 August 2014 18:00 are marked. (b) The cross-section view of the template events along profile AA'.

On 23 August 2011 17:51:05 UTC, an M_w 5.7 earthquake struck Louisa County, Virginia (Figure 6.1). The ground shaking caused by this earthquake was felt over most of the eastern United States. The epicenter reported by U.S. Geological Survey was at 37.905N, 77.975W, with a depth of 8.0 km. The mainshock ruptured a shallow, reverse fault striking N29E and dipping S51E in the central Virginia seismic zone (CVSZ) [*Chapman*, 2013]. The CVSZ is an active intraplate seismic zone, where several moderate-size (M~5) earthquakes occurred. Historic earthquakes in the CVSZ scattered in a west-east trending belt along the James River, which is bounded at Charlottesville on west and Richmond on east [*Bollinge*, 1973; *Kim and Chapman*, 2005]. Prior to the 2011 M_w 5.7 event, the largest event and latest moderate-size event in the CVSZ are the 23 December 1875 magnitude 4.5-5.0 and the 9 December 2003 M_w 4.3 earthquakes, respectively. The epicenters of the 2003 and the 2011 events are only ~20 km apart, and both mainshocks were recorded by only a handful of local seismic stations [*Chapman*, 2013]. The 2011 mainshock had a relative large stress drop [*Chapman*, 2013], which is typical for intraplate seismicity.

Subsequently, several dense temporary seismic networks were deployed around the rupture zone to capture the aftershock sequence (Figure 6.1) [*Chapman*, 2013; *McNamara et al.*, 2014]. Only a few days later, the destructive Irene raked the east coast of United States. Irene made its first landfall in United States at Cape Lookout, North Carolina roughly on 27 August 2011 12:00:00 (Figure 6.1). About 18 hours later, Irene made another landfall at Brigantine Island, New Jersey [*Avila and Cangialosi*, 2011]. Between the two landfalls, Irene passed by the rupture zone of the 2011 Virginia earthquake with powerful swirls of wind. The important meteorological data (e.g.,

rainfall, temperature and atmosphere pressure) is recorded by a National Oceanic and Atmospheric Administration (NOAA) station 03715/LKU ~5 km from the epicenter of the Virginia mainshock (Figure 6.1). The spatio-temporal coincidence between the 2011 Virginia earthquake and Irene, as well as rapid deployments of several seismic networks around the rupture zone, provides a unique opportunity to investigate whether the earthquake activities could be affected by hurricanes.

6.2 Data and Methods

The seismic data used in this study are downloaded from the Data Management Center (DMC) at the Incorporated Research Institutions for Seismology (IRIS). Among them, 8 temporary seismic stations were deployed around the mainshock's epicenter by teams from IRIS, USGS, the University of Memphis, Lamont Doherty Earth Observatory, and Virginia Tech about 2 to 3 days following the mainshock (network XY) (Figure 6.1a). Simultaneously, another 7 temporary seismic stations (network YC) were set up across the rupture zone subsequently from 2 to 6 days following the mainshock by IRIS RAMP deployment (Figure 6.1a). Moreover, 4 and 7 seismic stations deployed by University of Memphis (network ET) and USGS (network GS) are used in this study. Only 51 aftershocks of the 2011 Virginia earthquake prior to 1 December 2011 have been identified by the Advanced National Seismic System (ANSS) catalog. 80 early aftershocks are identified and located till 2 September 2011, using temporary network XY only (Figure 6.1a) [*Chapman*, 2013]. 380 local earthquakes are identified using 4 temporary networks (XY, YC, ET, GS) [*McNamara et al.*, 2014]. The aftershock hypocenters agree with the focal mechanism of the main. Most of the relocated events locate in the top 8 km in depth (Figure 6.1b).

Because of the existence of the temporary seismic networks and relocated local earthquakes, I apply the same technique to detect missing events in the study region. In details, I use the 380 relocated earthquakes as templates [*McNamara et al.*, 2014]. The arrival times of templates at all seismic stations are manually picked. The template waveform is set as 0.5s before to 4.5s after the *S*-wave arrival. The continuous seismic recordings are from 25 August 2011 to 1 December 2011. Since only a few permanent Virginia seismic network stations (the closest station is JSRW, ~25 km away from the epicenter) were available and no temporary seismic station was deployed in the first day after the 2011 Virginia earthquake, I cannot obtain a complete early aftershock sequence. However, the lack of the first day's aftershocks should not weaken the ability to investigate potential aftershock rate changes caused by Irene, which passed by rupture zone ~3-5 days after the mainshock (Figure 6.1a).

Both template and continuous waveforms are band-pass filtered from 2 to 8 Hz to enhance the signal to noise ratio for local earthquakes. For each template, only channels with the signal to noise ratio larger than 5 are used for detection. I compute the mean correlation coefficient (CC) between all templates and continuous recordings in a 5s time window. A local event is detected if its mean CC exceeds the sum of the median value and 9 times the MAD of the mean CC trace and recorded by at least 9 channels. I then remove all 'duplicate detections' if their detecting time windows overlap [*Meng et al.*, 2013]. The hypocenter of the detected event is assigned to be the same with that of the corresponding template event. The magnitude of the detected event is estimated from the logarithmic peak amplitude ratio between the detected event and corresponding template event [*Peng and Zhao*, 2009].

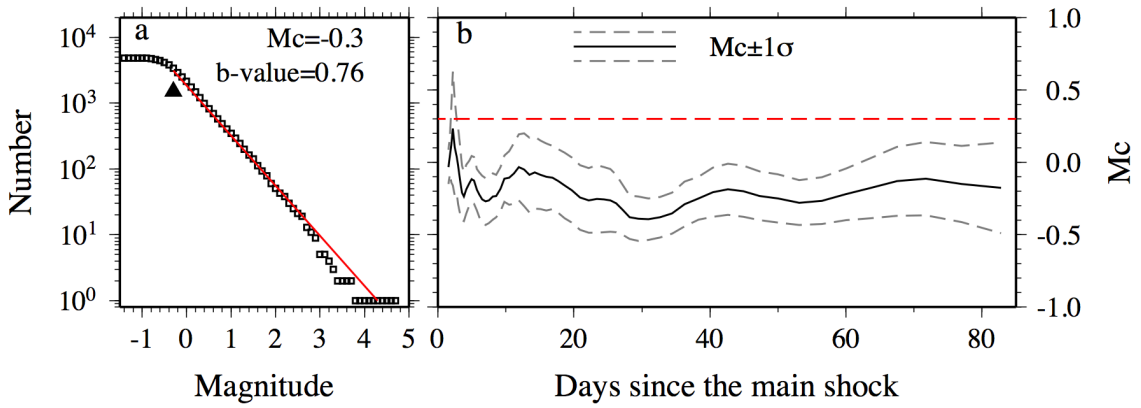

Figure 6.2 (a) The frequency-magnitude relationship of all detected aftershocks. The triangle denotes the magnitude of completeness M_c. (b) The M_c and the corresponding 1σ values versus time since the main shock. The red dashed line denotes the cutoff magnitude of 0.3 used in this study.

6.3 Results

I detect 4770 earthquakes between 25 August 2011 and 1 December 2011 (Figure 6.2 and 6.3). The magnitude of completeness (M_c) of the detected catalog is -0.3 using software ZMAP [*Wiemer*, 2001]. Due to the 'masking effect' of the mainshock and large aftershocks, I observe a relative high M_c in the beginning of the study period (Figure 6.2). Therefore, I select 0.3 as the M_c for the detected catalog. The *b*-value, which describes the relative abundance of large to small events, is 0.76 for the detected catalog. This relative small *b*-value is consistent with previous estimates for intraplate earthquakes in central and eastern United States [*Yang et al.*, 2009], suggesting a high stressing level. The detected events can be divided into two groups based on their hypocenters. Sixty per cent of events are detected by templates in Box A surrounding the mainshock rupture zone (Figure 6.1a). They depicted a southeast dipping and northeast striking plane that agrees well with the reverse-faulting mechanism of the mainshock (Figure 6.1b). Ten of

sixteen events in Box A with reliable focal mechanism solutions are associated with reverse faulting [*McNamara et al.*, 2014] (Figure 6.1a). Overall the seismicity rate change in Box A is well fitted by the Omori's law with p=1 [*Omori*, 1894; *Ogata*, 1988] (Figure 6.4a), suggesting a typical aftershock sequence. The aftershock rate shows one clear deviation from the Omori's law prediction at the beginning of the study period (Figure 6.3b). An M4.7 aftershock, the largest one during the study period, immediately preceded the peak, suggesting that the peak is most likely caused by secondary aftershocks of the M4.7 event. During the remaining study period, the aftershock rate shows little fluctuation comparing with the best-fitting Omori's law (Figure 6.3b).

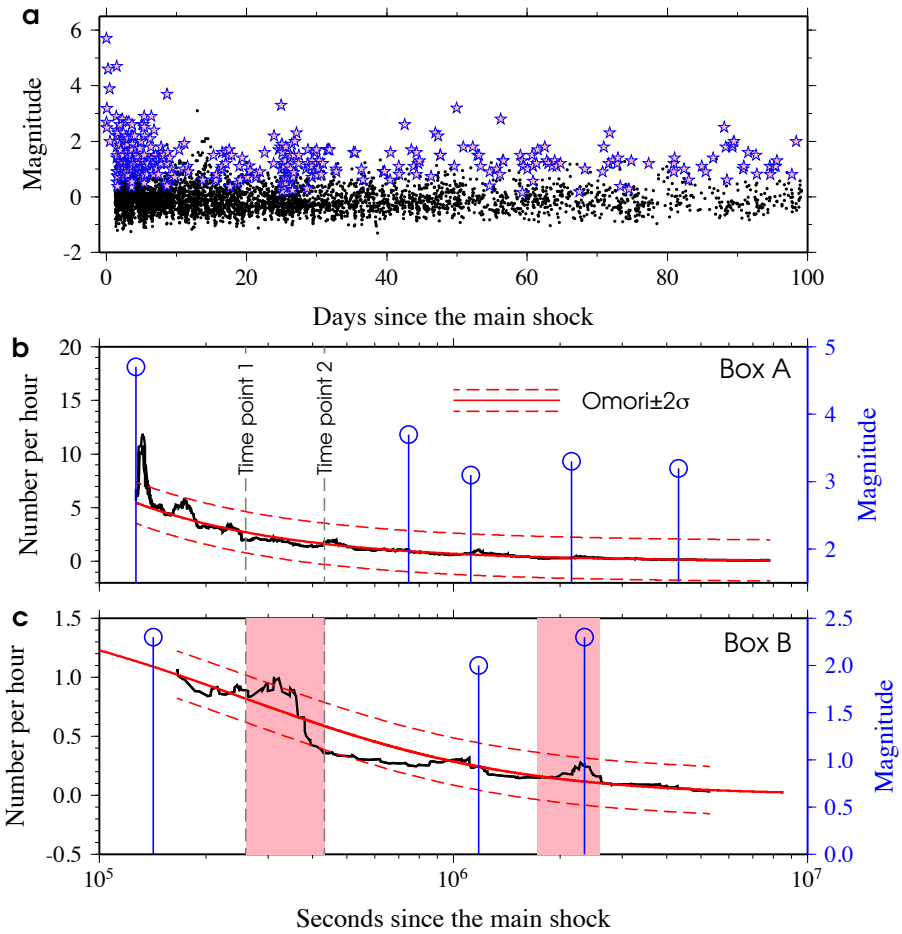

Figure 6.3 Temporal distributions of aftershocks. (a) The magnitude of templates (stars) and newly detected events (dots) versus time. (b) The smoothed seismicity rate with M>0.3 versus logarithmic time since the mainshock in Box A. The red solid and dashed lines denote the best-fitting Omori's law and two standard deviations. The blue circles denote events with M>3 in Box A. The grey dashed lines denote the two time points marked in Fig. 1 when Irene passed by the Virginia epicenter. (c) The same plot as (b) for Box B. The shaded areas denote the two periods of rate increase.

In contrast, events in Box B are more scattered at shallower depth (i.e., <5 km), and are well separated from the rupture plane of the mainshock. They are not associated with any known fault and do not show clear lineation (Figure 6.1b) [*McNamara et al.*, 2014]. The seismicity rate in Box B also shows a general Omori's decay pattern with a higher decay rate (i.e., p=1.3) than that of Box A (Figure 6.4b). Hence, instead of aftershocks, most detected events in Box B can be considered as events triggered by stress transfer of the mainshock onto nearby unknown faults.

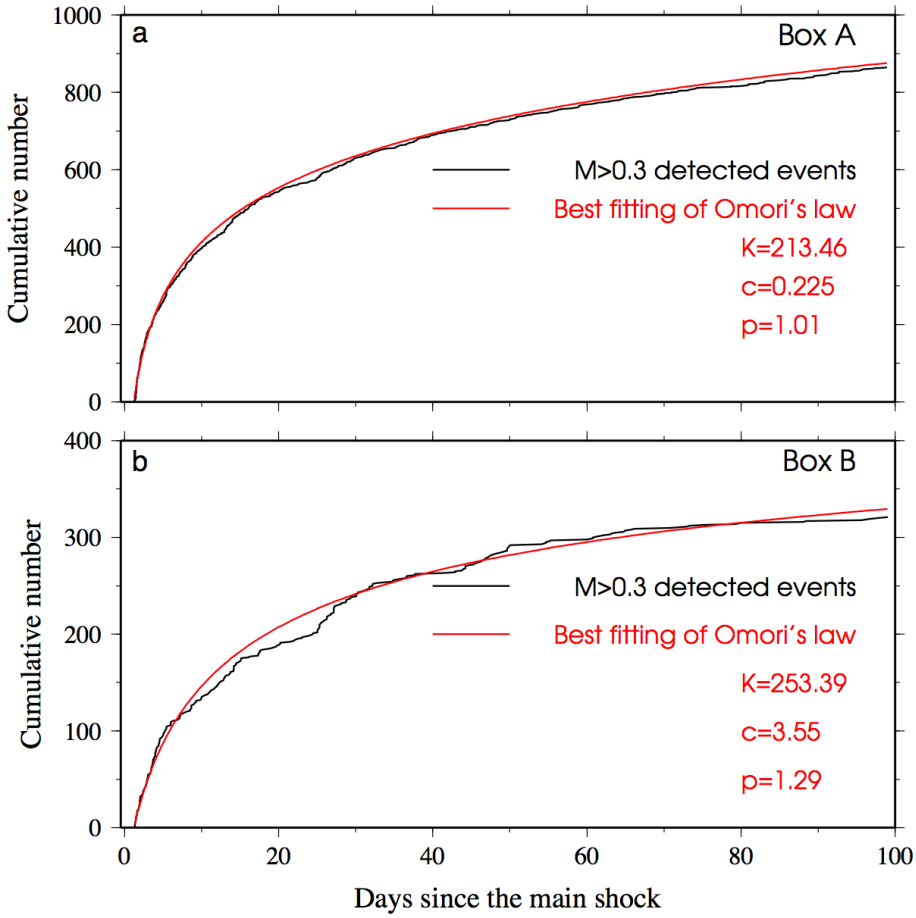

Figure 6.4 (a) and (b) The cumulative number of detected events with M>0.3 (black) and the best-fitting Omori's law (red) versus time since the mainshock in Box A and B, respectively.

I observe two time periods when the seismicity rate in Box B clearly deviated from the best-fitting Omori's law (Figure 6.3b). Since there is no earthquake with M>2 immediately preceding both time periods, the rate increases are not likely caused by secondary aftershocks. A close examination reveals that the seismicity in these two time periods behaves like swarm activities (Figure 6.5). That is, the largest-magnitude event did not occur at the beginning of a sequence, and the magnitude differences with other events are small [*Mogi*, 1962]. Recent studies have used the Epidemic Type Aftershock

Sequence (ETAS) model, which based on empirical relationships for earthquake clustering, to detect earthquake swarms [*Ogata*, 1988; *Llenos et al.*, 2009]. In the ETAS model, the seismicity rate at time *t* is described as

$$R(t) = \mu + \sum_{t_i \le t} \frac{K e^{\alpha(M_i - M_c)}}{(t - t_i + c)^p} \quad (6.1)$$

where μ is the background seismicity rate, *c* and *p* are Omori's law parameters, *K* is the aftershock productivity, α reflects how efficient a certain magnitude earthquake generates aftershocks, t_i is the origin time of the *i*th earthquake. The optimal parameters can be obtained by maximum likelihood estimation using software SASeis2006 [*Ogata*, 2006]. Then, I investigate the relationship between the cumulative observed number and theoretical number of events (i.e., transformed time τ_i) [*Ogata*, 1988; *Llenos et al.*, 2009]. The transformed time is calculated as:

$$\tau_i = \int_0^{t_i} R(s) ds \quad (6.2)$$

where *R* is the predicted seismicity rate by the ETAS model, t_i is the origin time of the *i*th event in the catalog. When a catalog can be well described by the ETAS model, the actual number should equal to the theoretical number of events.

The aftershock sequence in Box A can be well-fitted by the ETAS model during the whole study period (Figure 6.6a). In contrast, the sequence in Box B deviates significantly from the ETAS prediction (Figure 6.6b), suggesting that the sequence in Box B is not a typical aftershock sequence. Then, I apply the ETAS model to shorter time windows around the two periods of seismicity rate increase. First, I fit the events in Box B between 1.5 to 23 days after the mainshock, which is from the start of the temporary stations till the second period of seismicity rate increase (Figure 6.6c). I select this relative long time window to include as many events as possible for a stable fitting. A

significant deviation from the ETAS prediction occurs at ~3 days after the mainshock. This deviation indicates that the first period of seismicity rate increase is most likely due to a swarm sequence, which is not well fitted by the ETAS modeling [*Ogata*, 1988; *Llenos et al.*, 2009]. Similarly, I fit the events in Box between 16 days after the mainshock and right before the second period of seismicity rate increase (i.e., 25 days) and extrapolate it to the end of the second period of seismicity rate increase (i.e., 30 days) (Figure 6.6d). I also observe a clear deviation from the ETAS prediction, suggesting another swarm. The first swarm (i.e., 3-5 days after the main shock) in Box B overlaps the time window when Irene passed by the main shock rupture zone, suggesting a possible causal relationship.

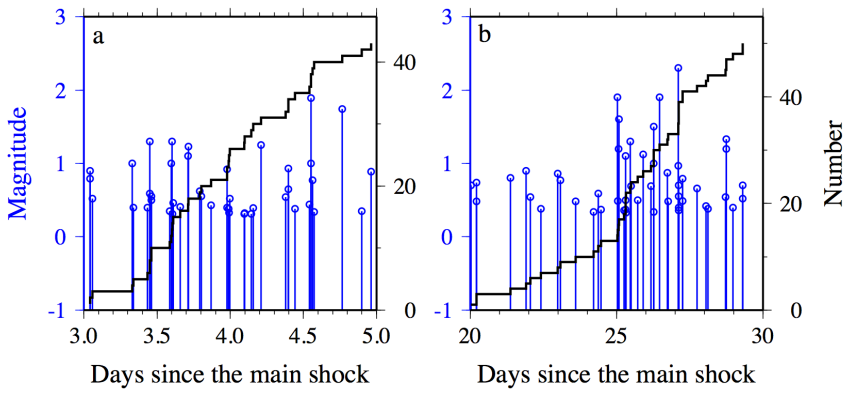

Figure 6.5 The zoom-in time windows of the two periods of seismicity rate increase (2-6 days and 20-30 days following the main shock) in Box B.

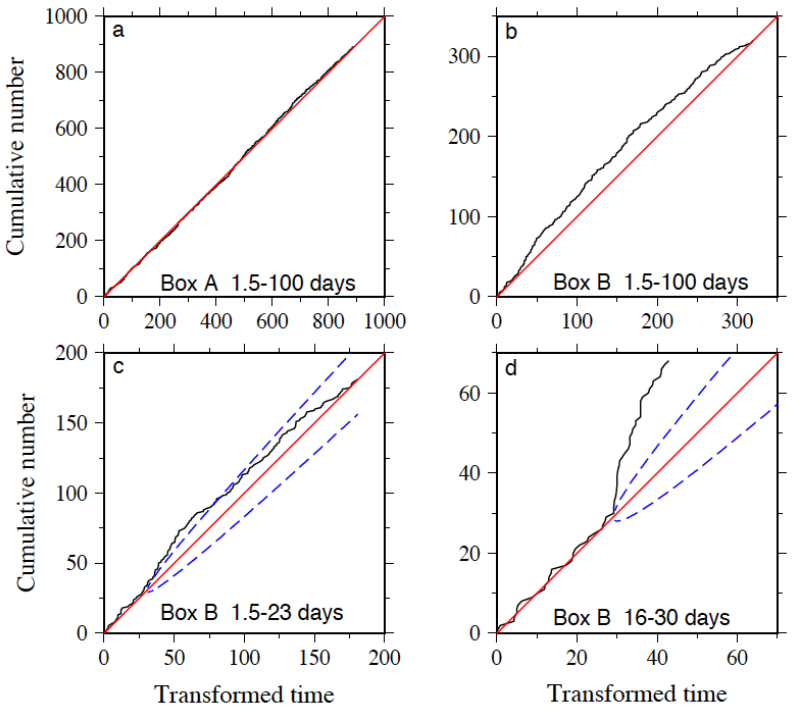

Figure 6.6 The ETAS modeling. The black curve denotes the actual data. The red line denotes the ETAS prediction. The blue dashed lines denote 2σ.

Next, I examine the impacts of major meteorological forces on the seismicity rate changes in Box B. There was a clear atmospheric pressure drop associated with Irene, whose peak amplitude is ~2 kPa. The pressure drop started ~3 days after the Virginia mainshock (i.e., time point 1 in Figure 6.1a) and returned to pre-hurricane level ~5 days after the mainshock (i.e., time point 2 in Figure 6.1a). The onset and duration of atmosphere pressure drop matches that of the first swarm in Box B (Figure 6.7b). In Box B, only one event has a reliable focal mechanism solution, which is also reverse faulting (Figure 6.1a). Assuming the majority of events in Box B are also reverse faulting, the seismicity rate increase during hurricane Irene can be qualitatively explained by the atmospheric pressure drop unclamping the fault (Figure 6.7a). However, the seismicity rate increase initiated when the atmospheric pressure drop was minimal, which may be

too small to trigger earthquakes even on critically stressed faults. Interestingly, a similar phenomenon is observed in Taiwan, where some SSEs initiated when the atmospheric pressure only started to decrease [*Liu et al.*, 2009]. It leads me to suspect that the stress rate, instead of stress, is the controlling factor on triggering earthquakes in this case. In the rate- and state-dependent friction model for earthquake triggering, stress steps cause aftershock-like sequences, while stress rate changes cause earthquake swarms [*Dieterich*, 1994; *Toda et al.*, 2002], which is consistent with the observation of swarm activity during Irene.

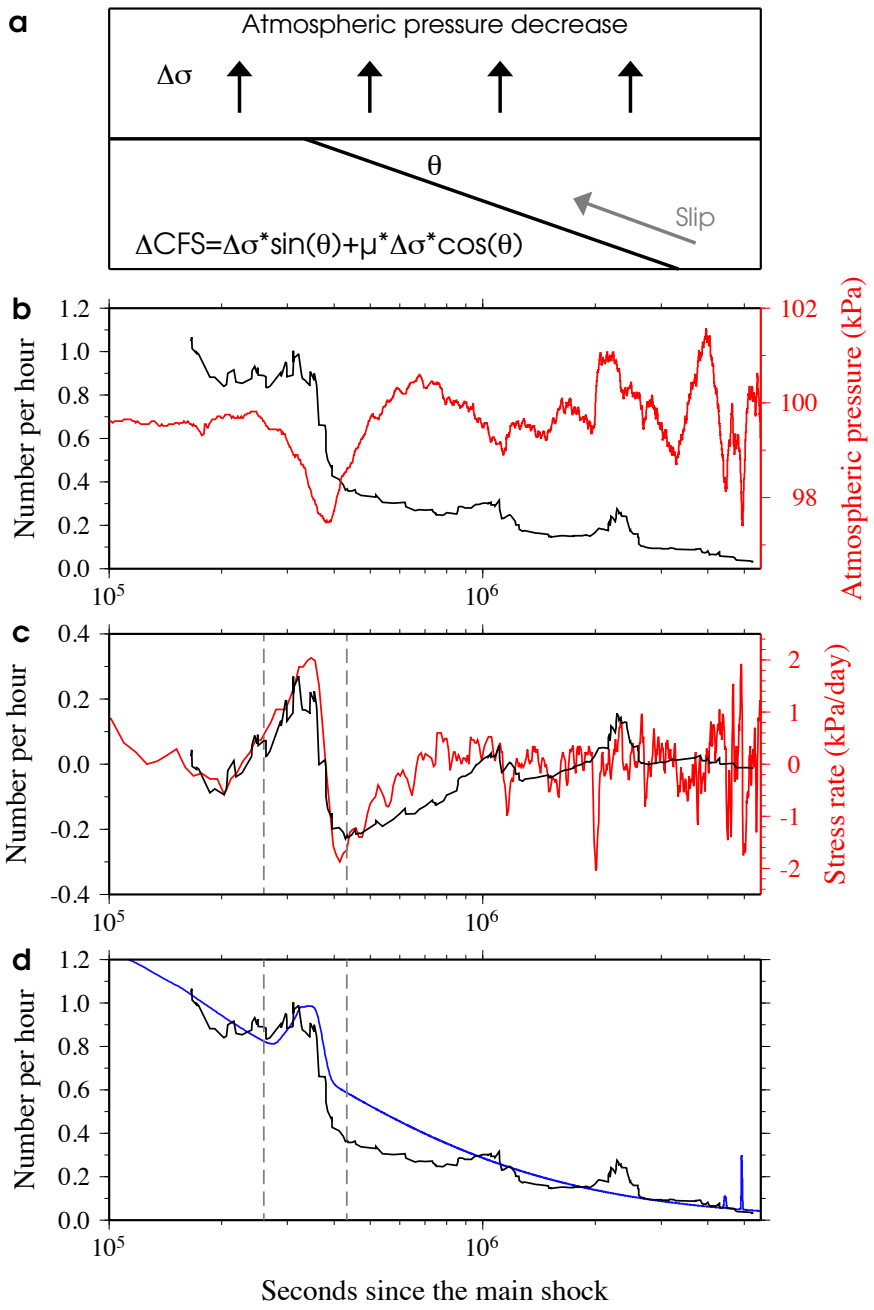

Figure 6.7 A schematic diagram and observed versus predicted aftershock rates. (a) The cartoon illustrates how the atmosphere pressure decrease promotes reverse faulting. $\Delta\sigma$ denotes the atmospheric pressure change. θ denotes the dip angle. (b) The comparison between the atmospheric pressure chronogram (red) and the smoothed seismicity rate in Box B (black). (c) The comparison between the smoothed Coulomb stress rate chronogram (red) and the seismicity rate differences between the smoothed rate changes and its best-fitting Omori's law (black). (d) The blue curve denotes the sum of the predicted seismicity rate fluctuations from stress rate history in (c) assuming $r = 2.4/yr$,

$A\sigma = 0.1\ kPa$ and $\dot{S_r} = 0.73\ kPa/yr$ and the best-fitting Omori's law. The black curve denotes the actual seismicity rate changes in Box B.

I compute the Coulomb stress rate changes from the atmospheric pressure changes resolved on the sole focal mechanism in Box B and compare it with the seismicity rate changes in Box B (Figure 6.7c). To remove the general decay trend of the seismicity rate, I subtract the smoothed seismicity rate by its best-fitting Omori's law decay. It is evident that the seismicity rate fluctuations generally follow the Coulomb stress rate changes with little delay during Irene's pass-by (Figure 6.7c).

Next, I predict the seismicity rate fluctuations from the Coulomb stress rate by the rate- and state-dependent friction model and add such fluctuations to the best-fitting Omori's law. I predict the seismicity rate from the stress rate using following equations:

$$R = \frac{r}{\gamma \dot{S_r}} \tag{6.3}$$

$$d\gamma = \frac{dt}{A\sigma}(1 - \gamma \dot{S}) \tag{6.4}$$

where r and $\dot{S_r}$ are constant background seismicity and Coulomb stress rate, respectively. R and $\dot{S}$ are time dependent seismicity and Coulomb stress rate, respectively. γ is state variable, A is a fault constitutive parameter, and σ is the constant normal stress. The time step dt is 0.01 day in the computation. Assuming the fault constitutive parameter $A\sigma = 0.1\ kPa$ and background stress rate $\dot{S_r} = 0.73\ kPa/yr$, the predicted seismicity rate fit well with the observed rate increase during Irene (Figure 6.7d). The parameters are consistent with the optimal parameters obtained from rainfall-induced seismicity in another intraplate region at Mt. Hochstaufen, Germany (i.e., $A\sigma = 0.15\ kPa$ and $\dot{S_r} = 0.85\ kPa/yr$) [*Hainzl et al.*, 2013]. Although the rate- and state-dependent model

accurately predicts the seismicity rate increase during Irene, there are clear misfits afterwards. First, the clear decrease of the seismicity rate following the first swarm is not predicted. Second, although the second swarm also occurs when the Coulomb stress rate increases (Figure 6.7b), the rate- and state-dependent friction model does not predict any seismicity rate change due to the much lower amplitude (Figure 6.7c). Third, there were clear atmospheric pressure drop following the second swarm (Figure 6.8). The rate- and state-dependent friction model predicts another two seismicity rate peaks, but no visible change is shown in the smoothed seismicity rate (Figure 6.7c). The lack of response in seismicity rate could be explained by that the previous two swarms have relieved the majority of cumulated stress on reverse faults in Box B, hence similar atmospheric pressure decrease at later times can not trigger significant seismicity rate anymore; or the background seismicity rate became too low to reflect clear change comparing to earlier times.

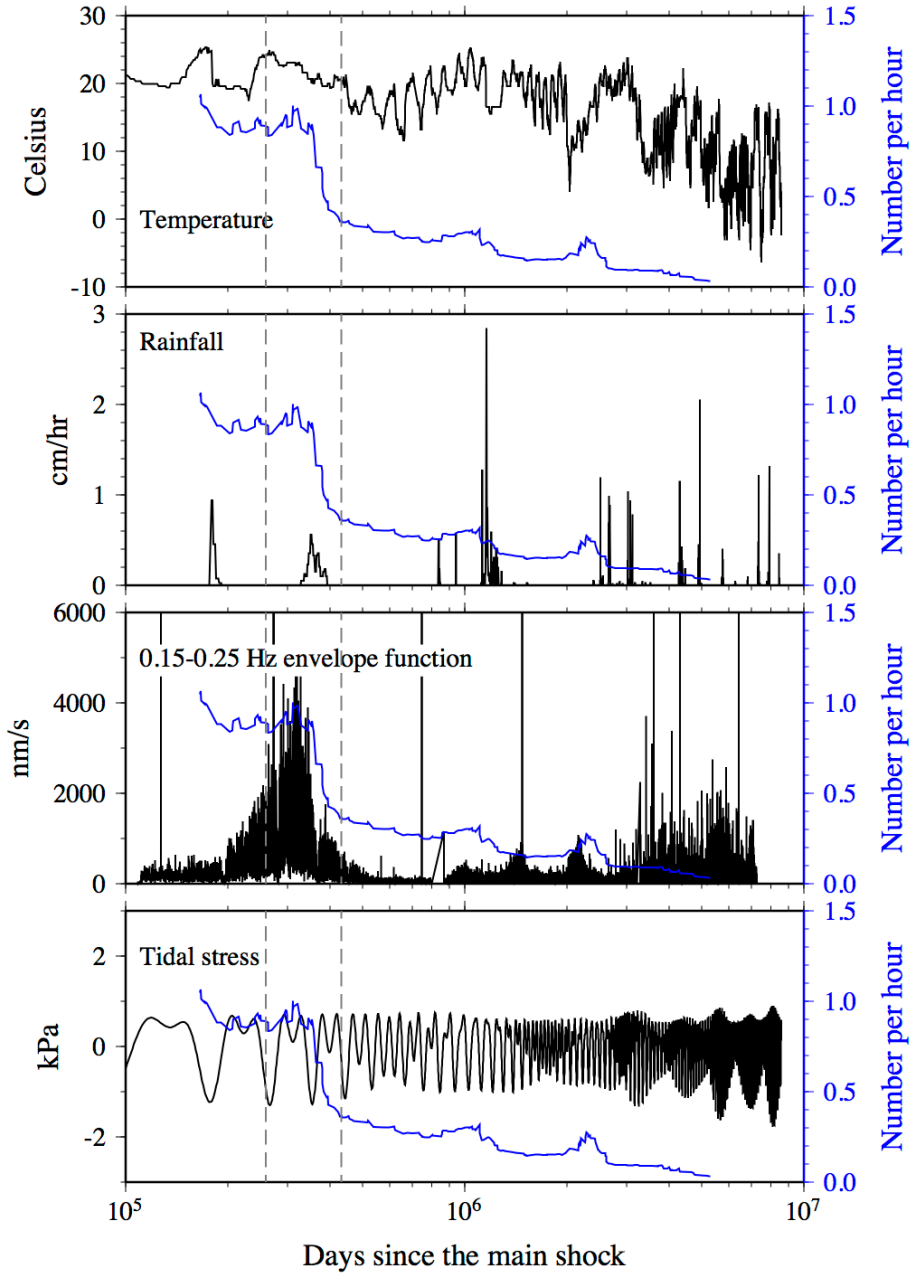

Figure 6.8 The comparison between the seismicity rate changes in Box B and other external forces, including temperature, rainfall, microseism amplitude and tidal stress.

6.4 Alternative Explanations

I also investigate and rule out possibilities of other triggering mechanisms (e.g., rainfall, temperature variation, solid earth tide, static and dynamic stress changes) being the primary causes on the seismicity rate changes in Box B.

6.4.1 Rainfall and Temperature Variation

During Irene's pass-by, only a small amount of rainfall was recorded (Figure 6.8). More importantly, for rainfall to act as a trigger, it usually takes a certain amount of time (e.g., few days to months) for water to diffuse into seismogenic depth [*Hainzl et al.*, 2013]. Hence, the small amount of rainfall during Irene should not be a primary factor for triggering seismicity in this case. Similarly, the temperature changes during Irene are negligible and so are the resultant thermal strain changes [*Ben-Zion and Leary*, 1986].

6.4.2 Static Coulomb Stress Changes

I calculate the static Coulomb stress changes from a finite slip model (http://www.geol.ucsb.edu/faculty/ji/big_earthquakes/2011/08/23/virginia.html). Since I do not know any fault geometry in Box B, I use the mainshock's fault geometry and the sole reliable focal mechanism in Box B as the receiver fault, respectively (Figure 6.9). The effective coefficient of friction is set to 0.4. When computed at 1 km depth, the static Coulomb stress increased in Box B for both receiver fault geometries. When computed at 5 km in depth, Box B lies on the boundary of positive and negative static stress changes in both cases. Therefore, the majority of events in Box B are in area where Coulomb stress increased. However, such stress step can best explain the overall activation of seismicity in Box B, instead of the swarm-like sequence during Irene's pass-by [*Dieterich*, 1994; *Toda et al.*, 2002].

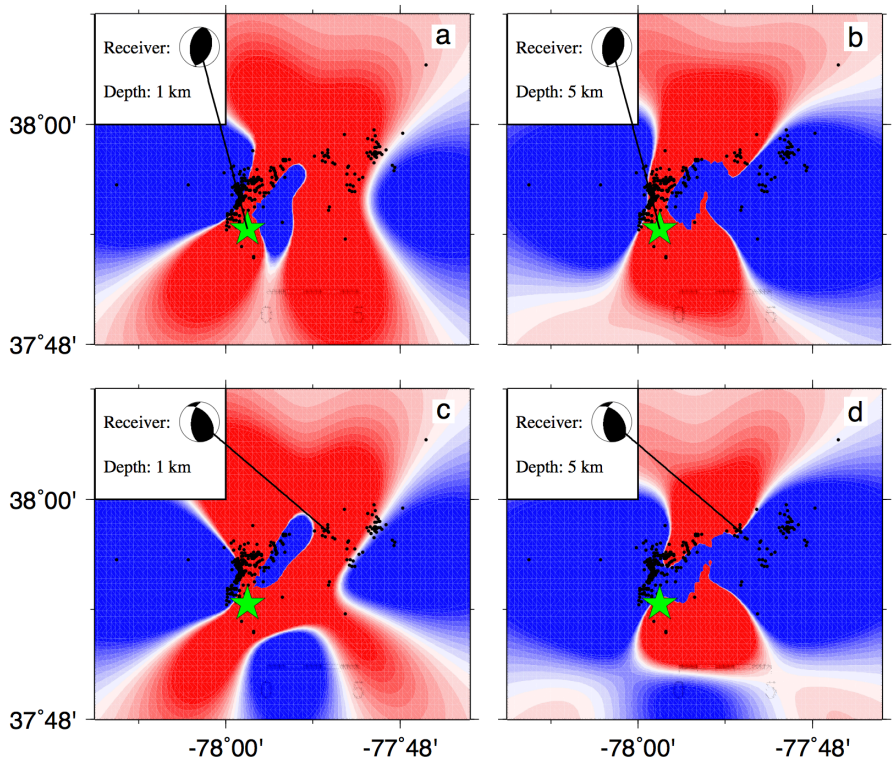

Figure 6.9 The static Coulomb stress changes caused by the Virginia earthquake resolved on different focal mechanisms and depths. The green star denotes the epicenter of the main shock. The black dots denote the template events.

6.4.3 Dynamic Stress Changes

I compute the empirical dynamic stress changes following global earthquakes with M>5 using the standard magnitude and 20s surface wave relationship (Figure 6.10). I do not find any global earthquake with dynamic stress changes larger than 0.1 kPa immediately before the first swarm. Although I observe a M6.7 aftershock of the 2011 great Tohoku-Oki earthquake occurred ~1 day prior to the second swarm, I did not observe any instantaneous triggering during the surface wave of the M6.7 event. This is mostly because the dynamic stress changes are only ~80 Pa, which is a few orders smaller than dynamic triggering threshold (i.e., a few kPa) identified in other studies [*Hill and Prejean*, 2007]. Moreover, global events that caused larger dynamic stress changes at

other times were not associated with any obvious seismicity rate changes. Similarly, although the seismic signal associated with hurricane (filtered in 0.15-0.25 Hz) shows good temporal correlation with the seismicity rate increase during Irene's pass-by (Figure 6.8), its peak amplitude (i.e., 4 μm/s) and resultant dynamic stress changes (i.e., 30 Pa) are too small to trigger earthquakes.

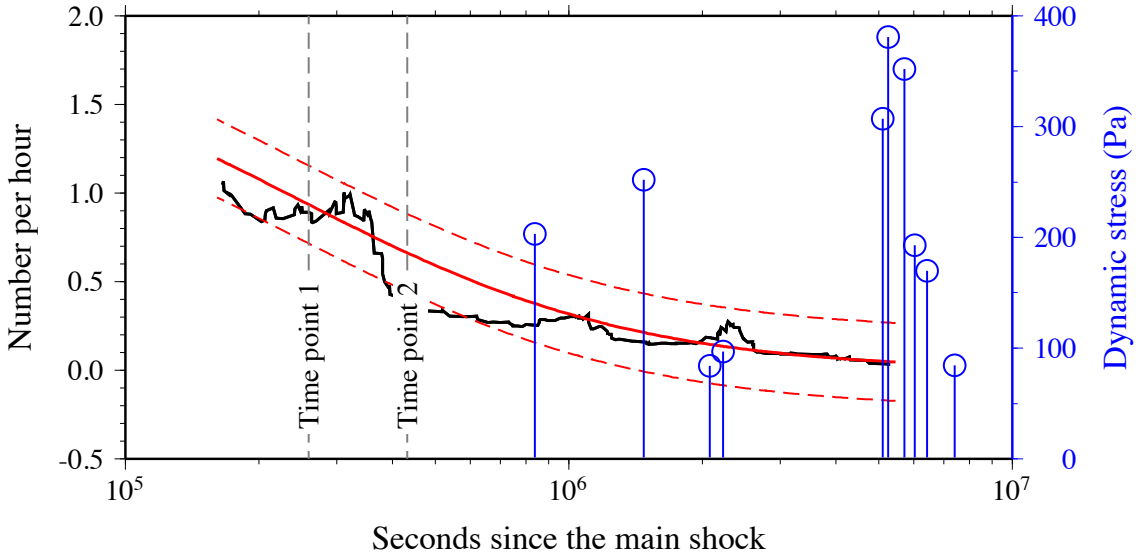

Figure 6.10 The black curve denotes the smoothed seismicity rate versus time since the main shock in Box B. The blue circles denote the dynamic stress changes caused by large distant earthquakes with M>5.

6.4.4 Earth Tide

Previous studies on tidal triggering mainly rely on the Schuster test [*Cochran et al.*, 2004; *Tanaka et al.*, 2004], which computes the probability to reject the null hypothesis that a catalog does not correlate with the perturbation of a certain period. Recently, it is suggested that the Schuster test on a single periodicity can be misleading, instead one should compute the Schuster probability (i.e., *p*-value) in a wide range of periodicities (i.e., Schuster spectrum) [*Ader and Avouac*, 2013], which can assert the

existence of certain period in the catalog and reveal unexpected periodicity. I then compute the Schuster spectrums for seismicity in Box A and B respectively (Figure 6.11). The Schuster spectrum of Box A is typical for an aftershock sequence. That is, the *p*-values decay with periodicity and many large periodicities have *p*-values beyond 99% confidence level [*Ader and Avouac*, 2013]. However, those extremely small *p*-values are artifacts and do not represent genuine periodicities [*Ader and Avouac*, 2013]. In Box B, although the seismicity rate also follows a general decay pattern, the Schuster spectrum is totally different from that of Box A. I observe a very low *p*-value beyond 95% confidence level at 0.5 day, which is consistent with the semidiurnal tidal stress fluctuations. However, I also observe two periodicities that have even smaller *p*-value that are not related to any tidal stress periodicity. Therefore, events in Box B might be weakly modulated by the semidiurnal tidal stress variation, but the signals are contaminated by the general decay pattern of the seismicity rate.

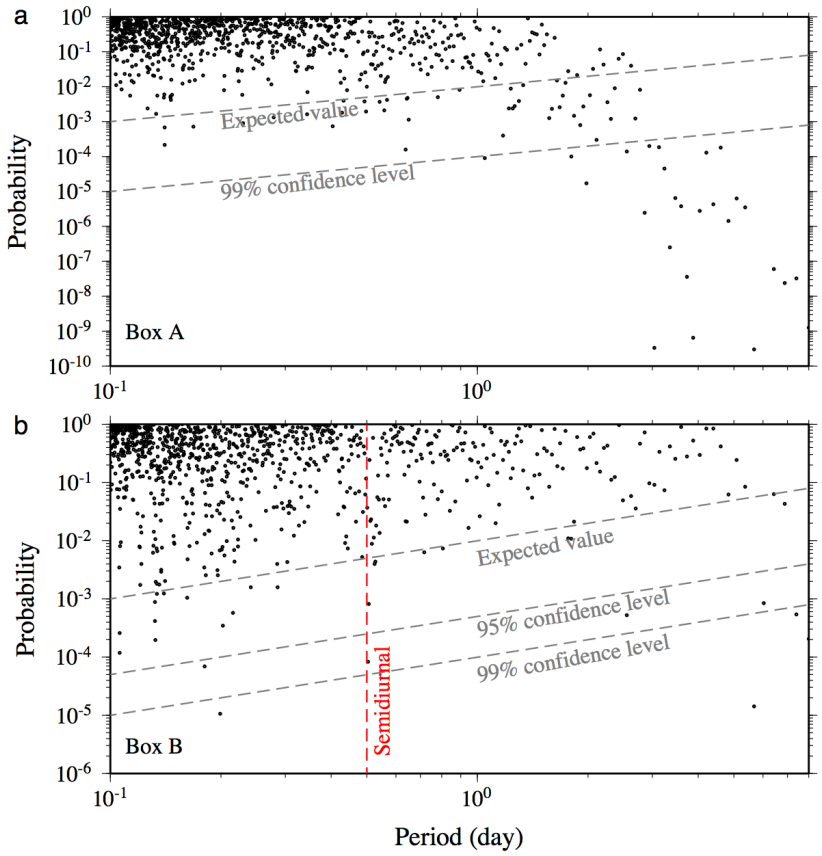

Figure 6.11 (a) and (b) The Schuster spectrums of the detected events in Box A and B, respectively.

6.4.5 Random Fluctuations

Next, I evaluate whether the seismicity rate increase in Box B during Irene's pass-by could be simply random fluctuations. I apply the same analysis procedure to 6 earthquake sequences with the mainshocks' magnitude between 5.5 and 6 in California and Japan from 2000 to 2012 based on following criterions: 1) the magnitude of the mainshock (i.e., the largest event during the sequence) is between 5.5 and 6 so that they are similar to the magnitude of the Virginia event; 2) the mainshock's hypocenter is shallow (i.e., <15 km); 3) at least 300 aftershocks were listed in the local catalog. In total, 6 earthquake sequences are used for further analysis. Earthquakes occurred within 20 km

from the mainshock and between 1 to 100 days following the mainshock are used for further analysis, which are consistent with the spatial and temporal windows for the 2011 Virginia sequence analysis. I use the Northern California Seismic Network (NCSN) catalog and a relocated catalog in southern California [*Hauksson et al.*, 2012] for sequences in California, and Japan Meteorological Agency (JMA) catalog for sequences in Japan. Next, I compute the time varying M_c using software ZMAP [*Wiemer*, 2001]. The smoothed aftershock rate is calculated in a 20-event sliding window [*Peng et al.*, 2007] with events above M_c. I then fit the aftershock rate with the Omori's law using software aftpoi [*Ogata*, 1988]. When a clear deviation from the best-fitting Omori's law appears, I examine whether it is a secondary aftershock sequence. Finally, I apply the ETAS model to all sequences from 1.5 to 100 days after the main shock (Figure S6.1-S6.6). It appears that clear deviations from the Omori's law are always preceded by relative large aftershocks and therefore most likely secondary aftershock-sequences. Although such analysis cannot completely dispute the possibility of random fluctuations, it suggests that the swarm-like increase of seismicity rate is uncommon during an aftershock sequence for moderate-size main shocks.

6.5 Conclusion

In summary, I find the off-fault seismicity increased significantly when hurricane Irene approached the aftershock zone of the 2011 Virginia mainshock. The onset and duration of the seismicity rate increase are consistent with that of the atmospheric pressure decrease. I suggest that the atmospheric pressure decrease might unclamp and prompt additional failures on critically stressed reverse faults. The swarm-like behavior is consistent with the rate- and state-dependent modeling that increasing stress rate governs

the seismicity changes in this study. Whether major meteorological forces can trigger seismicity is still poorly understood, mainly due to poor instrumentations and lack of good case studies. This work documents a likely triggering case by atmospheric pressure decrease in an intraplate region. Although I only present a single case study here, the observations shed new insight on how extreme weather events may impact local seismicity, which helps understand the fundamental physics of earthquake triggering, and links between atmospheric and lithospheric processes.

6.6 Supplementary Figures

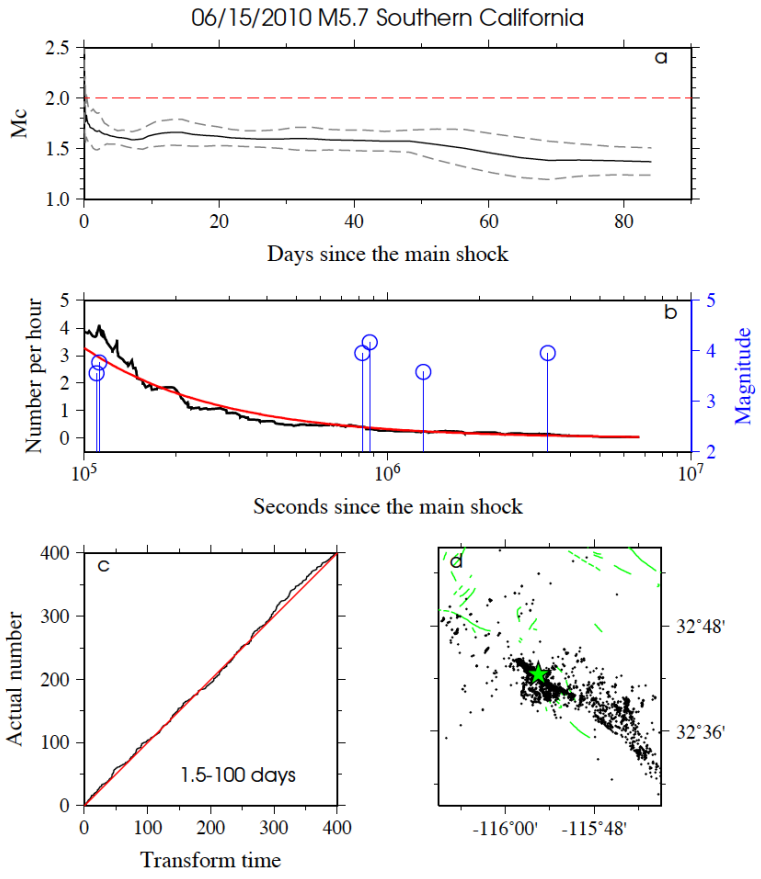

Figure S6.1 The aftershock sequence of the 06/15/2010 M5.7 Southern California earthquake. (a) M_c versus time. The grey dashed lines are two times standard deviation. The red dashed line denotes the M_c used in further analysis. (b) The smoothed seismicity rate (black) and its best-fitting Omori's law (red). The blue circles denote large

aftershocks. (c) The ETAS modeling. (d) The map showing the sequence. The green star denotes the main shock. The green lines denote fault traces.

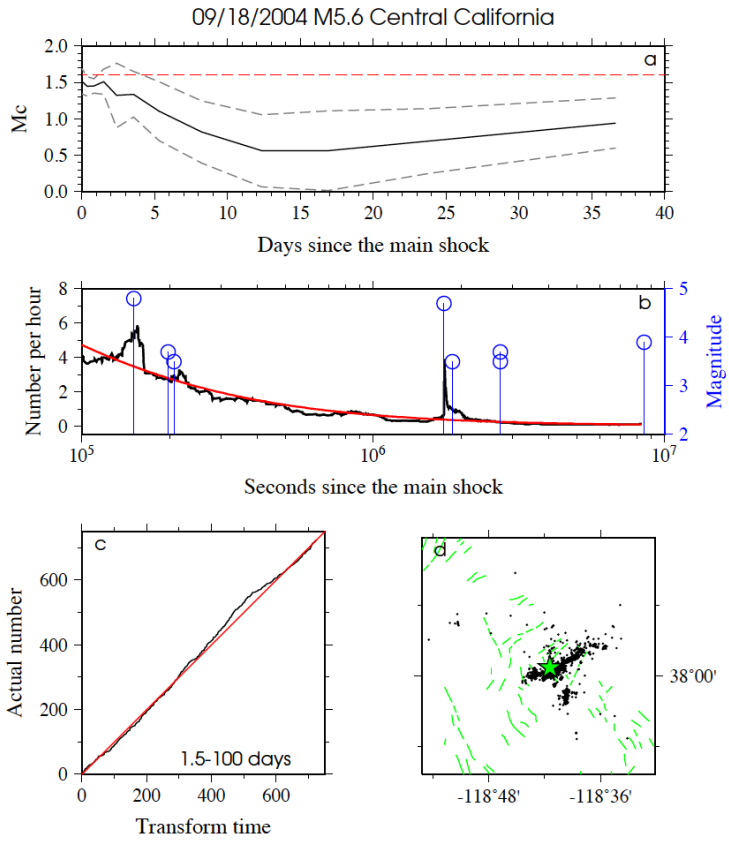

Figure S6.2 The aftershock sequence of the 09/18/2004 M5.6 Central California earthquake. All the denotations are the same as Figure S6.1.

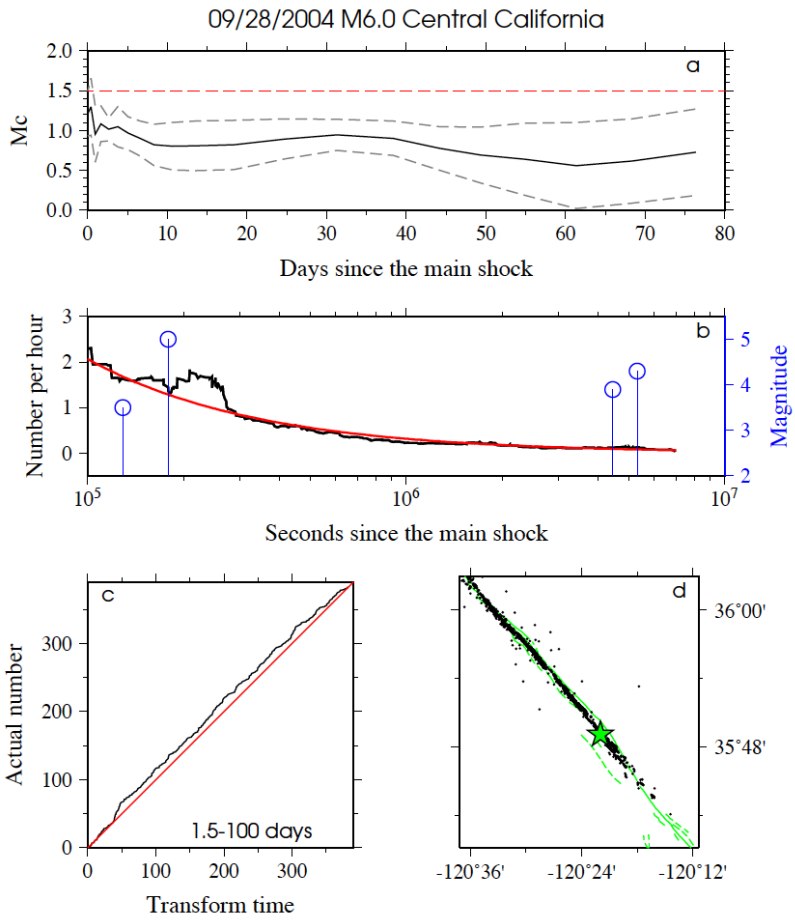

Figure S6.3 The aftershock sequence of the 09/28/2004 M6.0 Central California earthquake. All the denotations are the same as Figure S6.1.

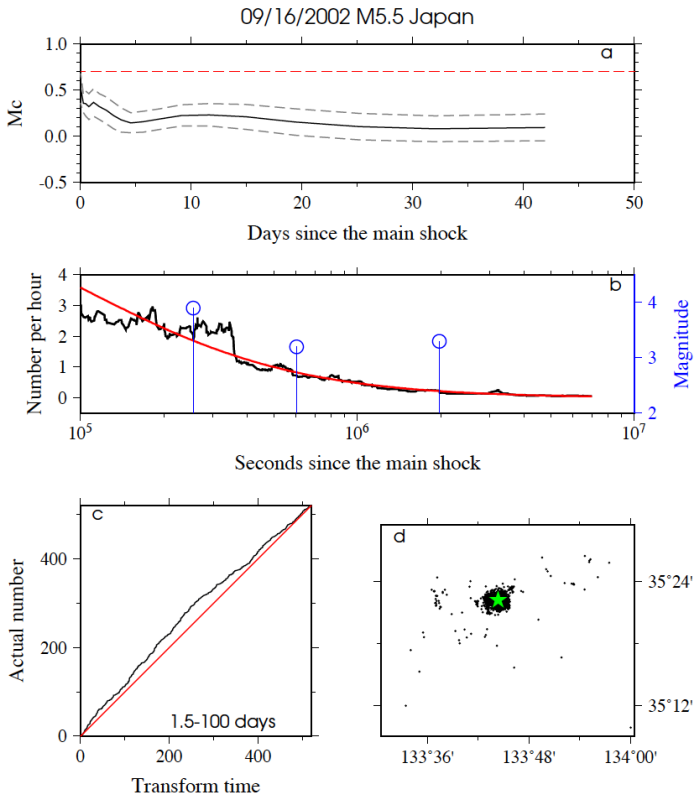

Figure S6.4 The aftershock sequence of the 09/16/2002 M5.5 earthquake in Japan. All the denotations are the same as Figure S6.1.

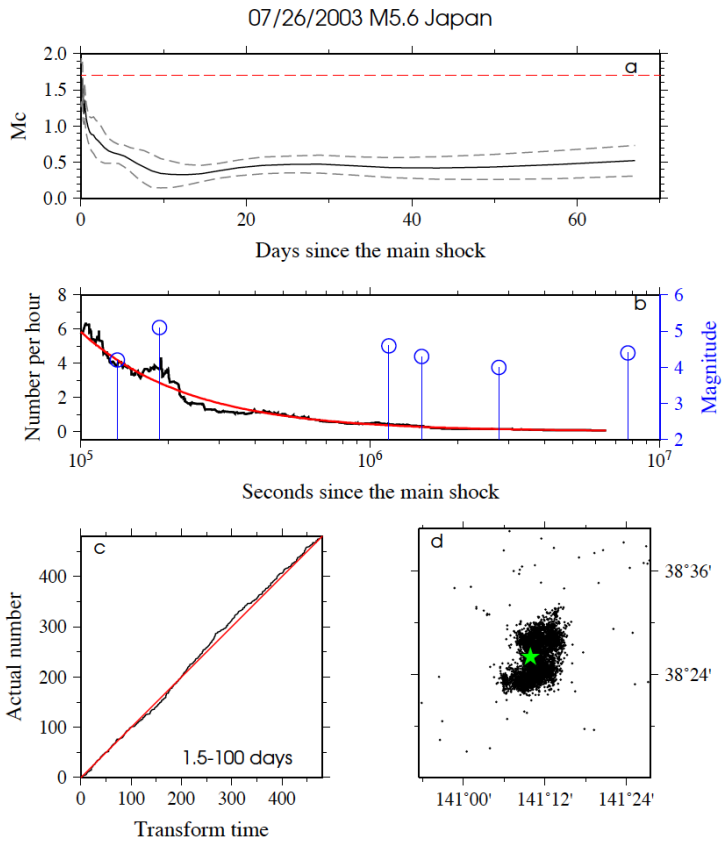

Figure S6.5 The aftershock sequence of the 07/26/2003 M5.6 earthquake in Japan. All the denotations are the same as Figure S6.1.

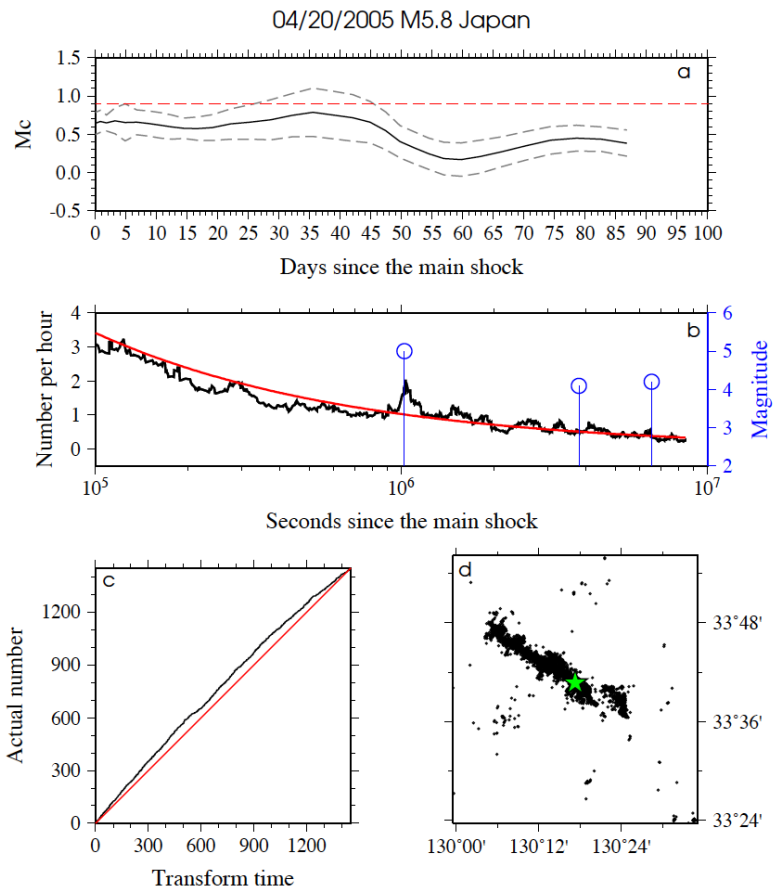

Figure S6.6 The aftershock sequence of the 04/20/2005 M5.8 earthquake in Japan. All the denotations are the same as Figure S6.1.

CHAPTER 7

CONCLUSION AND FUTURE WORK

Using newly detected events from the matched filter technique, I investigated a wide spectrum of earthquake triggering mechanisms, including static and dynamic stress changes, atmospheric pressure changes and deep creep. I found clear evidence of 'stress shadow', a shut-down of seismicity due to negative Coulomb stress changes along Parkfield section of the San Andreas Fault following the 2003 M6.5 San Simeon earthquake, suggesting that static stress change is important for near-field triggering. By examining the temporal evolution of seismicity near Salton Sea and along the San Jacinto Fault following the 2010 M7.2 El Mayor earthquake. I observed that dynamic triggering is dominant in the first few tens of days following the mainshock, while static triggering takes over in a relative longer-term. This work is one of the first observations on the coexistence of dynamic and static triggering, which demonstrates the need to take account of different triggering mechanisms while assessing seismic hazard. I also observed that atmospheric pressure decrease during hurricane Irene may have triggered additional aftershocks following the 2011 M5.7 Virginia earthquake, which was not observed before. Finally, I found extended aftershock zones following five moderate-size earthquakes near the Anza gap along the San Jacinto Fault that are likely driven by deep creep. The results illustrate a weak root of the San Jacinto Fault that might significantly limit the size of the future earthquake rupturing the Anza gap.

My collective studies demonstrate that moderate-size to large earthquakes are able to significantly alter seismic activity around the rupture zone. Hence, detailed

investigations on near-field triggering have the potential to forecast seismic hazard following large earthquakes. However, my results also show that there is not one physical process can explain all triggering phenomenon. The dominant triggering mechanism seems to vary from region to region and sequence to sequence. In some cases, multiple mechanisms work jointly, but dominate in different time scales.

Despite decades of effort, scientists are still debating on the relative importance of different triggering mechanisms. As a result, the limited knowledge on triggering mechanisms prevents efficient seismic hazard forecast and mitigation. To further decipher earthquake triggering, we need to investigate the long-term (i.e., years to decades) seismicity rate changes at many seismic active regions and analyze their response to different types of stress perturbations. In the mean time, stress perturbations do not only trigger earthquakes along the faults, but may also alter certain fault properties (e.g., seismic velocity) [*Brenguier et al.*, 2008]. Thus, continuously monitoring seismic velocity changes near active fault zones may also help understand the physics of earthquake triggering.

One potential problem is that studies on earthquake triggering require high-quality earthquake catalogs. In some newly instrumented regions, local earthquake catalogs may not exist at all. In this case, in order to apply the matched filter technique, one must identify some earthquakes beforehand either manually or automatically. It is some inefficient; more importantly, the quality of the final catalog strongly depends on that of the initial library of templates. Therefore, I plan to develop an autocorrelation technique that is capable of detecting repetitive seismic signals through multi-year-long waveforms. Specifically, the multi-year-long waveforms are dissected into numerous short time

windows, and every pair of those time windows are cross-correlated for each station. Repeating (or similar) signals can be detected by relatively high correlation coefficients across the entire network. Such an autocorrelation scheme [*Brown et al.*, 2008] is similar to the waveform matched filter technique. However, it does not require any known event (i.e., template), but will systematically search for any repetitive seismic signals, including regular earthquakes, tectonic tremor, volcanic tremor and other kinds (e.g., icequakes).

In regions with good local catalogs (e.g., Japan and California), using a large GPU cluster and instant access to continuous recordings, the GPU-based code has the potential to become a near-real-time application. That is, the technique can detect new events from the continuous data efficiently, using all previously cataloged earthquakes as templates. Moreover, the software hypoDD [*Waldhauser and Ellsworth*, 2000] is designed to calculate the relative positions among closely located earthquakes. Both the matched filter technique and hypoDD require cross-correlation between two events. Therefore, it will be optimal that one can directly input the computed correlation coefficients by the matched filter technique to hypoDD for relocation right after an event is detected [*Shelly et al.*, 2013]. If successful, this technique will have following scientific impacts: 1) obtaining a more complete earthquake sequence can improve the rapid seismic hazard assessment on nearby major faults (i.e., operational earthquake forecasting) [*Jordan et al.*, 2011]; 2) detecting early aftershocks following large earthquakes in the first a few hours to one day has the potential to forecast large future aftershocks that possibly cause additional damages [*Omi et al.*, 2013]; 3) the accurate pattern of the spatial-temporal migration of aftershock sequences can be used to image the ruptured fault structure in a fine-scale [*Peng and Zhao*, 2009]. Some of the

aforementioned topics will be pursued during the Data Science Postdoctoral Fellowship at University of Washington.

References

Ader, T. J., and J. P. Avouac (2013), Detecting periodicities and declustering in earthquake catalogs using the Schuster spectrum, application to Himalayan seismicity, *Earth Planet Sc Lett*, *377*, 97-105.

Agnew, D. C., and F. Wyatt (2005), Possible triggered aseismic slip on the San Jacinto fault, in *Southern California Earthquake Center Annual Meeting*, edited, Palm Springs, California.

Allam, A. A., Y. Ben-Zion, I. Kurzon, and F. Vernon (2014), Seismic velocity structure in the Hot Springs and Trifurcation areas of the San Jacinto fault zone, California, from double-difference tomography, *Geophysical Journal International*, *198*(2), 978-999.

Anderson, G., D. C. Agnew, and H. O. Johnson (2003), Salton trough regional deformation estimated from combined trilateration and survey-mode GPS data, *Bulletin of the Seismological Society of America*, *93*(6), 2402-2414.

Aron, A., and J. Hardebeck (2009), Seismicity rate changes along the central California coast due to stress changes from the 2003 M 6.5 San Simeon and 2004 M 6.0 Parkfield earthquakes, *Bulletin of the Seismological Society of America*, *99*(4), 2280-2292.

Avila, L. A., and J. Cangialosi (2011), Hurricane Irene, *Trop. Cyclone Rep.*, 44 pp, Natl. Hurricane Cent., Miami, Fla.

Bailey, I. W., Y. Ben-Zion, T. W. Becker, and M. Holschneider (2010), Quantifying focal mechanism heterogeneity for fault zones in central and southern California, *Geophysical Journal International*, *183*(1), 433-450.

Barbour, A. J., and D. C. Agnew (2012), Detection of Seismic Signals Using Seismometers and Strainmeters, *Bulletin of the Seismological Society of America*, *102*(6), 2484-2490.

Ben-Zion, Y., and P. Leary (1986), Thermoelastic Strain in a Half-Space Covered by Unconsolidated Material, *Bulletin of the Seismological Society of America*, *76*(5), 1447-1460.

Bollinge, G. A. (1973), Seismicity of Southeastern United-States, *Bulletin of the Seismological Society of America*, *63*(5), 1785-1808.

Brenguier, F., M. Campillo, C. Hadziioannou, N. M. Shapiro, R. M. Nadeau, and E. Larose (2008), Postseismic relaxation along the San Andreas fault at Parkfield from continuous seismological observations, *Science*, *321*(5895), 1478-1481.

Brodsky, E. E. (2006), Long-range triggered earthquakes that continue after the wave train passes, *Geophysical Research Letters*, *33*(15).

Brodsky, E. E., and S. G. Prejean (2005), New constraints on mechanisms of remotely triggered seismicity at Long Valley Caldera, *J Geophys Res-Sol Ea*, *110*(B4).

Brodsky, E. E., and L. J. Lajoie (2013), Anthropogenic Seismicity Rates and Operational Parameters at the Salton Sea Geothermal Field, *Science*, *341*(6145), 543-546.

Brodsky, E. E., and N. J. van der Elst (2014), The Uses of Dynamic Earthquake Triggering, *Annual Review of Earth and Planetary Sciences, Vol 42*, *42*, 317-339.

Brown, J. R., G. C. Beroza, and D. R. Shelly (2008), An autocorrelation method to detect low frequency earthquakes within tremor, *Geophysical Research Letters*, *35*(16).

Buck, I. (2007), GPU computing: Programming a massively parallel processor, *CGO 2007: International Symposium on Code Generation and Optimization*, 17-17.

Chapman, M. C. (2013), On the Rupture Process of the 23 August 2011 Virginia Earthquake, *Bulletin of the Seismological Society of America*, *103*(2A), 613-628.

Cochran, E. S., J. E. Vidale, and S. Tanaka (2004), Earth tides can trigger shallow thrust fault earthquakes, *Science*, *306*(5699), 1164-1166.

Costain, J. K., and G. A. Bollinger (2010), Review: Research Results in Hydroseismicity from 1987 to 2009, *Bulletin of the Seismological Society of America*, *100*(5A), 1841-1858.

Dieterich, J. (1994), A Constitutive Law for Rate of Earthquake Production and Its Application to Earthquake Clustering, *J Geophys Res-Sol Ea*, *99*(B2), 2601-2618.

Ellsworth, W. L. (2013), Injection-Induced Earthquakes, *Science*, *341*(6142), 142-+.

Enescu, B., J. Mori, and M. Miyazawa (2007), Quantifying early aftershock activity of the 2004 mid-Niigata Prefecture earthquake (Mw6.6), *J Geophys Res-Sol Ea*, *112*(B4).

Enescu, B., J. Mori, M. Miyazawa, and Y. Kano (2009), Omori-Utsu Law c-Values Associated with Recent Moderate Earthquakes in Japan, *Bulletin of the Seismological Society of America*, *99*(2A), 884-891.

Felzer, K. R., and E. E. Brodsky (2005), Testing the stress shadow hypothesis, *J Geophys Res-Sol Ea*, *110*(B5).

Felzer, K. R., and D. Kilb (2009), A Case Study of Two M similar to 5 Mainshocks in Anza, California: Is the Footprint of an Aftershock Sequence Larger Than We Think?, *Bulletin of the Seismological Society of America*, *99*(5), 2721-2735.

Fialko, Y. (2006), Interseismic strain accumulation and the earthquake potential on the southern San Andreas fault system, *Nature*, *441*(7096), 968-971.

Fletcher, J., L. Haar, T. Hanks, L. Baker, F. Vernon, J. Berger, and J. Brune (1987), The Digital Array at Anza, California - Processing and Initial Interpretation of Source Parameters, *J Geophys Res-Solid*, *92*(B1), 369-382.

Freed, A. M. (2005), Earthquake triggering by static, dynamic, and postseismic stress transfer, *Annu Rev Earth Pl Sc*, *33*, 335-367.

Freed, A. M., and J. Lin (2001), Delayed triggering of the 1999 Hector Mine earthquake by viscoelastic stress transfer, *Nature*, *411*(6834), 180-183.

Gao, S. S., P. G. Silver, A. T. Linde, and I. S. Sacks (2000), Annual modulation of triggered seismicity following the 1992 Landers earthquake in California, *Nature*, *406*(6795), 500-504.

Gerstenberger, M., S. Wiemer, L. Jones, and P. Reasenberg (2005), Real-time forecasts of tomorrow's earthquakes in California, *Nature*, *435*(7040), 328-331.

Gibbons, S. J., and F. Ringdal (2006), The detection of low magnitude seismic events using array-based waveform correlation, *Geophysical Journal International*, *165*(1), 149-166.

Gomberg, J., M. L. Blanpied, and N. M. Beeler (1997), Transient triggering of near and distant earthquakes, *Bulletin of the Seismological Society of America*, *87*(2), 294-309.

Graves, R. W., B. T. Aagaard, and K. W. Hudnut (2011), The ShakeOut Earthquake Source and Ground Motion Simulations, *Earthq Spectra*, *27*(2), 273-291.

Hainzl, S., Y. Ben-Zion, C. Cattania, and J. Wassermann (2013), Testing atmospheric and tidal earthquake triggering at Mt. Hochstaufen, Germany, *J Geophys Res-Sol Ea*, *118*(10), 5442-5452.

Hainzl, S., T. Kraft, J. Wassermann, H. Igel, and E. Schmedes (2006), Evidence for rainfall-triggered earthquake activity, *Geophysical Research Letters*, *33*(19).

Hardebeck, J. L., and A. Aron (2009), Earthquake Stress Drops and Inferred Fault Strength on the Hayward Fault, East San Francisco Bay, California, *Bulletin of the Seismological Society of America*, *99*(3), 1801-1814.

Hardebeck, J. L., et al. (2004), Preliminary report on the 22 December 2003, M 6.5 San Simeon, California earthquake, *Seismological Research Letters*, *75*(2), 155-172.

Hauksson, E., W. Z. Yang, and P. M. Shearer (2012), Waveform Relocated Earthquake Catalog for Southern California (1981 to June 2011), *Bulletin of the Seismological Society of America*, *102*(5), 2239-2244.

Hauksson, E., J. Stock, K. Hutton, W. Z. Yang, J. A. Vidal-Villegas, and H. Kanamori (2011), The 2010 Mw 7.2 El Mayor-Cucapah Earthquake Sequence, Baja California,

Mexico and Southernmost California, USA: Active Seismotectonics along the Mexican Pacific Margin, *Pure Appl Geophys*, *168*(8-9), 1255-1277.

Hill, D., and S. Prejean (2007), Dynamic triggering, *in Treatise on Geophysics*, *Vol. 4*, 257-291.

Hodgkinson, K. (2013), Strainmeters capture strain transients following the M4.7 March 2013 Anza Earthquake, edited.

Hough, S. E., and H. Kanamori (2002), Source properties of earthquakes near the Salton Sea triggered by the 16 October 1999 M 7.1 Hector Mine, California, earthquake, *Bulletin of the Seismological Society of America*, *92*(4), 1281-1289.

Ji, C., K. Larson, Y. Tan, K. Hudnut, and K. Choi (2004), Slip history of the 2003 San Simeon earthquake constrained by combining 1-Hz GPS, strong motion, and teleseismic data, *Geophysical Research Letters*, *31*(17).

Jordan, T. H., Y. T. Chen, P. Gasparini, R. Madariaga, I. Main, W. Marzocchi, G. Papadopoulos, G. Sobolev, K. Yamaoka, and J. Zschau (2011), Operational Earthquake Forecasting: State of Knowledge and Guidelines for Utilization, *Ann Geophys-Italy*, *54*(4), 315-391.

Kagan, Y. Y. (2002), Aftershock zone scaling, *Bulletin of the Seismological Society of America*, *92*(2), 641-655.

Kanamori, H., and E. E. Brodsky (2004), The physics of earthquakes, *Rep Prog Phys*, *67*(8), 1429-1496.

Kato, A., J. Fukuda, and K. Obara (2013), Response of seismicity to static and dynamic stress changes induced by the 2011 M9.0 Tohoku-Oki earthquake, *Geophysical Research Letters*, *40*(14), 3572-3578.

Kato, A., K. Obara, T. Igarashi, H. Tsuruoka, S. Nakagawa, and N. Hirata (2012), Propagation of Slow Slip Leading Up to the 2011 M-w 9.0 Tohoku-Oki Earthquake, *Science*, *335*(6069), 705-708.

Kilb, D., J. Gomberg, and P. Bodin (2002), Aftershock triggering by complete Coulomb stress changes, *J Geophys Res-Sol Ea*, *107*(B4).

Kilb, D., V. G. Martynov, and F. L. Vernon (2007), Aftershock detection thresholds as a function of time: Results from the ANZA seismic network following the 31 October 2001 M-L 5.1 ANZA, California, earthquake, *Bulletin of the Seismological Society of America*, *97*(3), 780-792.

Kim, W. Y., and M. C. Chapman (2005), The 9 December 2003 central Virginia earthquake sequence: A compound earthquake in the central Virginia seismic zone, *Bulletin of the Seismological Society of America*, *95*(6), 2428-2445.

King, G., R. S. Stein, and J. Lin (1994), Static stress changes and the triggering of earthquakes, *Bulletin of the Seismological Society of America*, *84*(3), 935-953.

Lay, T., et al. (2009), Seismological Grand Challeges in Understanding Earth's Dynamic Systems, in *Report to the National Science Foundation, IRIS Consortium*, edited, p. 76.

Lindsey, E. O., V. J. Sahakian, Y. Fialko, Y. Bock, S. Barbot, and T. K. Rockwell (2014), Interseismic Strain Localization in the San Jacinto Fault Zone, *Pure Appl Geophys*, *171*(11), 2937-2954.

Liu, C., A. Linde, and I. Sacks (2009), Slow earthquakes triggered by typhoons, *Nature*, *459*(7248), 833-836.

Llenos, A. L., J. J. McGuire, and Y. Ogata (2009), Modeling seismic swarms triggered by aseismic transients, *Earth Planet Sc Lett*, *281*(1-2), 59-69.

Lockner, D., C. Morrow, D. Moore, and S. Hickman (2011), Low strength of deep San Andreas fault gouge from SAFOD core, *Nature*, *472*(7341), 82-U107.

Lohman, R. B., and J. J. McGuire (2007), Earthquake swarms driven by aseismic creep in the Salton Trough, California, *J Geophys Res-Sol Ea*, *112*(B4).

Ma, K. F., C. H. Chan, and R. S. Stein (2005), Response of seismicity to Coulomb stress triggers and shadows of the 1999 M-w=7.6 Chi-Chi, Taiwan, earthquake, *J Geophys Res-Sol Ea*, *110*(B5).

Macedonia, M. (2003), The GPU enters computing's mainstream, *Computer*, *36*(10), 106-108.

Marsan, D., and S. S. Nalbant (2005), Methods for measuring seismicity rate changes: A review and a study of how the Mw 7.3 Landers earthquake affected the aftershock sequence of the Mw 6.1 Joshua Tree earthquake, *Pure Appl Geophys*, *162*(6-7), 1151-1185.

Matthews, M. V., and P. A. Reasenberg (1988), Statistical-Methods for Investigating Quiescence and Other Temporal Seismicity Patterns, *Pure Appl Geophys*, *126*(2-4), 357-372.

McLaren, M., J. Hardebeck, N. van der Elst, J. Unruh, G. Bawden, and J. Blair (2008), Complex faulting associated with the 22 December 2003 M(w) 6.5 San Simeon, California, earthquake, aftershocks, and postseismic surface deformation, *Bulletin of the Seismological Society of America*, *98*(4), 1659-1680.

McNamara, D. E., H. M. Benz, R. B. Herrmann, E. A. Bergman, P. Earle, A. Meltzer, M. Withers, and M. Chapman (2014), The M-w 5.8 Mineral, Virginia, Earthquake of August 2011 and Aftershock Sequence: Constraints on Earthquake Source Parameters and Fault Geometry, *Bulletin of the Seismological Society of America*, *104*(1), 40-54.

Meng, X., and Z. Peng (2014), Seismicity rate changes in the Salton Sea Geothermal Field and the San Jacinto Fault Zone after the 2010 M-w 7.2 El Mayor-Cucapah earthquake, *Geophysical Journal International*, *197*(3), 1750-1762.

Meng, X., and Z. Peng (2015), Improved understanding of moderate-size earthquake sequences on the San Jacinto Fault and their relationship with deep creep, *in prep*.

Meng, X., Z. Peng, and J. Hardebeck (2013), Seismicity around Parkfield correlates with static shear stress changes following the 2003 Mw6.5 San Simeon earthquake, *J Geophys Res-Sol Ea*, *118*(7), 3576-3591.

Meng, X., H. Yang, and Z. Peng (2015), Hurricane Irene's Impacts on the Earthquake Sequence of the 2011 Mw5.8 Virginia Earthquake, *Nature Geoscience, in review*.

Meng, X., X. Yu, Z. Peng, and B. Hong (2012), Detecting Earthquakes around Salton Sea Following the 2010 M(w)7.2 El Mayor-Cucapah Earthquake Using GPU Parallel Computing, *Procedia Comput Sci*, *9*, 937-946.

Mogi, K. (1962), Magnitude frequency relations for elastic shocks accompanying fractures of various materials and some related problems in earthquakes, *Bull. Earthquakes Res. Inst. Univ. Tokyo*, *40*, 831-853.

Mori, J. (1993), Fault Plane Determinations for 3 Small Earthquakes Along the San-Jacinto Fault, California - Search for Cross Faults, *J Geophys Res-Sol Ea*, *98*(B10), 17711-17722.

Murray, J., and J. Langbein (2006), Slip on the San Andreas Fault at Parkfield, California, over Two Earthquake Cycles, and the Implications for Seismic Hazard, *Bulletin of the Seismological Society of America*, *96*(4B), S283-S303.

Nickolls, J., and W. J. Dally (2010), The Gpu Computing Era, *Ieee Micro*, *30*(2), 56-69.

Obara, K. (2002), Nonvolcanic deep tremor associated with subduction in southwest Japan, *Science*, *296*(5573), 1679-1681.

Ogata, Y. (1988), Statistical-Models for Earthquake Occurrences and Residual Analysis for Point-Processes, *J Am Stat Assoc*, *83*(401), 9-27.

Ogata, Y. (2006), Fortran programs statistical analysis of seismicity -updated version (point process data), EPTREN, LINLIN, SIMBVP, LINSIM and PGRAPH in cluded in Time Series and Control Program Package, SASeis2006, *Computer Science Monograph*, *No. 33*.

Omi, T., Y. Ogata, Y. Hirata, and K. Aihara (2013), Forecasting large aftershocks within one day after the main shock, *Sci Rep-Uk*, *3*.

Omori, F. (1894), On the aftershocks of earthquakes, *J. Coll. Sci., Imp. Univ. Tokyo*, *7*, 111-200.

Owens, J. D., M. Houston, D. Luebke, S. Green, J. E. Stone, and J. C. Phillips (2008), Gpu Computing, *P Ieee*, *96*(5), 879-899.

Parsons, T. (2005), A hypothesis for delayed dynamic earthquake triggering, *Geophysical Research Letters*, *32*(4).

Parsons, T., and M. Segou (2014), Stress, Distance, Magnitude, and Clustering Influences on the Success or Failure of an Aftershock Forecast: The 2013 M 6.6 Lushan Earthquake and Other Examples, *Seismological Research Letters*, *85*(1), 44-51.

Peltzer, G., P. Rosen, F. Rogez, and K. Hudnut (1998), Poroelastic rebound along the Landers 1992 earthquake surface rupture, *J Geophys Res-Sol Ea*, *103*(B12), 30131-30145.

Peng, Z., and P. Zhao (2009), Migration of early aftershocks following the 2004 Parkfield earthquake, *Nature Geoscience*, *2*(12), 877-881.

Peng, Z., and J. Gomberg (2010), An integrated perspective of the continuum between earthquakes and slow-slip phenomena, *Nature Geoscience*, *3*(9), 599-607.

Peng, Z., J. E. Vidale, and H. Houston (2006), Anomalous early aftershock decay rate of the 2004 Mw6.0 Parkfield, California, earthquake, *Geophysical Research Letters*, *33*(17).

Peng, Z., J. E. Vidale, M. Ishii, and A. Helmstetter (2007), Seismicity rate immediately before and after main shock rupture from high-frequency waveforms in Japan, *J Geophys Res-Sol Ea*, *112*(B3).

Pollitz, F. F., R. Burgmann, and W. Thatcher (2012a), Illumination of rheological mantle heterogeneity by the M7.2 2010 El Mayor-Cucapah earthquake, *Geochem Geophy Geosy*, *13*.

Pollitz, F. F., R. S. Stein, V. Sevilgen, and R. Burgmann (2012b), The 11 April 2012 east Indian Ocean earthquake triggered large aftershocks worldwide, *Nature*, *490*(7419), 250-+.

Reasenberg, P., and M. V. Matthews (1988), Precursory Seismic Quiescence - a Preliminary Assessment of the Hypothesis, *Pure Appl Geophys*, *126*(2-4), 373-406.

Reasenberg, P., and L. Jones (1989), Earthquake hazard after a mainshock in California, *Science*, *243*(4895), 1173-1176.

Richards-Dinger, K., R. S. Stein, and S. Toda (2010), Decay of aftershock density with distance does not indicate triggering by dynamic stress, *Nature*, *467*(7315), 583-U105.

Rockwell, T., C. Loughman, and P. Merifield (1990), Late Quaternary Rate of Slip Along the San-Jacinto Fault Zone near Anza, Southern California, *J Geophys Res-Solid*, *95*(B6), 8593-8605.

Ross, Z., Y. Ben-Zion, and L. Zhu (2015), Isotropic source terms of San Jacinto fault zone earthquakes based on waveform inversions with a generalized CAP method, *Geophysical Journal International*, *200*, 1267-1278.

Sanders, C. O., and H. Kanamori (1984), A Seismotectonic Analysis of the Anza Seismic Gap, San-Jacinto Fault Zone, Southern-California, *J Geophys Res*, *89*(Nb7), 5873-5890.

Scholz, C. H. (1990), *The Mechanics of Earthquakes and Faulting*, Cambridge University Press, New York.

Shapiro, N. M., M. Campillo, L. Stehly, and M. H. Ritzwoller (2005), High-resolution surface-wave tomography from ambient seismic noise, *Science*, *307*(5715), 1615-1618.

Shelly, D. R., and K. Johnson (2011), Tremor reveals stress shadowing, deep postseismic creep, and depth-dependent slip recurrence on the lower-crustal San Andreas fault near Parkfield, *Geophysical Research Letters*, *38*.

Shelly, D. R., G. Beroza, and S. Ide (2007), Non-volcanic tremor and low-frequency earthquake swarms, *Nature*, *446*(7133), 305-307.

Shelly, D. R., D. P. Hill, F. Massin, J. Farrell, R. B. Smith, and T. Taira (2013), A fluid-driven earthquake swarm on the margin of the Yellowstone caldera, *J Geophys Res-Sol Ea*, *118*(9), 4872-4886.

Stein, R. S. (1999), The role of stress transfer in earthquake occurrence, *Nature*, *402*(6762), 605-609.

Stein, R. S. (2003), Earthquake conversations, *Scientific American*, *288*(1), 72-79.

Sykes, L. R., and S. P. Nishenko (1984), Probabilities of Occurrence of Large Plate Rupturing Earthquakes for the San-Andreas, San-Jacinto, and Imperial Faults, California, 1983-2003, *J Geophys Res*, *89*(Nb7), 5905-5927.

Tanaka, S., M. Ohtake, and H. Sato (2004), Tidal triggering of earthquakes in Japan related to the regional tectonic stress, *Earth Planets Space*, *56*(5), 511-515.

Thatcher, W., J. A. Hileman, and T. C. Hanks (1975), Seismic Slip Distribution Along San-Jacinto Fault Zone, Southern-California, and Its Implications, *Geol Soc Am Bull*, *86*(8), 1140-1146.

Thurber, C., H. Zhang, F. Waldhauser, J. Hardebeck, A. Michael, and D. Eberhart-Phillips (2006), Three-dimensional compressional wavespeed model, earthquake relocations, and focal mechanisms for the Parkfield, California, region, *Bulletin of the Seismological Society of America*, *96*(4), S38-S49.

Toda, S., and R. S. Stein (2002), Response of the San Andreas fault to the 1983 Coalinga-Nunez earthquakes: An application of interaction-based probabilities for Parkfield, *J Geophys Res-Sol Ea*, *107*(B6).

Toda, S., R. S. Stein, and T. Sagiya (2002), Evidence from the AD 2000 Izu islands earthquake swarm that stressing rate governs seismicity, *Nature*, *419*(6902), 58-61.

Toda, S., R. S. Stein, G. Beroza, and D. Marsan (2012), Aftershocks halted by static stress shadows, *Nature Geoscience*, *5*(6), 410-413.

Utsu, T., Y. OGATA, and R. MATSUURA (1995), The centenary of the Omori formula for a decay law of aftershock activity, *Journal of Physics of the Earth*, *43*(1), 1-33.

van der Elst, N. J., H. M. Savage, K. M. Keranen, and G. A. Abers (2013), Enhanced Remote Earthquake Triggering at Fluid-Injection Sites in the Midwestern United States, *Science*, *341*(6142), 164-167.

Waldhauser, F., and W. Ellsworth (2000), A double-difference earthquake location algorithm: Method and application to the northern Hayward fault, California, *Bulletin of the Seismological Society of America*, *90*(6), 1353-1368.

Waldhauser, F., W. Ellsworth, D. Schaff, and A. Cole (2004), Streaks, multiplets, and holes: High-resolution spatio-temporal behavior of Parkfield seismicity, *Geophysical Research Letters*, *31*(18).

Wdowinski, S. (2009), Deep creep as a cause for the excess seismicity along the San Jacinto fault, *Nature Geoscience*, *2*(12), 882-885.

Wells, D. L., and K. J. Coppersmith (1994), New Empirical Relationships among Magnitude, Rupture Length, Rupture Width, Rupture Area, and Surface Displacement, *Bulletin of the Seismological Society of America*, *84*(4), 974-1002.

Wesnousky, S. G. (2006), Predicting the endpoints of earthquake ruptures, *Nature*, *444*(7117), 358-360.

Wiemer, S. (2001), A software package to analyze seismicity: ZMAP, *Seismological Research Letters*, *72*, 373-382.

Yang, H., L. P. Zhu, and R. S. Chu (2009), Fault-Plane Determination of the 18 April 2008 Mount Carmel, Illinois, Earthquake by Detecting and Relocating Aftershocks, *Bulletin of the Seismological Society of America*, *99*(6), 3413-3420.

Yang, W., E. Hauksson, and P. M. Shearer (2012), Computing a Large Refined Catalog of Focal Mechanisms for Southern California (1981-2010): Temporal Stability of the Style of Faulting, *Bulletin of the Seismological Society of America*, *102*(3), 1179-1194.

Zhuang, J. (2006), Second-order residual analysis of spatiotemporal point processes and applications in model evaluation, *J Roy Stat Soc B*, *68*, 635-653.

Zhuang, J., Y. Ogata, and D. Vere-Jones (2002), Stochastic declustering of space-time earthquake occurrences, *J Am Stat Assoc*, *97*(458), 369-380.

Zhuang, J., Y. Ogata, and D. Vere-Jones (2004), Analyzing earthquake clustering features by using stochastic reconstruction, *J Geophys Res-Sol Ea*, *109*(B5).

Zhuang, J., C. P. Chang, Y. Ogata, and Y. I. Chen (2005), A study on the background and clustering seismicity in the Taiwan region by using point process models, *J Geophys Res-Sol Ea*, *110*(B5).

Zoback, M., et al. (1987), New evidence on the state of stress of the San-Andreas Fault System, *Science*, *238*(4830), 1105-1111.